Probing AGN Environments using Absorption Lines

A Thesis submitted for the degree of

Doctor of Philosophy

(in PHYSICS)

to the

TATA INSTITUTE OF FUNDAMENTAL RESEARCH

by

NEERAJ GUPTA

National Centre for Radio Astrophysics
Tata Institute of Fundamental Research
Pune - 411 007

e-mail : *neeraj@ncra.tifr.res.in*

April 2007

Postscript version available from here

Contents

List of Figures

List of Tables

Acknowledgments

My deepest gratitudes to NCRA-TIFR for providing me the opportunity to pursue my interests and way of life in general. I fell in love with the place and people here when I visited NCRA, Pune for the first time as a VSRP participant in the year 2000 to do a summer project. Thanks to Gopal-Krishna for giving that excellent talk at Delhi University which inspired me to come to NCRA for the summer project. I would like to thank my Ph.D. thesis supervisors D.J. Saikia (NCRA-TIFR) and R. Srianand (IUCAA) for their guidance and help while I tried my hand at Astronomy. I would also like to thank our collaborators Chris Salter, Tapasi Ghosh, Patrick Petitjean, Cedric Ledoux and S. Jeyakumar who have contributed to the work that is part of this thesis. I have greatly benefitted from interactions with them and other researchers at NCRA and IUCAA. I am grateful to all of them. I would also like to thank staffs of the Arceibo telescope and GMRT for their assistance during our observations. The Arecibo Observatory is part of the National Astronomy and Ionosphere Center, which is operated by Cornell University under a cooperative agreement with the National Science Foundation. The GMRT is a national facility operated by the National Centre for Radio Astrophysics of the Tata Institute of Fundamental Research. I have also used HST, FUSE and IUE archival data downloaded from MAST. Thanks to MAST archive for the excellent user support and documentation. This research has made use of the NASA/IPAC Extragalactic Database (NED) which is operated by the Jet Propulsion Laboratory, California Institute of Technology, under contract with the National Aeronautics and Space Administration. All the work included in thesis has been done on computers running on Linux and using the open source softwares particularly AIPS, IRAF and LaTex. Thanks to numerous contributers to the Open Source movement. I would also like to thank Viswesh for reading some of the chapters and giving valuable comments. I learnt a great deal from interactions with my friends Sanjay Bhatnagar, Poonam Chandra, Nissim Kanekar, Sanjay Kudale, Urvashi Rau, Jatush Seth and Rajiv Singh. They certainly have a hand in the results presented in this thesis. Finally I would like to thank my office-mates (Urvashi, Resmi, Ananda and Nirupam) and the presence of `National Film Archive of India` and `Film and Television Institute of India` in Pune for making everything so much more fun.

Declaration

This thesis is a presentation of my original research work. Wherever contributions of others are involved, every effort is made to indicate this clearly, with due reference to the literature, and acknowledgment of collaborative research and discussions.
The work was done under the guidance of Professor D. J. Saikia, at the National Centre for Radio Astrophysics.

Neeraj Gupta

In my capacity as supervisor of the candidate's thesis, I certify that the above statements are true to the best of my knowledge.

Prof. D. J. Saikia
Thesis Supervisor

Synopsis

Synopsis of Ph.D. thesis submitted to TIFR
Thesis title: *Probing AGN Environments using Absorption Lines*
Name of Candidate: *Neeraj Gupta (NCRA-TIFR, Pune)*
Thesis supervisor: *Prof. D. J. Saikia (NCRA-TIFR, Pune)*

This thesis uses absorption line measurements to study the circumnuclear and subgalactic *environments* of the two minority and *almost* exclusive classes of active galactic nuclei (AGNs) i.e. radio loud AGN and broad absorption line (BAL) quasar. About 15%-20% AGNs have ratios of radio (5 GHz) to optical (B-band) flux density, $F_5/F_B \gtrsim 10$ and are referred to as radio loud. Radio loud AGNs are usually associated with radio jets that often extend upto distances much larger than the extent of their host galaxies. Interestingly, emission-line and continuum spectra from IR to X-rays for most of the AGNs, whether radio quiet or radio loud are similar. Based on the properties of optical and ultraviolet spectra AGNs have been classified as Type 1 or Type 2. Type 1 AGNs are those which exhibit broad emission lines and amongst the radio loud ones, Type 1 AGNs include broad line radio galaxies (BLRGs), steep-spectrum radio quasars (SSRQs) and flat-spectrum radio quasars (FSRQs). It is worth mentioning at this point that radio loud AGNs are classified as steep- or flat-spectrum depending on whether the radio spectral index (α; where $F(\nu) \propto \nu^{-\alpha}$) measured at frequencies $\gtrsim$ 1 GHz is greater or less than 0.5. AGNs which show only narrow emission lines are classified as Type 2. This includes narrow line radio galaxies (NLRGs) from the radio loud side. Much of this diversity can be simplified by adopting unification schemes which attribute several aspects of the diversity to the orientation of AGN with respect to the observer. Relativistic Doppler boosting of the electromagnetic radiation and presence of the circumnuclear obscuring torus are two essential ingredients of these unification schemes.

Radio loud AGNs have also been classified on the basis of their structural and spec-

tral properties Most prominent of these empirical categorization is the Fanaroff & Riley classification (i.e. FR I and FR II class) based on radio source morphology. FR I radio galaxies are characterized by subsonic radio jets whose intensity falls from the centre outward. FR II class consists of powerful radio galaxies that have supersonic jets that end in a bright hotspots. FR I and FR II radio morphologies have been found to strongly correlate with radio power, with FR Is and FR IIs lying below and above the power, $P_{178MHz} \sim 2 \times 10^{25}$ W Hz^{-1} Sr^{-1}. FR I and FR II class differ in more ways as well. For example at low redshifts, FR Is are found in relatively rich cluster environments whereas FR IIs are more isolated. It is probably in these differences lies the key to understanding the triggering of AGN and formation of jets.

Another striking classification of radio loud AGNs based on size and spectrum is that of compact steep-spectrum (CSS) and gigahertz peaked spectrum (GPS) sources. Most remarkable feature of CSS and GPS sources is their compactness ($\lesssim$15 kpc for CSS; $\lesssim$1 kpc for GPS) which has been established to be largely intrinsic on the basis of spectral ageing and jet-advancement speeds. These sources are therefore believed to be progenitors of classical large radio sources that extend far beyond the extent of host galaxy. In fact, these compact radio sources are often found to be strongly interacting with the ambient environment.

An understanding of the distribution and kinematics of the different components of the circumnuclear gas in AGNs, in general, is therefore important for studying the physical conditions in the nuclear region, the anisotropy of the radiation field and thereby testing the unification schemes. Physical conditions and kinematics of the gas at circumnuclear and subgalactic scales is also expected to contain imprints of the evolution of compact radio sources. In this thesis we have used absorption lines (from our own measurements as well as from the literature) associated with the radio loud AGN to address the following issues:

- What is the distribution and kinematics of neutral hydrogen in radio loud AGN?
- How does the 21-cm HI absorption detection rate and properties of absorption depend on projected linear size, redshift, luminosity and Fanaroff-Riley class type?
- Are the statistical trends in neutral hydrogen properties consistent with expectations of unification schemes?
- How much role does jet-cloud interaction play in determining the kinematics and physical conditions of absorbing gas?

There exists a class of radio quiet quasars which are characterised by the presence of associated absorption lines as broad as several 1000 $\mathrm{km\,s^{-1}}$. These are called broad absorption line quasars and form 10%-20% of the quasar population. Apart from this, BAL QSOs appear to be drawn from the same parent population as non-BAL QSOs when both are selected by their UV/optical properties. This has led to the suggestions that BAL and non-BAL QSOs are intrinsically same and the gas producing BAL has a covering factor of about 10%-20%. BAL QSOs have been known to be systematically X-ray quiet as compared to non-BAL QSOs. It is almost likely that this X-ray weakness is intrinsic although existing models of BAL systems largely assume a standard QSO spectrum. In this thesis we have explored the physical conditions in the two well-detached BAL outflow components that are seen in the spectrum of $z_{\rm em}\simeq$4.92 QSO SDSS J160501.21-011220.0.

To address above mentioned issues we have made observations with the Arecibo telescope and GMRT at radio wavelengths, VLT at optical and also used archival data of HST, FUSE and IUE at ultraviolet. **Chapter 1** gives a general overview of the AGN types and a background to the issues dealt in thesis. In **Chapter 2**, I present the results of our Arecibo telescope and GMRT survey to probe environments of radio-loud AGNs via 21-cm HI and OH absorption. The principal targets of this survey were subgalactic-sized CSS and GPS sources whose redshifted 21-cm HI lines lie in the observing bands of these telescopes. Of the 27 sources searched for 21-cm absorption, one totally new HI absorption system was detected against the radio galaxy 3C 258, while five previously known HI absorption systems, and one galaxy detected in emission, were studied with improved frequency resolution and/or sensitivity. Combining our results with those of similar 21-cm absorption searches, we obtain a 'full sample' of 96 radio sources and examine the trends in gas-properties with respect to radio-source characteristics and redshift. We made use of the versatility of Arecibo telescope backend to simultaneously search for OH in the sources observed for 21-cm absorption. No OH in emission or absorption was detected towards any of the sources. These results along with their implications are also presented in this Chapter.

In **Chapter 3**, we discuss in detail the physical conditions in the outflowing material detected by us in the ultraviolet spectra of the CSS quasar 3C 48 alongwith the implications of non-detection of 21-cm presented in **Chapter 2**. Historically, 3C 48 was the second quasar to be identified and has a highly complex and distorted radio structure, speculated to be due to disruption of jet by interaction with a cloud. On the basis of spatial correlation between the radio source and emission line gas, it has been argued that blue-shifted emission line gas bears the imprint of the interaction between the jet and the ambient gas. Outflowing

material detected in absorption in the ultraviolet spectrum obtained from HST, FUSE and IUE exhibits absorption lines over large range of ionisation states. We explore the physical conditions in the absorbing material using photoionization simulation code CLOUDY and find that photoionization models with Solar abundance ratios are enough to explain the observed column densities of all the species except for Ne VIII . Considering the similarity of the kinematics of the emitting and absorbing material and physical situation in 3C 48, it is possible that outflowing material detected in absorption may have also interacted with the radio jet.

In **Chapter 4**, we examine the dependence of HI column density on the degree of core prominence, which is being used as a statistical measure of the orientation of the source axis to the line of sight, for a sample of 32 CSS and GPS sources. We show that although the detection rates for quasars and galaxies are broadly consistent with the expectations for the unification scheme, sources with the lowest values of core prominence do not tend to have the higher values of N(HI). We argue that for this to be consistent with the scenario of unification scheme it is required that radio sources are larger than the scale of the circumnuclear HI disc so that the lines of sight to the lobes at very large inclinations do not intersect the disc.

In **Chapter 5**, I present the results of our GMRT survey of 21-cm absorption towards the cores of 10 FR I and FR II radio galaxies. From our search we made 1 new detection i.e. towards the core of the radio galaxy J2245+3941 (3C 452) and present the upper limits on N(HI) for the remaining 9 sources. We discuss in detail the properties of the 21-cm absorber associated with the narrow line radio galaxy 3C 452 in the light of observations at other wavelengths. Our survey of 21-cm absorption towards the cores of radio galaxies provides an opportunity to probe the HI content at the kpc-scales in these more evolved radio sources and compare it with the absorption studies towards the younger counterparts of these i.e.subgalactic-sized compact radio sources presented in **Chapters 2 and 4**. We combine our results with similar searches reported in the literature to obtain a larger sample called 'core sample' of 42 radio galaxies. Detection rate towards the cores of FR I and FR II radio sources are very similar to the detection rate of $\sim$35% towards the compact radio sources. This is despite the fact that N(HI) upper limits for the searches for 21-cm absorption towards the cores of radio galaxies have not been as deep as the limits obtained for the compact radio sources. It is to be contrasted that majority of absorption lines in the 'core sample' are either redshifted or consistent with systemic velocity as against the case of compact radio sources presented in **Chapter 2** where there is an excess of blueshifted

absorption lines. This accentuates the role played by jet-cloud interaction in accelerating the gas clouds in the case of compact radio sources.

In **Chapter 6**, I present the analysis of broad absorption lines (BALs) seen in the spectrum of the $z_{\rm em}\simeq$4.92 QSO SDSS J160501.21-011220.0. Our high spectral resolution UVES spectrum shows two well detached absorption line systems at $z_{\rm abs}$= 4.685 and 4.855. Physical conditions are investigated in the BAL system at $z_{\rm abs}$= 4.855 using detailed photoionization models. We find that observed column densities of N v , Si iv and C iv in the $z_{\rm abs}$= 4.855 component require that nitrogen is underabundant by more than a factor of 3 compared to silicon if the gas is photoionized by a typical QSO spectrum. We suggest that if the composition of BAL is like that of the emission line regions, it is most likely that the cloud sees an ionizing spectrum similar to what we observe from this QSO that is strongly attenuated in the X-rays. This is interesting as BAL QSOs are found to be systematically X-ray weak compared to *normal* QSOs and it is most likely that X-ray weakness of BAL QSOs is intrinsic.

Finally, in **Chapter 7** I present an overview of the main results of the thesis and recent developments in the field.

List of Publications

Refereed Publications

1. **Detecting cold gas at intermediate redshifts: GMRT survey using Mg II systems**; Neeraj Gupta, R. Srianand, P. Petitjean, P. Khare, D. J. Saikia, D. York, 2007, ApJ-Letters, 654, L111.

2. **HI gas in rejuvenated galaxies: GMRT observations of the DDRG J1247+6723**; D.J. Saikia, Neeraj Gupta, C. Konar, 2007, MNRAS-Letters, 375, L31.

3. **Multiwavelength investigation of a near-solar metallicity sub-DLA at z_{abs}=1.3647 towards PKS 0237−233**; R. Srianand, Neeraj Gupta and Patrick Petitjean, 2006, MNRAS, 375, 584.

4. **Probing radio source environments via HI and OH absorption**; Neeraj Gupta, C.J. Salter, D.J. Saikia, T. Ghosh and S. Jeyakumar, 2006, MNRAS, 373, 972.

5. **Unification scheme and the distribution of neutral gas in compact radio sources**; Neeraj Gupta and D.J. Saikia; 2006, MNRAS, 370, 738.

6. **Associated 21-cm HI absorption towards the radio galaxy 3C 452 (J2245+3941)**; Neeraj Gupta and D.J. Saikia; 2006, MNRAS-Letters, 370, 80L.

7. **Outflowing material in the compact steep-spectrum source quasar 3C 48: evidence of jet-cloud interaction?**; Neeraj Gupta, R. Srianand and D. J. Saikia; 2005, MNRAS, 361, 451.

8. **Outflowing material in the z_{em} = 4.92 BAL QSO SDSS J160501.21-011220.0**; N. Gupta, R. Srianand, P. Petitjean and C. Ledoux; 2003, A&A, 406, 65.

9. **Polarization asymmetry in CSS sources: Evidence of AGN fuel?**; D.J. Saikia and N. Gupta; 2003, A&A, 405, 499

.

Technical Report

- **Procedure for extending uv-limit of potential Giant Metrewave Radio Telescope(GMRT) phase calibrators**; Neeraj Gupta and Sanjay Bhatnagar; NCRA Technical Report, 2003, Oct, R00203.

Conference Proceedings/Poster Papers

1. **Probing radio source environments using absorption lines**; Neeraj Gupta, C.J. Salter, D.J. Saikia, T. Ghosh, and S. Jeyakumar; Science with ALMA: a new era for Astrophysics, International meeting in Madrid, Spain, 2006.

2. **Probing radio source environments using absorption lines**; Neeraj Gupta, C.J. Salter, D.J. Saikia, T. Ghosh, and S. Jeyakumar; The Central Engine of Active Galactic Nuclei, International meeting in X'ian, China, 2006.

3. **Episodic activity in radio galaxies**; D.J. Saikia, C. Konar, M. Jamrozy, J. Machalski, Neeraj Gupta, Ł. Stawarz, K-H. Mack and A. Siemiginowska; The Central Engine of Active Galactic Nuclei, International meeting in X'ian, China, 2006.

4. **Probing radio source environments using absorption lines**; Neeraj Gupta, C.J. Salter, D.J. Saikia, T. Ghosh, R. Srianand and S. Jeyakumar; XXIXth URSI General Assembly 2006.

5. **Probing radio source environments using absorption lines**; Neeraj Gupta, C.J. Salter, D.J. Saikia, T. Ghosh, R. Srianand and S. Jeyakumar; Astronomical Society of India meeting in Nainital, India, 2005.

6. **Polarization Asymmetry in CSS Sources** ; D.J. Saikia and Neeraj Gupta; 2003, BASI, 31, 441.

Chapter 1

Introduction

Active galactic nuclei (AGNs) from being defined as '*relatively nearby stars with most peculiar properties*' have come a long way over the last 50 years (see Shields 1999 for a review). Now we know them as exotic objects residing in the centres of galaxies and emitting tremendous amount of radiative energy across the entire electrmagnetic spectrum. Although not completely understood but widely accepted that it is supermassive black hole surrounded by a small accretion disk which is responsible for the copious amount of radiation (Rees 1984). Besides a supermassive blackhole and an accretion disk, AGN is essentially associated with both a broad line region (BLR) and a narrow line region (NLR). BLR corresponds to the gas clouds surrounding the AGN at radii less than pc and responsible for the broad emission lines (widths$\sim$ few 1000 kms^{-1}) seen in the AGN optical spectra. NLR on the other hand corresponds to much slowly rotating gas clouds that extend upto a few kpc. These give rise to narrow emission lines (widths$\sim$few 100 kms^{-1}) seen in the optical spectra of AGNs. About 15%-20% of AGNs have ratios of radio (5 GHz) to optical (B-band) flux $F_5/F_B \gtrsim 10$ (Kellermann et al. 1989). These are referred to as radio loud AGNs and are usually associated with radio jets that often extend upto distances much larger than the extent of host galaxy. Interestingly, emission-line and continuum spectra from IR to X-rays for most of the AGNs, whether radio loud or radio quiet are similar (Sanders et al. 1989). Obviously, by virtue of their tremendous energy output, AGNs make a deep impact on their environment at pc-to-kpc scale and beyond. This environment in turn is responsible for the triggering and feeding of nuclear activity, an understanding of which requires studying the gas properties at nuclear and subgalactic scales and and also the host galaxy environments.

1.1 Background

1.1.1 AGNs: How do they look?

AGNs, on the basis of their radio luminosity, radio structural and spectral properties and optical spectral characteristics, have been classified into various types. To begin with they have been categorised as radio loud ($F_5/F_B \gtrsim 10$) or radio quiet depending on the ratio of radio to optical emission. Based on the properties of optical and ultraviolet spectra AGNs have been classified as Type 1 or Type 2. Type 1 AGNs are those which exhibit broad emission lines and include low-luminosity radio quiet AGN i.e. Seyfert 1 galaxies and higher-luminosity radio-quiet AGN i.e.quasi-stellar object (QSO). Amongst the radio loud type, Type 1 AGN includes broad-line radio galaxies (BLRGs), steep-spectrum radio quasars (SSRQs) and flat-spectrum radio quasars (FSRQs). It is worth mentioning at this point that radio loud AGNs are classified as steep- or flat-spectrum depending on whether the radio spectral index (α; where $F(\nu) \propto \nu^{-\alpha}$) measured at frequencies of few GHz is greater or less than 0.5. AGNs which show only narrow emission lines are classified as Type 2. This includes Seyfert 2 from radio quiet side and narrow-line radio galaxy (NLRG) from the radio loud side. A few AGNs have the spectra different from Type 1 and Type 2. Sometimes referred to as Type 0 AGN, their spectra often lack strong emission or absorption features and are accompanied by rapid variability, unusually high and variable polarization and superluminal velocities in the nuclear jets. Objects often classified as Optically violent variable (OVV) quasars, Highly polarized quasars (HPQs), Core-dominated quasars (CDQs) and BL Lac objects would fall under this category. Since majority of FSRQs exhibit rapid variability and high polarization, OVV, HPQ and CDQ are often called as FSRQ (see Urry & Padovani 1995 and Krolik 1999 for detailed description on AGN types).

Radio loud AGNs can also be classified on the basis of their structural and spectral properties at radio wavebands. Most prominent of these empirical categorization is the Fanaroff & Riley classification (Fanaroff & Riley 1974). This classification based on radio source morphology consists of two classes: FR I and FR II. FR I radio galaxies are characterized by subsonic radio jets whose intensity falls from the centre outward. FR II class consists of powerful radio galaxies that have supersonic jets that end in a bright hotspot. See Figs. 5.2 and 5.10 for the examples of FR I and FR II radio morphology. FR I and FR II radio morphologies have been found to strongly correlate with radio power, with FR Is and FR IIs lying below and above the power, $P_{178MHz} \sim 2\times10^{25}$ W Hz^{-1} Sr^{-1} (Fanaroff & Riley 1974). FR I and FR II classes differ in more ways as well. FR Is at low redshifts are found in

relatively rich cluster environments whereas FR IIs are isolated (Prestage & Peacock 1988; Owen & Laing 1989; Hill & Lilly 1991). Their radio and optical line luminosities and properties at other wavebands show different correlations and probably in these differences lies clue to the triggering of AGN and formation of jets (see Baum et al. 1995).

Another striking classification of radio loud AGNs is that of compact steep-spectrum (CSS) and gigahertz peaked spectrum (GPS) sources (see O'Dea 1998 for the review). CSSs are defined to be radio sources with projected linear size $\lesssim$15 kpc (H_o=71 km s^{-1} Mpc^{-1}, Ω_m=0.27, Ω_Λ=0.73, Spergel et al. 2003)[1] and having a steep high-frequency radio spectrum ($\alpha\gtrsim$0.5). GPS on the other hand are classified on the basis of their convex radio spectra peaking at $\sim$1 GHz. Most remarkable feature of CSS and GPS sources is their compactness ($\lesssim$15 kpc for CSS; $\lesssim$1 kpc for GPS) which has been established to be intrinsic rather than due to the projection effects (Fanti et al. 1990). Further they are characterized by powerful emission ($P_{1.4GHz}\gtrsim10^{25}$ W Hz^{-1}) and low radio polarization. Several scenarios have been proposed to explain the compactness of CSS and GPS sources in relation to more extended i.e. large radio sources:

- Youth scenario
  In this scenario, CSS and GPS sources represent the early stages of evolution of more evolved sources and hence compact as they are younger ($\lesssim10^6$ yrs).

- Frustrated scenario
  According to this CSS and GPS sources are compact due to their inability to expand through the ISM of host galaxy. Their ages in this scenario are therefore ($\sim10^8$ yrs) similar to large radio sources (O'Dea et al. 1991; de Young 1993; Carvalho 1998).

- Recurrent scenario
  In this scenario CSS and GPS sources are result of the recently *restarted* radio activity. Evidence for this scenario comes from the detection of large scale diffuse radio emission (believed to be relic of past nuclear activity) in about $\sim$18% of the GPS sources (Baum et al. 1990; Stanghellini et al. 1990, 2005).

Most of the current evidence coming from spectral ageing arguments and jet advancement speeds though suggest that these are indeed younger radio sources (Philips & Mutel 1982; Fanti et al. 1995; O'Dea & Baum 1997; Snellen & Schillizi 2002; Polatidis & Conway 2003). Therefore youth scenario is most widely accepted explanation for the compactness of CSS

[1]Cosmology consistently used throughout the thesis.

and GPS sources. However, recurrent and frustrated scenario cannot be completely ruled out and are true for atleast a small fraction of compact radio sources.

1.1.2 Unification scheme and canonical model of AGN

Unification schemes are an attempt to simplify the picture of AGN containing widely different classes by attributing several aspects of diversity to the orientation of AGN with respect to observer. Relativistic Doppler boosting of the electromagnetic radiation and presence of the circumnuclear obscuring torus are two essential ingredients of these unification schemes. Although there exists very little to differentiate between the radio-loud and radio-quiet AGNs on the basis of their continuum and emission-line properties in other wavebands (Sanders et al. 1989) they are to be unified separately. Amongst the radio-quiet type i.e. Seyfert galaxies, Sy2s (equivalently type 2 quasars in case of high luminosity) are the ones which exhibit only narrow emission lines and are therefore believed to be seen at orientations such that circumnuclear torus obscures BLR (see Fig. 1.1). Then Seyfert 1 galaxies (or type 1 quasars) are identical to their type 2 counterparts except that they are being viewed face on thereby exposing the otherwise hidden BLR (see Antonucci & Miller 1985 for the pioneering work). For the radio loud AGN, a very similar picture can be used to unify powerful i.e. FR II broad-line and narrow-line radio galaxies (Barthel 1989). Hardly any unobscured nuclei have been found at the low luminosity end i.e. for FR I radio galaxies (Lawrence 1991; Falcke, Gopal-Krishna & Biermann 1995). It has been suggested that when the radio luminosity is low, the opening angle of the obscuration may be so small that it is no wider than the beaming angle for its relativistic jet. Any unobscured view of an FR I nucleus would then show only as a BL Lac object. This idea of unifying radio-loud AGNs on the basis of radiation anisotropy arising due to relativistic beaming can be used to unify steep- and flat-spectrum radio sources. In this scenario, steep-spectrum and flat-spectrum radio quasars are increasingly aligned versions of FR II radio galaxies (Barthel 1989; Padovani & Urry 1992). Compact radio sources i.e. GPS and CSS sources, which include both quasars and galaxies, have their size distribution and orientation-dependent properties consistent with the expectations of unification scheme for FR II radio sources (Fanti et al. 1990; Saikia et al. 1995).

1.1.3 Evolution of radio loud AGN and interaction with environment

Validity of above mentioned unification schemes require that environments and cosmic evolution of unified AGN classes be identical. FR II galaxies and quasars at low-redshift show

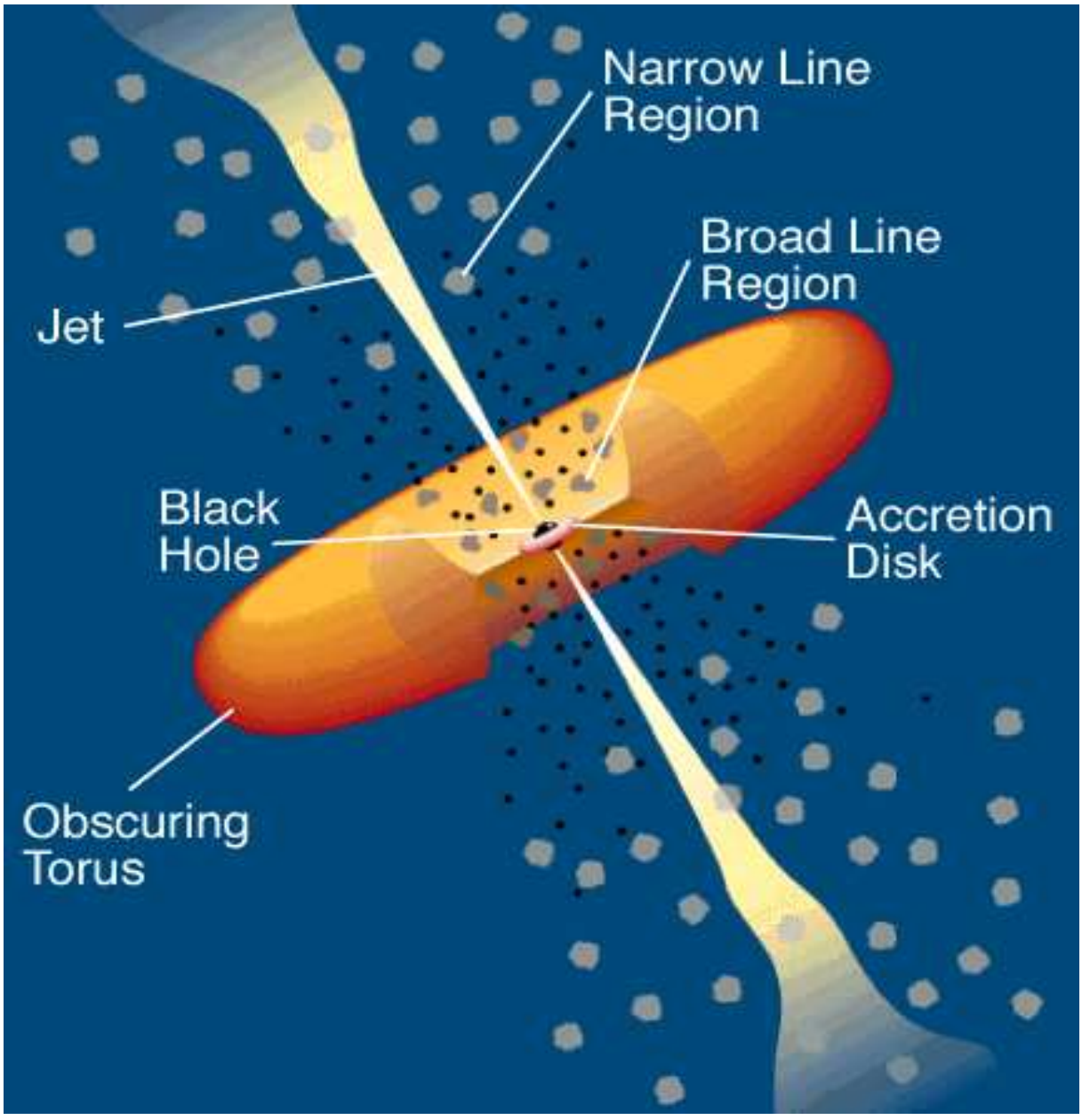

Figure 1.1: Cartoon depicting canonical model of AGN and essential elements of the orientation-based unification schemes (Urry & Padovani 1995).

atmost a marginal difference in their environment (Smith & Heckman 1990). At higher redshifts ($0.35 \lesssim z \lesssim 0.5$) the environments of quasars and galaxies are equally rich (Yates et al. 1989). Likewise, BL Lacs and FR Is also appear to have similar environments (Wurtz et al. 1993; Pesce, Falomo & Treves 1995). CSS and GPS sources, it is popularly believed, are compact i.e. subgalactic sized due to their young age and not because they have been confined by the ambient environment. If they are to evolve into large i.e. several 10 to 100 kpc scale classic radio sources (FR I and FR II) then it is natural to expect interaction between the radio jets and interstellar medium (ISM). Such an interaction must leave its imprints on the

- kinematical and ionisation properties of the ambient gas and
- structural properties of the radio source

Indeed it has been found via radio observations that CSSs tend to be more asymmetric than the large sources (Saikia et al. 1995, 2001; Arshakian & Longair 2000). These authors argued that these asymmetries are due to the interactions of jet with dense clouds of gas. More direct evidence of interaction of jet with ISM have come through polarization measurements and observations of emission line gas. Radio polarization studies often indicate large Faraday depths (e.g. Mantovani et al. 1994; Fanti et al. 2004), and also sometimes show evidence of asymmetrically-located clouds as a huge differential rotation measure between the oppositely directed lobes as in the CSS quasar 3C 147 (Junor et al. 1999), or high rotation measure where the jet bends sharply suggesting collision of the jet with a dense cloud as in 3C 43 (Cotton et al. 2003). Signatures of interaction with the jet in CSSs have been detected in broad and complex emission-line profiles and their alignment with the radio source structure. Gelderman & Whittle (1994) found that properties of [O III] λ5007 for a sample of CSS sources suggest that kinematics of emission line were driven by the radio source. It was however not clear if interaction with radio source also played a direct role in the ionization. Radio-optical alignment, i.e. similar extent and alignment for the radio source and emission-line gas, has been detected for large as well as compact radio sources (Chambers et al. 1987; McCarthy et al. 1987; de Vries et al. 1999; Axon et al. 2000; O'Dea et al. 2002; Labiano et al. 2005). Interaction with the ambient medium is also required to slow down the jet advancements in compact radio sources (de Young 1993; Carvalho 1998) to the speeds estimated for large scale classical doubles (Alexander & Leahy 1987).

1.1.4 Absorption lines as probe of the AGN environment

AGN spectra quiet commonly exhibit absorption lines or ionisation edges arising from both intervening matter and gas associated with the AGN itself. In fact, there exists a class of radio quiet quasars which are characterised by the presence of associated absorption lines as broad as several 1000 $\mathrm{km\,s^{-1}}$. These are called broad absorption line (BAL) quasars and form 10%-20% of the quasar population. Apart from this, BAL QSOs appear to be drawn from the same parent population as non-BALQSOs when both are selected by their UV/optical properties (Weymann et al. 1991; Reichard et al. 2003). This has led to the suggestions that BAL and non-BAL QSO are intrinsically same and the gas producing BAL has a covering factor of about 10%-20% (Weymann et al. 1991). Intervening absorption lines have yielded invaluable information regarding the galaxies and physical state of the Universe particularly at high redshifts where it is difficult to do the similar studies in continuum or emission lines. Here, in this thesis, we concentrate only on the associated absorption lines i.e. absorption caused by the gas associated with AGN or AGN host galaxy which I will refer to as '*AGN environment*'. Detection of absorption lines *associated* with the *AGN environment* over a large range of ionisation stages, in optical and ultraviolet, provides valuable constraints on:

- physical conditions i.e. temperature, density, abundance and ionisation state of the absorbing gas,
- ionizion spectrum i.e. AGN spectral energy distribution in this case, and
- dynamics of the absorbing material i.e. whether falling-in or outflowing and associated momentum and energy.

In the case of radio-loud AGNs, associated 21-cm absorption can be used to probe the dynamics and physical state of cold atomic gas component. Unlike the case of QSO which is a point-like source, extended radio emission of radio-loud AGN can also be used to map the distribution of absorbing gas using 21-cm absorption (e.g. see Mundell et al. 2003 for the most famous case of NGC 4151).

1.2 About this thesis

This thesis uses absorption line measurements to study environments of the two minority and *almost* exclusive classes of AGN i.e. radio loud AGN and broad absorption line quasar. We have based our investigations on the following:

- Issues for radio loud AGN

  - What is the distribution and kinematics of neutral hydrogen in radio loud AGN?
  - How does the 21-cm HI detection rate and properties of absorption depend on projected linear size, redshift, luminosity and Fanaroff-Riley class type?
  - Are the statistical trends in neutral hydrogen properties consistent with expectations of unification schemes?
  - How much role does jet-cloud interaction play in determining the kinematics and physical conditions of absorbing gas?

- Issues for broad absorption line quasar

  - Are BAL QSOs intrinsically x-ray quiet?

To address these issues we make use of the data from a number of observing facilities e.g. our own observations of Arecibo telescope and GMRT at radio wavelengths, VLT at optical and archival data of HST, FUSE and IUE at ultraviolet.

In **Chapter 2**, I present the results of our Arecibo telescope and GMRT survey to probe environments of radio-loud AGNs via 21-cm HI and OH absorption. The principal targets of this survey were subgalactic-sized CSS and GPS sources whose redshifted 21-cm HI lines lie in the observing bands of these telescopes. Of the 27 sources observed, we detect associated HI absorption towards 6 and HI emission for one other. Combining our results with those of similar 21-cm absorption searches, we obtain a 'full sample' of 96 radio sources and examine the trends in gas-properties with respect to radio-source characteristics and redshift. We made use of the versatility of Arecibo telescope backend to simultaneously search for OH in the sources observed for 21-cm absorption. No OH in emission or absorption was detected towards any of the sources. These results along with their implications are also presented in this chapter.

In **Chapter 3**, we discuss in detail the physical conditions in the outflowing material in the CSS quasar 3C 48 alongwith the implications of non-detection of 21-cm presented in **Chapter 2**. Historically, 3C 48 is only second quasar to be identified and has a highly complex and distorted radio structure, speculated to be due to disruption of the jet by interaction with a cloud. On the basis of spatial correlation between the radio source and emission line gas, it has been argued that blue-shifted emission line gas bears the imprint

of the interaction between the jet and the ambient gas. We detected outflowing material in absorption in the ultraviolet spectrum obtained from HST, FUSE and IUE over large range of ionisation states. We explore the physical conditions in the absorbing material using photoionization simulation code CLOUDY and find that photoionization models with Solar abundance ratios are enough to explain the observed column densities of all the species except for Ne VIII . Considering the similarity of the kinematics of the emitting and absorbing material and physical situation in 3C 48, it is possible that outflowing material detected in absorption may have also interacted with the radio jet.

In **Chapter 4**, we examine the dependence of HI column density on the degree of core prominence, which is being used as a statistical measure of the orientation of the source axis to the line of sight, for a sample of 32 CSS and GPS sources. We show that although the detection rates for quasars and galaxies are broadly consistent with the expectations for the unification scheme, sources with the lowest values of core prominence do not tend to have the higher values of N(HI). We argue that for this to be consistent with the scenario of unification scheme it is required that radio sources are larger than the scale of the circumnuclear HI disc so that the lines of sight to the lobes at very large inclinations do not intersect the disc.

In **Chapter 5**, I present the results of our GMRT survey of 21-cm absorption towards the cores of 10 FR I and FR II radio galaxies. From our search we made 1 new detection i.e. towards the core of radio galaxy J2245+3941 (3C 452) and present the upper limits on N(HI) for remaining 9 sources. We discuss in detail the properties of the 21-cm absorber associated with narrow line radio galaxy 3C 452 in the light of observations at other wavelengths. Our survey of 21-cm absorption towards the cores of radio galaxies provides an opportunity to probe the HI content at the kpc-scales in these more evolved radio sources and compare it with the absorption studies towards the younger counterparts of these i.e.subgalactic-sized compact radio sources presented in **Chapters 2 and 4**. We combine our results with similar searches available in literature to obtain a larger sample called 'core sample' of 44 radio galaxies. Detection rate towards the cores of FR I and FR II radio sources compares very well with the detection rate of $\sim$35% towards the compact radio sources. This is despite the fact that N(HI) upper limits for the searches for 21-cm absorption towards the cores of radio galaxies have not been as deep as the limits obtained for the compact radio sources. It is to be contrasted that majority of absorption lines in the 'core sample' are either redshifted or consistent with systemic velocity as against the case of compact radio sources presented in **Chapter 2** where there is an excess of blueshifted absorption lines.

This accentuates the role played by jet-cloud interaction in accelarating the gas clouds in the case of compact radio sources.

In **Chapter 6**, I present the analysis of broad absorption lines (BALs) seen in the spectrum of the $z_{\rm em}\simeq$4.92 QSO SDSS J160501.21-011220.0. Our high spectral resolution UVES spectrum shows two well detached absorption line systems at $z_{\rm abs}$= 4.685 and 4.855. Physical conditions are investigated in the BAL system at $z_{\rm abs}$= 4.855 using detailed photoionization models. We find that observed column densities of N v , Si iv and C iv in the $z_{\rm abs}$= 4.855 component require that nitrogen is underabundant by more than a factor of 3 compared to silicon if the gas is photoionized by a typical QSO spectrum. We suggest that if the composition of BAL is like that of the emission line regions it is most likely that the cloud sees an ionizing spectrum similar to what we observe from this QSO that is strongly attenuated in the X-rays. This is interesting as BAL QSOs are found to be systematically X-ray weak compared to *normal* QSOs and it is most likely that X-ray weakness of BAL QSOs is intrinsic.

Finally, in **Chapter 7** I present an overview of the main results of thesis and recent developments in the field.

Bibliography

[1] Alexander P., Leahy J.P., 1987, MNRAS, 225, 1

[2] Antonucci R.R.J., Miller J.S., 1985, ApJ, 297, 621

[3] Arshakian T.G., Longair M.S., 2000, MNRAS, 311, 846

[4] Axon D.J., Capetti A., Fanti R., Morganti R., Robinson A., Spencer R., 2000, AJ, 120, 2284

[5] Barthel P.D., 1989, ApJ, 336, 606

[6] Baum S.A., Zirbel E.L., O'Dea C.P., 1995, ApJ, 451, 88

[7] Carvalho J.C., 1998, A&A, 329, 845

[8] Chambers K.C., Miley G.K., van Breugel W., 1987, Nature, 329, 604

[9] Cotton W.D., Spencer R.E., Saikia D.J., Garrington S., 2003, A&A, 403, 537

[10] de Vries W.H., O'Dea C.P., Baum S.A., Barthel P.D., 1999, ApJ, 526, 27

[11] de Young D.S., 1993, ApJ, 402, 95

[12] Falcke H., Gopal-Krishna, Biermann P.L., 1995, A&A, 298, 395

[13] Fanaroff B.L., Riley J.M., 1974, MNRAS, 167, 31

[14] Fanti R., Fanti C., Schilizzi R.T., Spencer R.E., Nan R., Parma P., van Breugel W.J.M., Venturi T., 1990, A&A, 231, 333

[15] Fanti C., Fanti R., Dallacasa D., Schilizzi R.T., Spencer R.E., Stanghellini C., 1995, A&A, 302, 317

[16] Fanti et al. 2004, A&A, 427, 465

[17] Gelderman R., Whittle M., 1994, ApJS, 91, 491

[18] Hill G.J., Lilly S.J., 1991, ApJ, 367, 1

[19] Mundell C.G., Wrobel J.M., Pedlar A., Gallimore J.F., 2003, ApJ, 583, 192

[20] Junor W., Salter C.J., Saikia D.J., Mantovani F., Peck A.B., 1999, MNRAS, 308, 955

[21] Kellermann K.I., Sramek R., Schmidt M., Shaffer D.B., Green R., 1989, AJ, 98, 1195

[22] Krolik J.H., 1999, Active galactic nuclei: from the central black hole to the galactic environment (Princeton, NJ: Princeton University Press, 1999)

[23] Labiano A. et al., 2005, A&A, 436, 493

[24] Lawrence A., 1991, MNRAS, 252, 586

[25] Mantovani F., Junor W., Fanti R., Padrielli L., Saikia D.J., 1994, A&A, 292, 59

[26] McCarthy P.J., van Breugel W., Spinrad H., Djorgovski S., 1987, ApJ, 321, L29

[27] O'Dea C.P., Baum S.A., Stanghellini C., 1991, ApJ, 380, 66

[28] O'Dea C.P., Baum S.A., 1997, AJ, 113, 148

[29] O'Dea C.P., 1998, PASP, 110, 493

[30] O'Dea C.P. et al., 2002, AJ, 123, 2333

[31] Owen F.N., Laing R.A., 1989, MNRAS, 238, 357

[32] Pesce J.E., Falomo R., Treves A., 1995, AJ, 110, 1554

[33] Phillips R.B., Mutel R.L., 1982, A&A, 106, 21

[34] Polatidis A.G., Conway J.E., 2003, PASA, 20, 69

[35] Prestage R.M., Peacock J.A., 1988, MNRAS, 230, 131

[36] Rees M.J., 1984, ARA&A, 22, 471

[37] Reichard T.A. et al., 2003, AJ, 126, 2594

[38] Saikia D.J., Jeyakumar S., Wiita P.J., Sanghera H.S., Spencer R.E., 1995, MNRAS, 276, 1215

[39] Saikia D.J., Jeyakumar S., Salter C.J., Thomasson P., Spencer R.E., Mantovani F., 2001, MNRAS, 321, 37

[40] Sanders D.B., Phinney E.S., Neugebauer G., Soifer B.T., Matthews K., 1989, ApJ, 347, 29

[41] Shields G.A., 1999, PASP, 111, 661

[42] Smith E.P., Heckman T.M., 1990, ApJ, 348, 38

[43] Snellen I., Schilizzi R., 2002, NewAR, 46, 61

[44] Spergel D.N. et al., 2003, ApJS, 148, 175

[45] Stanghellini C., Baum S.A., O'Dea C.P., Morris G.B., 1990, A&A, 233, 379

[46] Stanghellini C., O'Dea C.P., Dallacasa D., Cassaro P., Baum S.A., Fanti R., Fanti C., 2005, A&A, 443, 891

[47] Urry C.M., Padovani P., 1995, PASP, 107, 803

[48] Weymann R.J., Morris S.L., Foltz C.B., Hewett P.C., 1991, ApJ, 373, 23

[49] Wurtz R., Ellingson E., Stocke J.T., Yee H.K.C., 1993, AJ, 106, 869

[50] Yates M.G., Miller L., Peacock J.A., 1989, MNRAS, 240, 129

Chapter 2

Arecibo telescope and GMRT survey to probe radio source environments via HI and OH absorption

2.1 Introduction

There is general agreement that the energy output from an active galactic nucleus (AGN) is fuelled by the supply of gas to the central engine, which is presumably a supermassive black hole (e.g. Rees 1984). This infall could be triggered by interactions or mergers with companion galaxies, leading to the formation of circumnuclear starbursts and the fuelling of nuclear black holes (e.g. Sanders et al. 1988). Although there have been a number of studies of the gas kinematics of nearby AGN in an effort to understand both the fuelling of this activity and the relationship between the starburst and the AGN, relatively little is known regarding the situation in powerful radio galaxies. Observationally, there is evidence that the central regions of such galaxies contain dust plus ionised, atomic and molecular gas which could be reservoirs of fuel for the central engine. For example, Walsh et al. (1989) have shown that long-wavelength infrared emission, indicative of dust, is correlated with nuclear radio emission. Further, Verdoes Kleijn et al. (1999), from an HST study of 19 Fanaroff-Riley class I (FRI) galaxies, have demonstrated the presence of dust structures in 17 of these. Besides such structures, atomic and molecular gas within $\sim$5–10 kpc of the nuclear region has been seen in many nearby active galaxies, including several well-known

radio galaxies (e.g. Rupen 1997; Lim et al. 2000; Leon et al. 2003).

In the canonical model of an AGN, the nuclear region contains a torus around a supermassive black hole. The torus can consist of ionised, atomic and molecular gas components. An understanding of the distribution and kinematics of the different components of the circumnuclear gas is important both for studying the anisotropy in the radiation field and thereby testing the unified scheme, and for understanding the fuelling of the radio activity. In addition, detection of this gas over a large range of redshifts and source sizes can provide valuable information on the evolution of its properties with redshift and source size (age). At radio wavelengths, the ionized component of this gas may be probed via radio continuum and polarization measurements of compact source components residing within the dense interstellar environments of their parent galaxies. Radio cores, and compact steep-spectrum (CSS) and gigahertz peaked-spectrum (GPS) sources constitute such objects. The structural and polarization asymmetries observed in these sources require an asymmetric distribution of gas in the central regions of the galaxy, which may be related to the infall of gas that fuels the radio source (Saikia et al. 1995; Saikia & Gupta 2003, and references therein).

An important way of probing atomic gas on sub-galactic scales is via HI absorption towards the compact components of CSS and GPS sources or the radio nuclei of larger objects (e.g. van Gorkom et al. 1989; Conway & Blanco 1995; Peck et al. 2000; Pihlström 2001; Vermeulen et al. 2003; Pihlström, Conway & Vermeulen 2003). A pioneering study of HI absorption for a well-defined sample of radio galaxies was made by van Gorkom et al. (1989). This detected HI in 4 out of 29 galaxies, all 4 being dominated by a compact nuclear radio source. More recently, a large survey of CSS and GPS sources detected HI absorption in 33%, with the HI column density being anti-correlated with source size (Vermeulen et al. 2003; Pihlström et al. 2003). The HI spectra exhibit a variety of line profiles, implying significant, sometimes complex, gas motions. van Gorkom et al. (1989) had reported that the HI-absorption features tend to be redshifted from the systemic velocity, suggesting infall of gas. However, recent observations show a more complex situation. For example, Vermeulen et al. find many sources with substantial red and blue shifts, suggesting that atomic gas may be flowing out or falling in, interacting with the jets, or rotating around the nucleus.

Although many recent HI absorption studies have been based on samples of CSS and GPS objects, Morganti et al. (2001) observed extended radio galaxies from the 2-Jy sample of Wall & Peacock (1985), finding the following trends. HI absorption was detected in only 1

of the 10 FRI radio galaxies observed. For FRII radio galaxies, they detected HI absorption in 3 of 4 NLRGS, while absorption was not detected in any of 4 BLRGs. Although this is largely consistent with the predictions of the unified scheme (see van Ojik et al. 1997; Pihlström et al. 2003), the HI is blueshifted from the systemic velocity in 2 of the 3 NLRGs, suggesting that attributing the absorption to just a torus may be too simplistic.

In order to extend these HI investigations to a larger number of GPS and CSS objects, especially those that are of lower luminosity or more distant, and also towards larger sources, we have begun a program using the Arecibo 305-m telescope and the Giant Metrewave Radio Telescope (GMRT). In addition to HI, at Arecibo we have attempted to detect the OH radical which has so far received little attention in this context. In this chapter I present the results of the first phase of our study and examine the dependence of HI column density on projected linear size, redshift, luminosity and host galaxy type by combining our results with those available in the literature. The observations are described in Section 2.2, while the results, with notes on individual sources, are presented in Section 2.3. In Section 2.4, we combine our results with those of similar HI searches and discuss the statistical trends in gas properties with respect to radio-source characteristics and redshift. The results are summarized in Section 2.5.

2.2 Observations

2.2.1 The observed sample

The principal targets of the Arecibo and GMRT observations presented in this chapter were CSS and GPS sources whose redshifted 21-cm HI lines lie in the observing bands of these telescopes. In total, we observed 17 GPS and CSS sources with redshifts of $z \lesssim 1.4$. We also observed 7 large radio galaxies (LRGs; sizes $\gtrsim$15 kpc), and 3 compact flat-spectrum (CFS) objects ($\alpha \lesssim 0.5$ and sizes $\lesssim$15 kpc). At Arecibo, data were also recorded for the OH main-lines in an attempt to detect these in either emission or absorption. The sources and some of their properties are listed in Table 2.1. They form a heterogeneous set having been selected from a number of samples rather than a single well-defined complete sample. Possible selection effects arising from this are discussed later in the chapter.

2.2.2 Arecibo observations and data reduction

The 15 radio sources observed at Arecibo consist of both GPS and CSS objects, and large FRI and FRII sources. The 7 CSS and GPS sources that formed the basic Arecibo sample

Table 2.1: Radio sources observed with the Arecibo telescope and GMRT.

Source name	Alt. name	Opt. id.	Redshift	S_{5GHz}	$\alpha^5_{1.4}$	Spect. class	P_{5GHz}	Str. class	LAS	LLS	Ref.	Radio class
				Jy			10^{25} W/Hz		$''$	kpc		
(1)	(2)	(3)	(4)	(5)	(6)	(7)	(8)	(9)	(10)	(11)	(12)	(13)
J0031−2652	MRC	Q	0.333	0.12	1.03	STP	4.4	U	<1	<4.8	1	CSS
J0034+3025	B2	G	0.1744	0.07	1.06	STP	0.7	SR	∼1.3	2.9	2	CSS
J0040−2043	MRC	G	0.091	0.34	0.51	STP	0.7	CE	<2.4	<4.0	0	CSS
									(15)	(25.5)		
J0119+3210	4C+31.04	G	0.060	1.58	0.47	LFT	1.3	T	0.08	0.1	4	CSS
J0137+3309	3C48	Q	0.3700	5.73	0.82	LFT	245	T	1.2	6.12	5	CSS
J0251+4315	S4	Q	1.311	1.43	−0.45	GPS	449	T?	0.012	0.11	6	GPS
J0255−2153	MRC	G	0.1128	0.17	0.97	STP	0.58	U	<2	<4.0	3	CSS
J0301+3512	NGC1167	G	0.0165	0.86	0.58	STP	0.1	T?	1.13	0.3	7	CSS
J0347−2900	MRC	G	0.1423	0.30	0.90	STP	1.54	U	<5	<12.5	3	CSS
J0513+0157	4C+01.13	BL/G	0.0881†	0.14	0.40	FLT*	0.2	SR	61.2	97.9	8	LRG
J0645+2121	3C166	G	0.2449	1.24	0.58	STP	19.9	T	45.0	171	9	LRG
J0725−0054	PKS	G	0.1273	1.38	0.01	FLT	4.9	CJ	0.03	0.07	10	CFS
J0805+2409	3C192	G	0.0598	1.86	0.88	STP	1.5	T	200	220	11	LRG
J0822+0557	3C198	G	0.08156	0.44	1.13	STP	0.7	D	198	297	12	LRG
J0901+2901	3C213.1	G	0.194	0.78	0.53	STP	7.4	T	5.7	18.2	13	LRG
									(40)	(128)		
J1124+1919	3C258	G	0.165	0.45	0.60	STP	3.0	D	0.10	0.28	7,14	CSS
									(60)	(168)		
J1148+5924	NGC3894	G	0.01075	0.62	−0.31	FLT	0.02	T	0.04	0.008	15	CFS
J1347+1217	4C+12.50	Sy/Q	0.12174	3.10	0.45	LFT	10.8	T	0.09	0.20	16	CSS
J1407+2827	Mrk668	Sy	0.0766	2.41	0.87	GPS	3.1	D?	0.008	0.01	17	GPS
J1516+0015	MRC	G	0.052	1.64	0.40	FLT*	0.98	CJ	0.009	0.01	18	CFS
J1521+0430	4C+04.51	Q	1.296	1.19	1.05	GPS	1208	D	0.137	1.15	19	GPS
J1604−2223	MRC	G	0.141	0.39	0.67	GPS	1.9	D	0.013	0.03	18	GPS
J1643+1715	3C346	G	0.162	1.39	0.78	STP	9.3	T	13.3	37.2	4,13	LRG
J2058+0542	4C+05.78	G	1.381	0.36	0.98	LFT	402	U	<0.4	<3.4	20	CSS
J2250+1419	4C+14.82	Q	0.23478	1.18	0.47	STP	16.8	D	0.2	0.74	21	CSS
J2316+0405	3C459	G	0.2199	1.43	0.95	LFT	19.2	D	8.0	28.0	22	LRG
J2325+4346	OZ438	G	0.145	0.92	0.63	STP	4.7	D	1.6	4.0	7	CSS

Col. 1: source name; col. 2: alternative name; col. 3: optical identification, where BL = BL Lac object, G = galaxy, Q = quasar and Sy = Seyfert galaxy; col. 4: redshift from NASA/IPAC Extragalactic Database (NED); col. 5: total 5-GHz flux density from NED; col. 6: spectral index between 1.4 and 5 GHz; col. 7: integrated radio spectral class, where STP = steep, i.e. $\alpha \geq 0.5$, LFT = low-frequency turnover, GPS = gigahertz peaked and FLT = flat spectrum; col. 8: 5-GHz luminosity in the rest frame of the source; col. 9: radio structure classification, where CE = unresolved component with extended emission, CJ = core-jet source, D = double-lobed, SR = slightly resolved, T = triple and U = unresolved (deconvolved size $\lesssim$ a fifth of the resolution element); cols. 10 & 11: largest projected angular (LAS) and linear (LLS) size in arcsec and kpc respectively, as measured from the outermost radio peaks, or from Gaussian fits to slightly resolved sources (sizes in bracket correspond to the large scale diffuse emission); col. 12: references for the radio structure and col. 13: radio class, where CSS = compact steep-spectrum, GPS = gigahertz peaked-spectrum, CFS = compact flat-spectrum, and LRG = large radio source; see text (Section 2.2.1) for further details.

References for the largest angular sizes – 0: This paper; 1: Kapahi et al. (1998b); 2: Saikia et al. (2002); 3: Kapahi et al. (1998a); 4: Cotton et al. (1995); 5: Feng et al. (2005); 6: Fey & Charlot (2000); 7: Sanghera et al. (1995); 8: NRAO VLA Sky Survey (NVSS) at 1.4 GHz; 9: Neff, Roberts & Hutchings (1995); 10: Bondi et al. (1996); 11: Baum et al. (1988); 12: Fomalont & Bridle (1978); 13: Akujor & Garrington (1995); 14: Strom et al. (1990); 15: Peck & Taylor (1998); 16: Lister et al. (2003); 17: Stanghellini et al. (2001); 18: Beasley et al. (2002; VCS observations); 19: Xiang et al. (2002); 20: de Breuck et al. (2000); 21: Spencer et al. (1989); 22: Thomasson, Saikia & Muxlow (2003)

† The source was observed at $z = 0.084$, the best available redshift at that time.

* The intergrated spectrum exhibits low-frequency steepening.

were selected from well-defined samples of such objects (Fanti et al. 1990; Sanghera et al. 1995, and references therein) and a sample of compact symmetric objects (Taylor, Readhead & Pearson 1996). They have angular sizes of $\lesssim 1''$, with L-band flux densities in the range 0.3−5.4 Jy, and $z \leq 0.3$. Seven LRGs and one CFS object, all within the same flux density and redshift ranges, were added to fill gaps in the observing schedule. Six of the LRGs were chosen from the 3C sample. In addition to the HI observations, we made use of the versatility of the Arecibo spectrometer to simultaneously search for OH in all objects. Sadly, a number had their OH spectra corrupted by radio frequency interference (RFI). See Table 2.2 for the observing log.

Table 2.2: Observational details and results of the Arecibo search for associated HI absorption.

Source name	$S_{1.4GHz}$ Jy	Date	Δv^{HI} km s^{-1}	σ_{FA}^{HI} 10^{-3}	FA_{max}	$W_{50\%}$ km s^{-1}	N(HI) 10^{20} cm^{-2}
(1)	(2)	(3)	(4)	(5)	(6)	(7)	(8)
J0034+3025	0.26	2002 Dec	16.0	2.0	–	–	<1.16
J0119+3210	2.64	2002 Dec	0.72[a]	1.5[a]	0.038[b]	153[b]	12.2±0.14[c]
					0.030[d]	7.6[d]	
J0301+3512	1.84	2002 Dec	24.0	1.3	–	–	<0.75
J0513+0157	0.35	2004 Mar	13.6	2.7	–	–	<1.56
J0645+2121	2.59	2002 Dec	18.0	0.85	–	–	<0.49
		2004 Sep					
J0725−0054	1.40	2002 Dec	14.8	3.6	–	–	<2.08
J0805+2409	5.33	2002 Dec	13.0	0.62	–	–	<0.36
J0822+0557	1.98	2002 Dec	13.6	1.4	–	–	<0.81
J0901+2901	2.00	2002 Nov	16.5	0.46	–	–	<0.27
		2002 Dec					
J1124+1919	0.88	2002 Nov	3.5	1.3	0.095	31.5	5.05±0.13
		2003 Jan					
J1347+1217	5.40	2002 Nov	3.2	0.87	0.012	135	3.03±0.16
		2003 Jan					
J1407+2827	0.82	2002 Nov	13.4	0.66	0.003	326	1.53±0.29
		2003 Jan					
J2250+1419	1.97	2002 Dec	17.7	0.40	–	–	<0.23
J2316+0405	4.68	2002 Dec	17.2	0.49	0.0034	166	1.33±0.27
		2005 Aug					

Col. 1: source name; col. 2: 1.4-GHz flux density from NED; col. 3: dates of observation; col. 4 & 5: the smoothed velocity resolution and the corresponding 1-σ noise for the HI fractional absorption; cols. 6 & 7: peak optical depth and full width at half maximum (FWHM) for the absorption components derived directly from spectra with the velocity resolution given in col. 5, and col. 8: HI column density assuming T_s=100 K. Upper limits and quoted errors are both 3σ. The upper limits assume Δv=100 km s^{-1} and f_c=1.0.

[a] These values are for a spectrum with a total bandwidth of 3.125 MHz. The values for a total bandwidth of 25 MHz were σ_{FA}^{HI}= 0.00051 and Δv^{HI}=5.8 km s^{-1}.

[b] The maximium optical depth and velocity half width given represent just the main absorption component.

[c] The integrated column density is for the total absorption spectrum.

[d] The maximium optical depth and velocity half width given represent just the secondary absorption component.

The Arecibo feed platform and its support cables cause blockage to the incoming wavefront that is focussed on the telescope feed, and also scatter significant amounts of radiation from directions outside of the telescope main beam. The standing-wave pattern resulting

from multipath scattering adds baseline ripples to a line spectrum. For standard Arecibo spectral-line observations of sources emitting little continuum radiation, such effects are minimized via a variant of the position-switching technique. However, when the target emits significant continuum radiation, the standing-wave pattern due to the continuum emission from the target itself is not cancelled by subtracting the position-switched OFF from the ON, and a standing-wave residual remains whose amplitude is proportional to the source intensity. Briggs, Sorar & Taramopoulos (1993) extended the basic position switching method such as to minimize the effect of these residual standing waves. To achieve this, another strong continuum source (of different redshift) is also observed via position switching. Ghosh & Salter (2002) explored this "Double Position-Switching" (DPS) approach at Arecibo for sources having significant continuum emission and found it to be very effective in providing flat spectral baselines. We therefore adopted DPS for the present Arecibo observations of our sample, all of which emit significant continuum radiation.

The present observations recorded the orthogonal linear polarizations of both the λ21-cm HI line, and the λ18-cm OH main-lines. For all sources except J0119+3210 (see below), a bandwidth of 12.5 MHz was processed into 2048 channels, with data acquisition using 9-level quantization. The typical flux-density ratio for the DPS source pairs was 2:1. Weighted averages of the data for individual DPS cycles yielded the final spectra, which were Hanning smoothed. HI absorption was detected in five of the targets (J0119+3210, J1124+1919, J1347+1217, J1407+2827 and J2316+0405), and emission in a sixth (J0301+3512). Neither OH emission nor absorption was detected for any source. The rms noises on the HI and OH spectra of fractional absorption for a given (often smoothed) velocity resolution are listed in Tables 2.2 and 2.13. The peak fractional absorptions, integrated column densities and full-width half maxima for the five sources with detected HI absorption are given in Table 2.2.

2.2.3 GMRT observations and data reduction

Of the 12 radio sources observed with GMRT to search for associated HI absorption, 9 were selected from the sample of Snellen et al. (2002) and the Molonglo Reference Catalogue (MRC; Large et al. 1981; Kapahi et al. 1998a,b). Of the remaining three, two are the CSS objects J0137+3309 (3C48) and J2325+4346, and the third is the flat-spectrum source J1148+5924 (NGC3894). The angular size of each source is less than the spatial resolution of the observations.

HI absorption profiles for CSS sources exhibit a variety of shapes and can be as broad

Table 2.3: Observational details and results of the GMRT search for associated HI absorption.

Source name	Date	Obs. freq	BW	t_{int}	Beam	Peak flux	σ	σ_{FA}^{HI}	FA_{max}	$W_{50\%}$	N(HI)
		MHz	MHz	hr	$''\times''$ °	Jy/b	mJy/b/ch	10^{-3}		km s^{-1}	10^{20}cm^{-2}
(1)	(2)	(3)	(4)	(5)	(6)	(7)	(8)	(9)	(10)	(11)	(12)
J0031−2652	2003 Dec	1065.570	4	3.5	3.9×2.8 19	0.55	1.8	<3.27	–	–	<1.90
J0040−2043	2003 Dec	1301.930	4	2.5	4.2×3.0 3	0.40	0.6	<1.50	–	–	<0.87
J0137+3309*	–	–	4	–	–	20.19	20	<1.00	–	–	<0.06
J0251+4315	2003 Jul	614.894	2	1.0	13.2×6.9 4	0.80	3.6	<4.50	–	–	<2.61
J0255−2153	2003 Dec	1276.425	4	3.0	3.1×2.5 30	0.44	2.8	<6.36	–	–	<3.69
J0347−2900	2003 Dec	1243.461	4	3.0	6.6×2.5 43	2.21	1.6	<0.72	–	–	<0.42
J1148+5924	2003 Jun	1405.299	4	1.5	4.9×2.8 34	0.62	0.6	<0.97	0.034	157	9.66±3.24
J1516+0015	2003 Dec	1350.196	4	3.5	5.1×4.9 59	0.68	0.6	<0.82	–	–	<0.51
J1521+0430	2003 Jul	618.644	2	1.3	29.3×8.0 43	4.34	4.8	<1.11	–	–	<0.64
						0.41					
J1604−2223	2003 Jul	1244.878	4	2.3	6.4×3.1 35	0.72	4.1	<5.69	–	–	<3.30
J2058+0542	2003 Jul	596.558	2	2.0	9.5×6.2 172	2.04	5.0	<2.45	–	–	<1.42
J2325+4346	2003 Jan	1240.529	8	3.2	3.0×1.9 56	0.48	0.7	<1.45	–	–	<0.84

Col. 1: source name; col. 2: year and month of observations; col. 3: redshifted 21-cm frequency; col. 4: baseband bandwidth (BW); col. 5: observing time in hr (excluding calibration overheads); cols. 6 & 7: restoring beam and peak brightness in Jy/beam for the continuum image made using line-free channels; col. 8: rms noise in the spectrum in units of mJy/beam/channel; col. 9: 1-σ noise for the HI fractional absorption; cols. 10 & 11: peak optical depth and FWHM for the absorption components derived directly from the spectra, and col. 12: HI column density in units of 10^{20} cm^{-2}, assuming T_s=100 K; upper limits are 3σ values, and assume Δv=100 km s^{-1}and f_c=1.0. The values of noise and peak optical depth have been estimated from the unsmoothed spectra except for J1148+5924 where the values have been estimated from the spectrum shown in Fig. 2.10.

* See text and Table 2.4 for details of the observations of J0137+3309 (3C48).

Table 2.4: Log for the GMRT observations of J0137+3309 (3C48).

Obs. run	Date	t_{int}* hr	Obs. freq. MHz
1	2003 Oct 11	3.0	1039.8
2	2003 Dec 10	5.0	1040.6
3	2004 Aug 24	7.0	1037.7
4	2004 Aug 25	6.0	1037.7

* Integration time includes calibration overheads.

as several 100 km s^{-1}. Further, the profiles are often either blue- or red-shifted by a few 100 km s^{-1} with respect to the systemic velocity derived from the optical emission lines. To account for these factors, we used a baseband bandwidth (BB BW) of 8 MHz in our first observing run. However, we soon realised that such broad bandwidths are both more difficult to calibrate, and susceptible to RFI. Thus for subsequent runs we used a BB BW of 4 MHz for observations at L-band, which has linearly-polarized feeds, and 2 MHz for those in the 610-MHz band, which has circularly-polarized feeds. This also gave the option of using the 6-MHz IF filter which helped minimise the effects of RFI. The GMRT FX correlator splits the BB BW into 128 frequency channels. The above choice of BB BWs thus implies a velocity resolution of $\sim$7 km s^{-1}, with a total typical velocity coverage of $\sim$1000 km s^{-1}, narrower than that of Vermeulen et al. (2003) by a factor of $\sim$2. Details of the GMRT observations are given in Table 2.3. GMRT calibration requires observations of standard flux density and phase calibrators. In all our observations, except for 3C48, the phase calibrator was observed approximately every 30 min. For bandpass calibration, a flux density calibrator (3C48, 3C147 or 3C286) was observed every 2$-$3 hr.

The CSS quasar J0137+3309 (3C48) was observed on a number of occasions (see Table 2.4) to search for HI absorption at z_{abs}=0.3654, the redshift at which Gupta, Srianand & Saikia (2005) detect outflowing material in the UV, and z=0.3695 and 0.3700, the emission-line redshifts from CO and optical observations respectively (cf. Gupta et al. 2005 or see Chapter 3 for details). The corresponding redshifted frequencies for 21-cm HI absorption lie in the 1060-MHz sub-band of GMRT. RFI at these frequencies not only makes the unambiguous detection of absorption and emission lines difficult, but also affects bandpass stability, thereby reducing the spectral dynamic range. Although a BB BW of 8 MHz was needed to cover the required redshifted frequencies, we chose to use a BB BW of 4 MHz and

move this in frequency for the different observing sessions. Since 3C48 is itself a standard calibrator, it was not required to observe a separate flux density or phase calibrator. However, the high flux density of 3C48 ($\sim$ 20 Jy at 1060 MHz) demands observing an equally strong bandpass calibrator, and for similar durations. We planned our observations such that 3C48 and 3C147 were observable at the same time. In all observing runs on 3C48, we observed it and 3C147 with a duty cycle of about 30 min. A log of the 3C48 observations is presented in Table 2.4. The integration time in column 3 includes the observing time for 3C147.

The NRAO AIPS[1] package was used for the GMRT data reduction. In general, the data of the flux density calibrator, phase calibrator and source were examined at various stages for bad antennas, baselines and time ranges. In particular, the AIPS task SPFLG was invaluable for identifying data affected by RFI. Such data were then flagged out. The complex gains determined from the final cleaned data on the flux density, bandpass, and phase calibrators were used to calibrate the observed visibilties of each program source. A continuum image of a source was then made via the task IMAGR using data averaged over 10−15 line-free channels on both sides of the line. This image was then self-calibrated until a satisfactory map was obtained. This was not difficult as most fields are dominated by a strong point source at the phase centre. This continuum image was then Fourier transformed and subtracted from the visibilty data cube using the task UVSUB. The continuum-subtracted data cube was then imaged (without cleaning) for all 128 channels to obtain a final image cube. The spectrum was obtained by taking a cut across the cube at the pixel correponding to the source location. If necessary, a smooth low-order (usually order one) cubic spline was fitted to take out residual bandpass effects or continuum subtraction errors. The spectra were then corrected to the heliocentric standard of rest[2].

2.3 Observational results

2.3.1 HI observations

From our search for HI absorption towards 27 radio sources (Table 2.1), we made one new detection (3C258) and confirmed 5 previously reported HI absorption systems. In the case of NGC 1167, we have confirmed the double-horn shaped HI emission profile associated with the host E-S0 galaxy, which was reported by Wegner, Haynes & Giovanelli (1993). Of the

[1] AIPS: Astronomical Image Processing System

[2] Optical definition of velocity is used throughout this thesis.

remaining 20 sources, there was no useful data for J1643+1715 (3C346), we have not been able to verify the detection towards J0901+2901 (3C213.1) by Vermeulen et al. (2003) while for J2250+1419 (4C+14.82) our Arecibo spectrum provides significant improvement over the limit of Vermeulen et al. For J0137+3309 (3C48), we do not detect any absorption line in our deeper spectrum although a preliminary detection was reported by Pihlström (2001). The N(HI) upper limits on the remaining 16 sources are new.

The absorption lines detected were fitted with multiple Gaussians to determine the peak optical depth (τ_p) and FWHM (Δv; in km s^{-1}) of spectral components. The parameters derived from the fits are considered in detail in Section 2.3.3. HI column densities were determined using the relations

$$\begin{aligned} \mathrm{N(HI)} &= 1.835 \times 10^{18} \frac{\mathrm{T_s} \int \tau(v)\, dv}{f_c}\, cm^{-2} \\ &= 1.93 \times 10^{18} \frac{\mathrm{T_s} \tau_p \Delta v}{f_c}\, cm^{-2} \end{aligned} \quad (2.1)$$

where $\mathrm{T_s}$ and f_c are the spin temperature (in K) and the fraction of the background emission covered by the absorber respectively. We have assumed $\mathrm{T_s}$=100 K and f_c=1.0. For non-detections, the upper limits on the HI column densities were calculated by replacing the τ_p in the above equation by 3σ upper limits to the peak optical depths estimated from the rms in the spectra, and assuming Δv=100 km s^{-1}. Measured HI column densities, and limits estimated as above, for the Arecibo sources are contained in Table. 2.2. The rms noises in the GMRT spectra, and constraints on the peak HI optical depths and column densities towards the GMRT sources, are presented in the last 3 columns of Table 2.3; the spectra for GMRT non-detections are shown in Fig. 2.1. One of the deepest Arecibo non-detections is shown in Fig. 2.8. The spectra for all detections are presented in Section 2.3.3.

2.3.2 OH observations

The 15 sources observed with the Arecibo telescope were also searched for OH main-line emission and/or absorption. The observations were unaffected by RFI for 9 objects, but none revealed either emission or absorption. Interpretation of these results is presented in Section 2.4.7.

2.3.3 Notes on individual sources

J0034+3025: This galaxy was not detected in either HI or OH. For OH, the segment of the observed spectrum between 1420.14 and 1420.72 MHz was corrupted by the presence of Galactic HI.

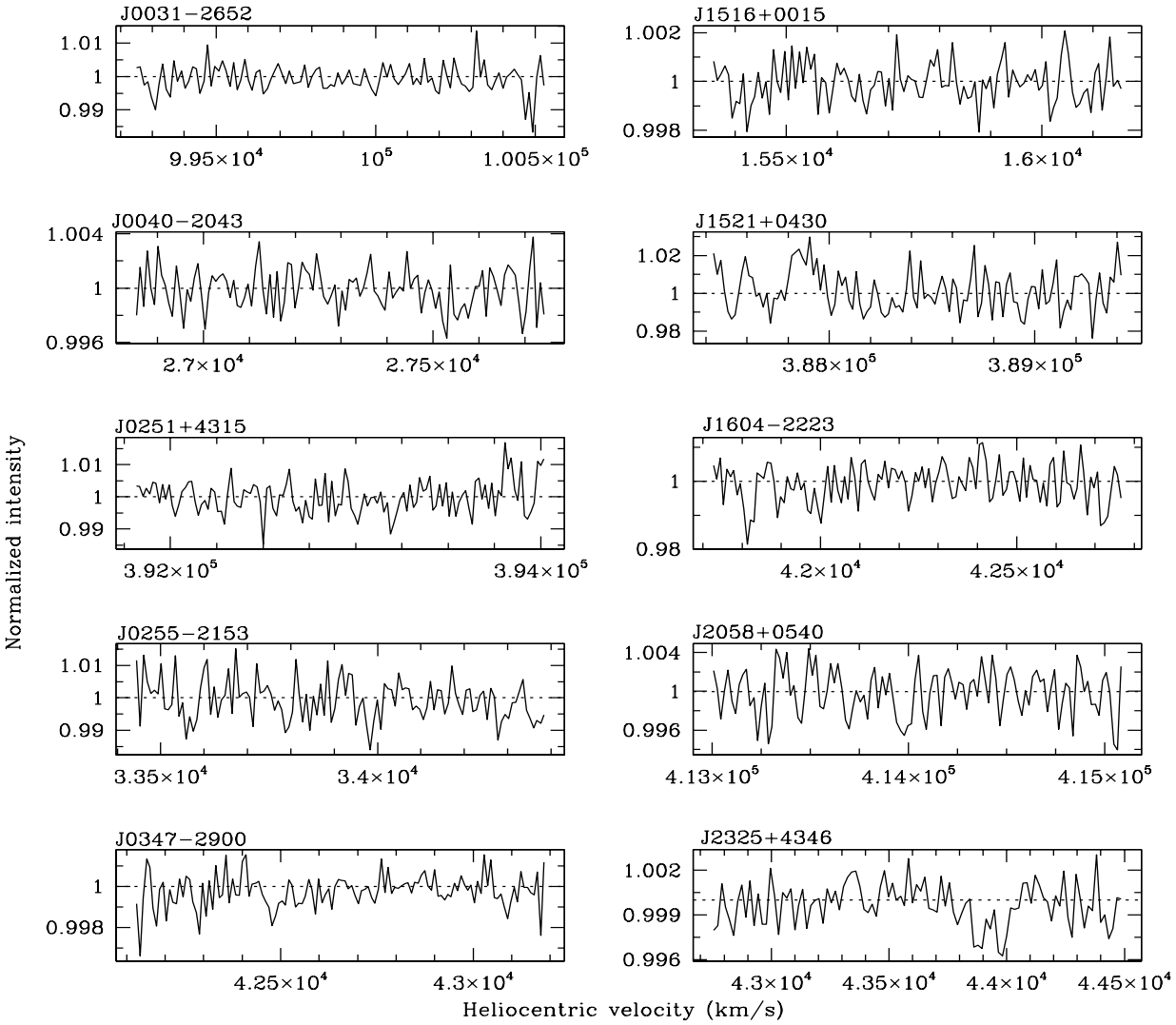

Figure 2.1: GMRT spectra for non-detections. The y-axis shows the normalized intensity while the x-axis shows the heliocentric velocity in km s^{-1}.

J0040−2043: This source was listed earlier as unresolved with an LAS<5″ (Kapahi et al. 1998a). Our GMRT image (Fig. 2.2) at ∼1300 MHz shows an unresolved component of LAS$\lesssim$2.4″ and diffuse emission extending up to at least 15″. From our map, the peak brightness and integrated flux density are 0.40 Jy/beam and 0.61 Jy respectively.

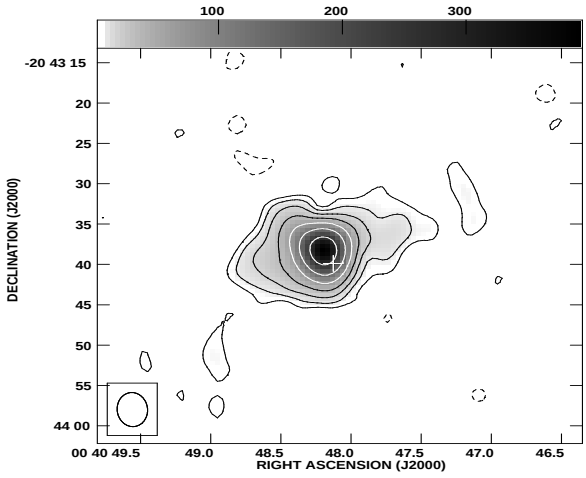

Figure 2.2: GMRT image of J0040−2043 at 1300 MHz with an rms noise of 1.4 mJy/beam. The contour levels are 4×(−1, 1, 2, 4, 8, 16, 32 and 64) mJy/beam. The restoring beam (see Table 2.3) is shown as an ellipse and the position of the optical host galaxy (McCarthy et al. 1996) is marked with a cross.

J0119+3210 (4C+31.04): The mas-scale radio images of this source show two lobes separated by ∼80 mas along a position angle (PA) of ∼110° (Cotton et al. 1995). A faint flat-spectrum component was identified by Giovannini et al. (2001) as the core which, with the absence of any jet-like structures, led them to suggest that the source is oriented close to the plane of the sky, with an angle of inclination to the line of sight, $\theta \geq 75°$.

HI absorption was first detected in this object by van Gorkom et al. (1989) and Mirabel (1990), who discovered that the source also displayed a high velocity component relative to the systemic velocity of the galaxy. The full HI spectrum was subsequently studied in detail via VLBI observations by Conway (1999). He interpreted the distribution of HI opacity as due to an HI disk whose axis is aligned with the jet axis, i.e. close to the plane of the sky. The disk covers the eastern lobe completely, but only the inner part of the western lobe. The high velocity component then arises from small clouds evaporating off the inner edge of the disk. The existence of this disk is further supported by an S-shaped dust lane with an inner PA of ∼25° as seen in HST images (Capetti et al. 2000).

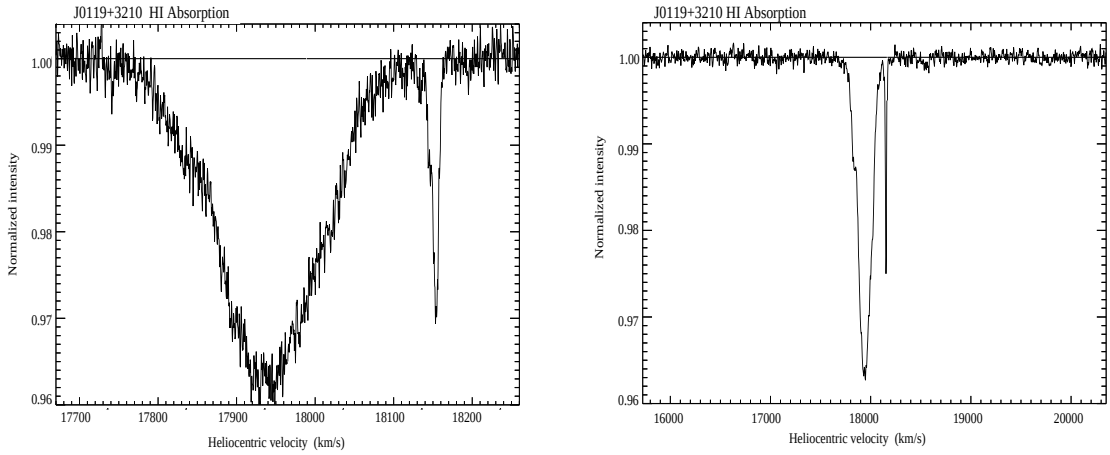

Figure 2.3: HI absorption spectra of J0119+3210 (4C+31.04). Left: The high-resolution spectrum. Right: The low-resolution spectrum with the wider wavelength coverage.

Sadly, the OH main lines are redshifted near to the frequency of GPS-L1 transmissions making them unobservable. Consequently, we decided to observe the HI spectrum at Arecibo with both high and low resolution, using total bandwidths of 3.125 and 25.0 MHz, each with 2048 spectral channels. The high resolution spectrum (Fig. 2.3: left) was used to fit Gaussian components to the main and high-velocity feature separately (Fig. 2.4), while the low resolution spectrum (Fig. 2.3: right) was used to search for any further weak absorption components separated in velocity from the others. The number of Gaussians fitted here, (and for other sources), was the minimum needed to reduce the post-fit residuals to noise.

For the high resolution spectrum, the main component is fitted well by four Gaussians, while the high-velocity feature requires only two. These are summarized in Table 2.5. The low-resolution spectrum shows only a single possible absorption feature separated from the stronger features; a small dip of optical depth $\sim$0.001 at heliocentric velocity $\sim$ 18530 km s^{-1}. This appears at the 3.5σ level on a smoothed version of Fig. 2.3: bottom. Confirmation would be required before its reality could be claimed with confidence.

J0137+3309 (3C48): This enigmatic CSS quasar has a complex radio morphology which has been interpreted as being due to the interaction of the jet with the host galaxy's interstellar medium (Wilkinson et al. 1991). The jet-cloud interaction scenario is further supported

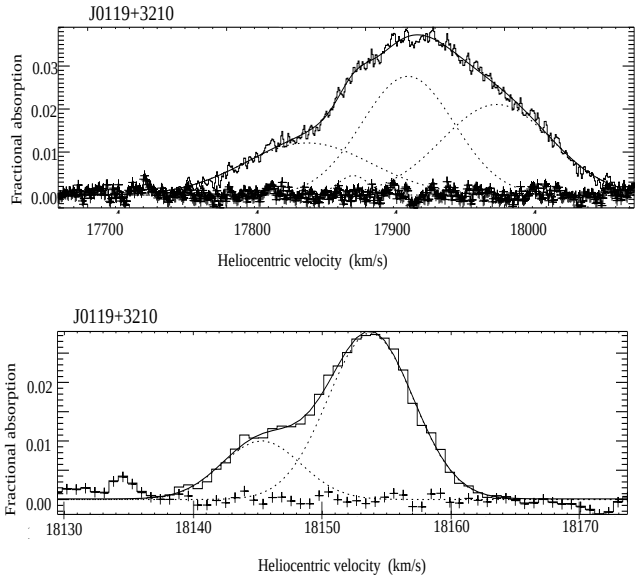

Figure 2.4: Gaussian fits to the HI absorption spectrum of J0119+3210 (4C+31.04). The high-resolution spectrum (histogram) with a velocity resolution of 0.72 km s^{-1} is plotted along with the four-component Gaussian fit to the broad component (top) and two-component Gaussian fit to the narrow high-velocity component (bottom). The individual Gaussians are shown dotted, and their sum as a solid line. The residuals, following subtraction of the Gaussians, are shown as crosses.

Table 2.5: Multiple-Gaussian fits to the broad and narrow absorption features towards the radio source J0119+3210 (4C+31.04).

Id. no.	v_{hel} km s^{-1}	FWHM km s^{-1}	Frac. abs.	N(HI) $10^{20}cm^{-2}$
Broad				
1	17858.2(3.3)	108.2(2.9)	0.0121(0.0001)	2.53(0.07)
2	17891.2(0.7)	26.1(2.2)	0.0045(0.0001)	0.23(0.02)
3	17930.5(0.4)	78.3(0.7)	0.0276(0.0003)	4.17(0.06)
4	17994.4(1.1)	93.7(0.9)	0.0211(0.0001)	3.81(0.04)
Narrow				
1	18145.3(0.06)	7.19(0.09)	0.0100(0.0002)	0.14(0.01)
2	18153.7(0.01)	7.78(0.01)	0.0285(0.0002)	0.43(0.01)

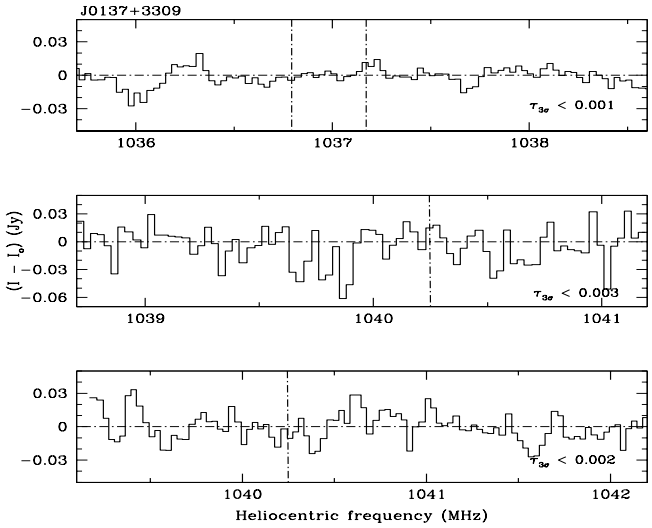

Figure 2.5: GMRT spectra of J0137+3309 (3C48) covering the redshifted 21-cm frequency (marked by vertical lines) corresponding to z_{em}=0.3700 from the optical emission lines, z_{em}=0.3695 from the CO emission spectrum (upper panel) and z_{abs}=0.3654 corresponding to the blue-shifted absorbing material (middle and lower panels) detected in the UV by Gupta et al. (2005).

by the properties of blue-shifted gas detected in forbidden emission lines (Chatzicristou, Vanderriest & Jaffe 1999). We have recently reported the detection of a z_{abs}=0.3654 associated absorption-line system in the UV spectrum (Gupta et al. 2005). A tentative detection of HI absorption towards 3C48 was reported by Pihlström (2001) with a peak optical depth of 0.001 and FWHM of 100 km s^{-1}. Our deep GMRT observations (Fig. 2.5) fail to reveal detectable HI absorption at either the systemic redshift of 3C48 or the redshift corresponding to the gas responsible for the UV absorption lines. For the flux density of 20.3 Jy determined from our observations and assuming f_c=1.0, we obtain a 3σ upper limit on optical depth in the range of 0.001 to 0.003 from the unsmoothed spectra shown in Fig. 2.5.

J0251+4315: The source structure in the VLBA images at 2.3 and 8 GHz show two prominent components, but appear to be better described by a multi-component structure (Fey & Charlot 2000). We detect no significant HI absorption feature associated with this GPS quasar in our GMRT spectrum. The quasar is part of a quasar-galaxy pair with the foreground galaxy G0248+430 (z=0.052) located at a distance of $\sim$15$''$ along a PA of 105° (Sargent & Steidel 1990). The GMRT 616-MHz image (Fig. 2.6) also shows continuum emission from the galaxy which has a flux density of $\sim$25 mJy at this frequency.

J0301+3512 (NGC1167): The Arecibo HI spectrum of this low redshift, E-S0, galaxy,

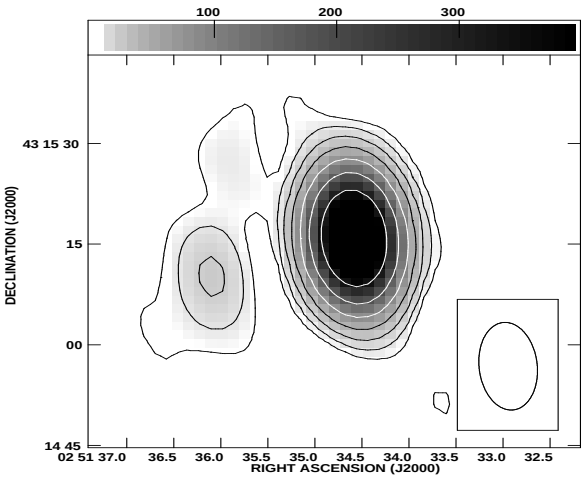

Figure 2.6: GMRT image of J0251+4315 at 616 MHz with an rms noise of 1.6 mJy/beam. The contour levels are $5\times(-2,\ -1,\ 1,\ 2,\ 4,\ 8,\ 16,\ 32$ and $64)$ mJy/beam. The restoring beam (see Table 2.3) is shown as an ellipse. The eastern feature is the foreground galaxy G0248+430.

which has a somewhat complex radio structure (Sanghera et al. 1995), shows no recognizable absorption. However, an emission spectrum typical of a spiral galaxy is seen (Fig. 2.7), where the spectrum has been normalized into Jy beam^{-1}, as is appropriate for line emission. The parameters derived from the spectrum are a HI line flux density of $6.22\pm0.4(1\sigma)$ Jy km s^{-1}, a heliocentric radial velocity of 4965 km s^{-1}, and line widths of 504 and 511 km s^{-1} at 50% of the mean and 20% of the peak signal intensity respectively. These values agree reasonably with those given by Wegner et al. (1993). As implied by the entry for J0301+3512 in Table 2 of Wegner et al., the HI emission from this galaxy is expected to be significantly resolved by the Arecibo beam at 21-cm. Earlier HI observations have been reported by Heckman et al. (1983) and Chamaraux, Balkowski & Fontanelli (1987) who suggested that the HI gas distribution may be influenced by tidal interactions with two disk galaxy companions.

J0513+0157 (4C+01.13): Perlman et al. (1998) classified the parent optical object as a BL Lac on the basis of Ca II break strength and lack of emission lines. However, due to the low signal-to-noise ratio of the spectrum blueward of the Ca II break, its classification as a radio galaxy cannot be ruled out. The OH observations for this source were corrupted by extensive RFI across the band. At the time of observations, the best available redshift for this source was $z = 0.084$. However, Rines et al. (2003) have since measured an improved value of $z = 0.08808 \pm 0.00014$, which would place the HI line towards the edge of the

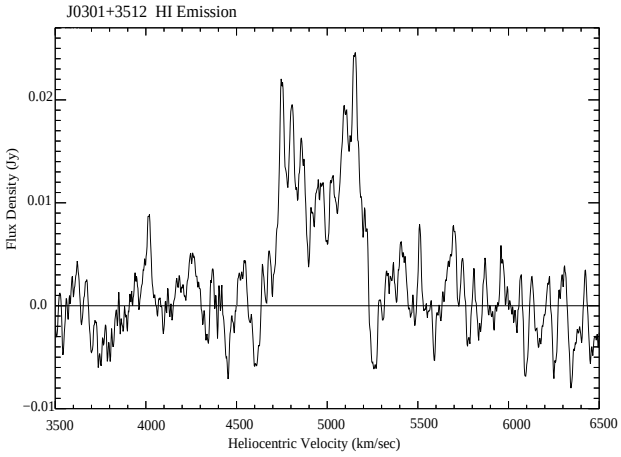

Figure 2.7: The double-horn shaped HI emission profile of the E-SO galaxy NGC 1167 (J0301+3512).

present spectrum. Nevertheless, there is still sufficient baseline to say with confidence that no HI absorption is seen for the source at the 3σ level for the parameters given in Table 2.2.

J0725−0054: This narrow-line radio galaxy, which has an asymmetric radio structure with a knotty jet extending for $\gtrsim$30 mas along PA$\sim -24^\circ$ (Fey & Charlot 1997; Bondi et al. 1996), was observed with the then best available redshift of $z = 0.128$. An improved value of $z = 0.1273 \pm 0.0001$ has since been measured by Eracleous & Halpern (2004). RFI is present over part of the Arecibo HI spectrum, with no HI absorption being detected in the uninterferred spectral region corresponding to $0.1247 < z < 0.1291$. The OH spectrum is RFI-free, and again neither emission nor absorption is seen.

J0805+2409 (3C192): This FRII source has an X-shaped structure (Baum et al. 1988). It is marginally resolved by the Arecibo beam at 1340 MHz, its measured flux density representing ∼84% of the total. No HI absorption was detected, while the OH spectrum was destroyed by RFI from GPS-L1 transmissions.

J0822+0557 (3C198): The OH spectrum for this classical double-lobed FRII radio galaxy (Fomalont 1971), was destroyed by RFI. With its large angular diameter, it is heavily resolved by the Arecibo beam at 1315 MHz, the measured flux density representing only ∼63% of the total. No HI absorption was detected.

J0901+2901 (3C213.1): This galaxy has emission that extends up to $\sim 40''$ in addition to a more compact double-lobed structure (Akujor et al. 1991). A detection of HI absorption in it was recently reported by Vermeulen et al. (2003). The optical depth that they measured was $\tau = 0.0005$, the lowest value detected in their survey by a factor of ∼3. Although this

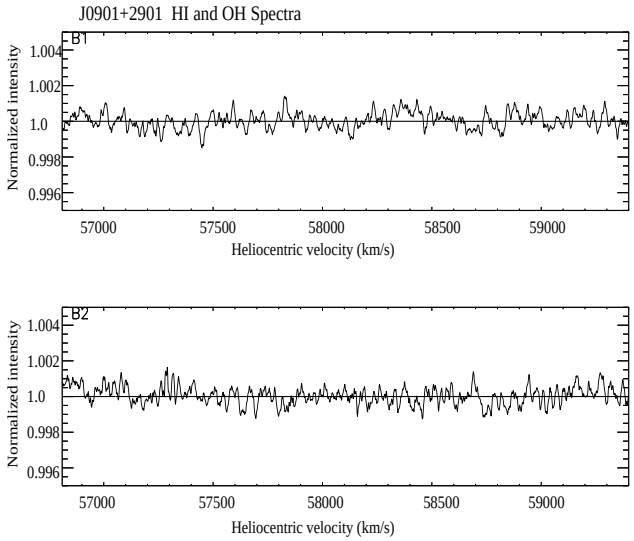

Figure 2.8: HI and OH spectra for J0901+2901 (3C213.1); the y-axis is the spectral intensity normalized by the source flux density, while the x-axis is the heliocentric velocity in km s^{-1}. Top: the HI spectrum with a velocity resolution of 16.5 km s^{-1}; bottom; the OH spectrum with a velocity resolution of 14.1 km s^{-1}.

source provided one of the lowest rms optical depth limits among our Arecibo observations (Fig. 2.8: top), this is still not deep enough to verify the detection of Vermeulen et al. The Arecibo OH spectrum (Fig. 2.8: bottom) shows neither emission nor absorption to a similar optical depth limit as for HI. The spectra shown illustrate one of the deeper Arecibo non-detections.

J1124+1919 (3C258): Deep HI absorption (Fig. 2.9: left) was detected for the first time against the continuum emission from this radio galaxy. This emission is dominated by the CSS source but it is known to also have more extended emission (Strom et al. 1990; Sanghera et al. 1995). The FWHM of the line is at the narrow end when compared to values listed by Pihlström et al. (2003). Despite this, it shows considerable structure, and seven Gaussian components are needed to fit the spectrum satisfactorily (Fig. 2.9: right). These components are listed in Table 2.6.

The individual Gaussian components are narrow, with half-height widths lying between $\sim$4 and 12 km s^{-1}. These narrow widths for the fitted components imply rather low upper limits on T_s values for the HI, the derived values lying in the range $T_s \lesssim 400 - 2000$ K. Compared to other CSS HI-absorption systems, 3C258 exhibits an unusually complex spectrum, with the components having about an order of magnitude narrower velocity widths than for most, though not all, features in other CSS sources (Vermeulen et al. 2003; Pihlström

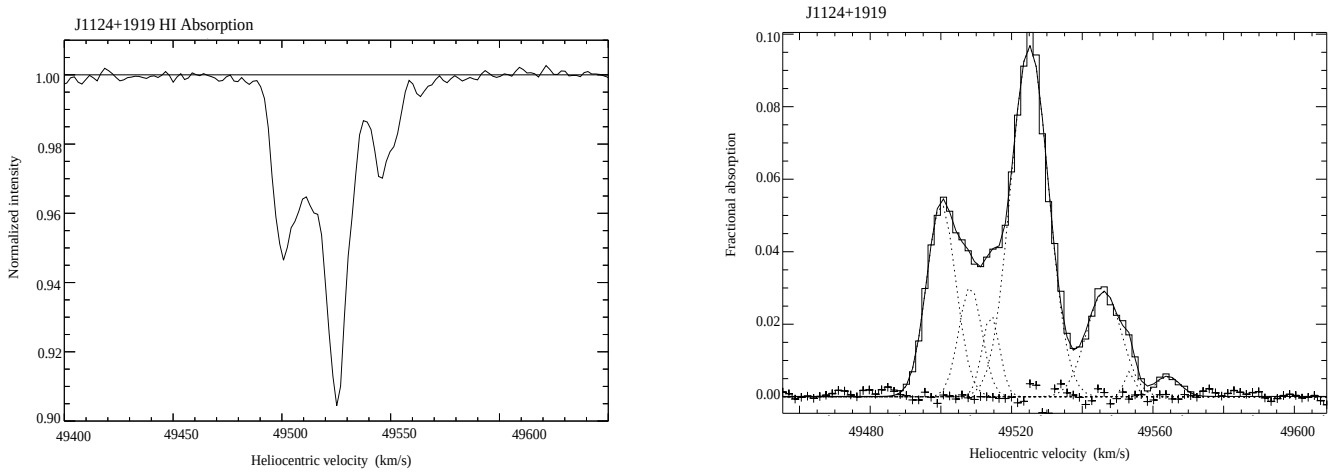

Figure 2.9: Left: The HI absorption spectrum for J1124+1919 (3C258) with a velocity resolution of 3.5 km s^{-1}. Right: The same spectrum plotted as a histogram, overlaid by the seven Gaussians fitted to the spectrum. The meanings of the different line types are as in Fig. 2.4.

Table 2.6: Multiple-Gaussian fit to the HI absorption spectrum of J1124+1919 (3C258).

Id. no.	v_{hel} km s^{-1}	FWHM km s^{-1}	Frac. abs.	N(HI) 10^{20} cm^{-2}
1	49500.1(0.05)	9.69(0.04)	0.0532(0.0013)	1.00(0.03)
2	49508.3(0.09)	7.64(0.28)	0.0304(0.0011)	0.45(0.02)
3	49514.2(0.07)	5.71(0.14)	0.0226(0.0026)	0.25(0.03)
4	49525.1(0.03)	12.50(0.01)	0.0968(0.0002)	2.34(0.01)
5	49546.1(0.06)	11.73(0.11)	0.0290(0.0002)	0.66(0.01)
6	49553.4(0.20)	3.60(0.49)	0.0070(0.0008)	0.05(0.01)
7	49564.2(0.38)	8.23(0.78)	0.0056(0.0002)	0.09(0.01)

et al. 2003). The possibility of the existence of weak, extended line wings, as suggested by Fig. 2.9: left, will have to await deeper integrations for confirmation.

Although detailed modelling of the HI gas seen in absorption in this galaxy will require VLBI imaging of the line and continuum emission, it is difficult to imagine that a single rotating disk/torus would produce such a complex absorption system. This may be a miniature version of 3C236, where jet-ISM interactions play the dominant role in shaping the structure/properties of the object. In fact, the signature of disturbance is perhaps already evident in its optical image. The HST image of 3C258 (de Vries et al. 1997) displays an arc-like structure of high surface brightness, with a larger, fainter tail extending to the northeast, roughly perpendicular to the bright central arc. The radio continuum image (Akujor et al. 1991) is at right angles to the central region and contains the entire VLBI-scale double-lobed structure (Sanghera et al. 1995). Neither OH absorption nor emission were detected against 3C258.

J1148+5924 (NGC3894): The galaxy NGC3894, classified as an E/S0, lies at a redshift of z=0.01075 (de Vaucouleurs et al. 1991). This is in agreement within the error of $\pm 30\,\mathrm{km\ s^{-1}}$, with the redshift of z=0.01068 determined by Karachentsev (1980). Using multi-epoch VLBI observations, Taylor, Wrobel & Vermeulen (1998) suggest that the radio source is oriented well away from the line of sight ($\theta \sim 50^\circ$). Redshifted HI absorption has been detected towards both the approaching and receding jets by Peck & Taylor (1998). Our GMRT spectrum (Fig. 2.10) shows the HI absorption towards this radio source. A good fit to the absorption profile was obtained using six Gaussian components. The best-fit parameters are summarised in Table 2.7. Most of the absorption features are redshifted with respect to the systemic velocity ($\sim 3220\,\mathrm{km\ s^{-1}}$) and could represent the large-scale circumnuclear disk, as well as clouds infalling towards the central engine (Peck & Taylor 1998).

J1347+1217 (4C+12.50): This CSS source is associated with a Seyfert-2 galaxy containing two nuclei separated by $2''$, which may be in the process of merging (Gilmore & Shaw 1986). Broad Paα emission ($\Delta v_{\mathrm{FWHM}} \approx 2600\ \mathrm{km\ s^{-1}}$) suggests that it may contain a buried quasar (Veilleux, Sanders & Kim 1997). The radio structure is highly asymmetric and has a jet on VLBI scales (Xiang et al. 2002; Lister et al. 2003).

Mirabel (1989) detected broad HI absorption against this radio galaxy, followed shortly afterwards by the detection (Mirabel, Sanders & Kazès 1989) of very broad CO(1→0) emission (see also Scoville et al. 2000). The HI spectrum of Mirabel (1989) showed a deep 'core' near the redshift of the galaxy, and apparent very broad wings covering a total

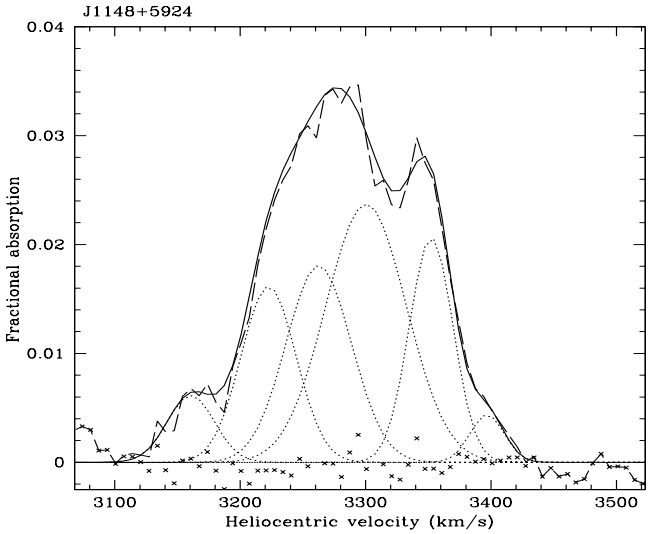

Figure 2.10: The HI absorption spectra (dashed line) for J1148+5924 (NGC3894) obtained with the GMRT. The spectrum has been smoothed using a 5 pixel wide boxcar filter. The six Gaussian components fitted to the absorption profile, the sum of these component fits and residuals are plotted as dotted and solid lines, and crosses respectively.

Table 2.7: Multiple-Gaussian fit to the HI absorption spectrum of J1148+5924 (NGC3894).

Id. no.	v_{hel} km s^{-1}	FWHM km s^{-1}	Frac. abs.	N(HI) $10^{20}cm^{-2}$
1	3161(4)	44.53(6.50)	0.0061(0.0006)	0.52(0.09)
2	3223(2)	51.74(3.58)	0.0161(0.0046)	1.61(0.47)
3	3262(2)	61.44(17.44)	0.0181(0.0024)	2.15(0.67)
4	3300(2)	75.77(12.26)	0.0237(0.0039)	3.47(0.80)
5	3352(2)	41.04(2.88)	0.0207(0.0024)	1.64(0.22)
6	3396(5)	32.26(7.34)	0.0044(0.0008)	0.27(0.08)

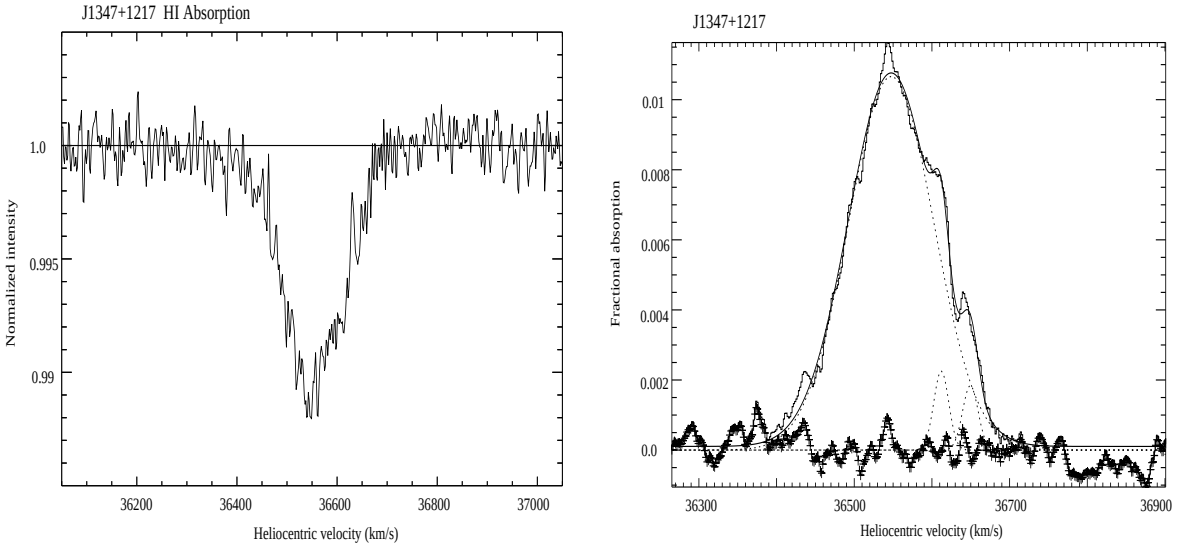

Figure 2.11: Right: The HI absorption spectrum towards the radio source J1347+1217 (4C+12.50) at a spectral resolution of 3.2 km s^{-1}. Left: The Gaussian fits to the components at a velocity resolution of 28.8 km s^{-1}. The line types are as in Fig. 2.4.

Table 2.8: Multiple-Gaussian fit to the HI absorption spectrum of J1347+1217 (4C+12.50).

Id. no.	v_{hel} km s^{-1}	FWHM km s^{-1}	Frac. abs.	N(HI) 10^{20}cm^{-2}
1	36547.4(0.4)	129.9(0.7)	0.0107(0.0001)	2.68(0.03)
2	36611.9(0.8)	22.8(1.8)	0.0023(0.0001)	0.10(0.01)
3	36649(1.7)	23.5(3.9)	0.0018(0.0001)	0.08(0.01)

velocity range of 950 km s^{-1}. Morganti et al. (2004) recently demonstrated that the line wings have an optical depth of $\lesssim$0.002, and cover some 2000 km s^{-1}, extending especially to the blue. We are unable to add anything on these line wings, both because of sensitivity and the presence of RFI at 1370 MHz (v$\sim$ 35500 km s^{-1}). However, our spectrum has higher velocity resolution on the core than previously published examples, and is shown in Fig. 2.11: left. There is an indication of broadening of the redshifted side of the line core, and a smoothed version of the spectrum can be fitted well by three Gaussian components (see Fig 2.11: right), where the best-fit parameters are listed in Table 2.8.

A recently published redshift for this object by Holt, Tadhunter & Morganti (2003) gives $z = 0.12174 \pm 0.00002$ (v = 36497 ± 6 km s^{-1}). This is consistent with our broad core component #1 being associated with the nucleus of the galaxy.

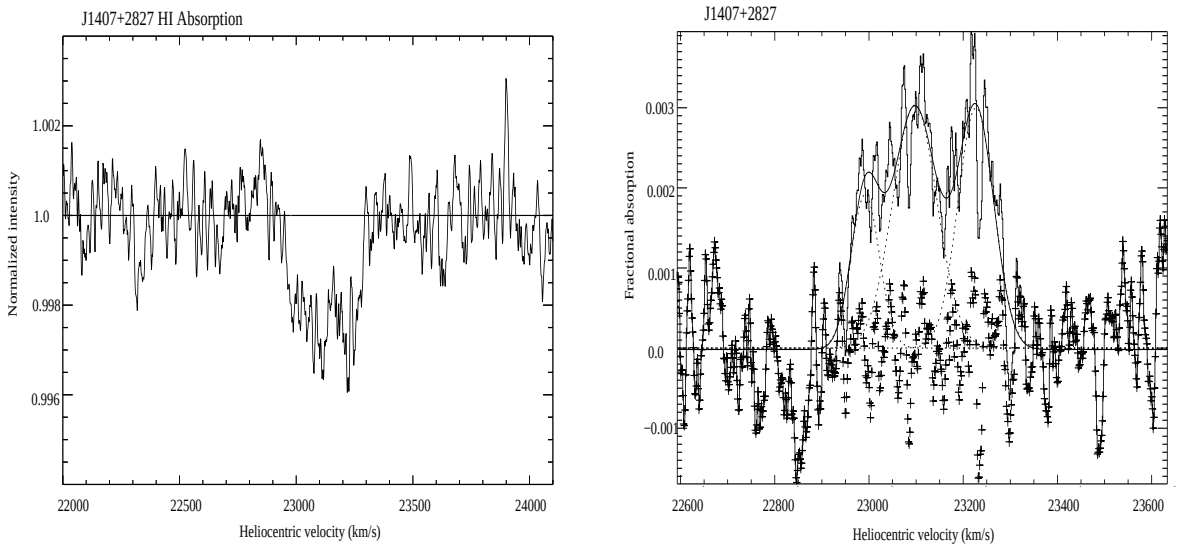

Figure 2.12: Right: The HI absorption spectrum towards the radio source J1407+2827 (Mrk668). Left: The three Gaussian components are overlaid on the spectrum. The line types are as in Fig. 2.4.

From the OH spectrum for J1347+1217 neither emission nor absorption is detected. The source was included in the sample of Darling & Giovanelli (2002), for which they searched for OH megamaser emission at Arecibo. However, they were unable to provide a meaningful limit to such emission for this object due to the effects of standing waves. Dickey et al. (1990) reported a tentative detection of OH emission in this source of peak flux density 1.7 ± 0.2 mJy, and a line width of 305 ± 44 km s^{-1}. Smoothing our spectrum to a velocity resolution of 35 km s^{-1}, we can set an upper limit on the presence of 1667-MHz OH emission of 4.8 mJy (3σ). A deeper integration would be valuable.

J1407+2827 (Mrk668): This GPS object has an asymmetric double-lobed structure and is embedded in a galaxy with highly irregular isophotes, suggesting dynamical disturbance (Stanghellini et al. 1993, 2001). Broad, but weak, HI absorption was detected against this source by Vermeulen et al. (2003). We confirm this (Fig. 2.12), and find evidence of structure within the feature. The line is well fitted by three Gaussian components, the best-fit parameters being listed in Table 2.9.

Recently published redshifts for this object are z=0.07658±0.00013 (Huchra et al. 1990) and z=0.07681±0.00007 (Eracleous & Halpern 2004). Our measured redshift for the fitted HI components of z = 0.07669(5), 0.07704(2) and 0.07748(2) suggest that the two stronger components are consistent with infall on to the galactic nucleus. Unfortunately, the OH spectrum for this source was corrupted by extensive RFI.

Table 2.9: Multiple-Gaussian fit to the HI absorption spectrum of J1407+2827 (Mrk668).

Id. no.	v_{hel} km s^{-1}	FWHM km s^{-1}	Frac. abs.	N(HI) 10^{20}cm^{-2}
1	22991(16)	71(23)	0.0019(0.0001)	0.26(0.08)
2	23097(7)	111(21)	0.0030(0.0001)	0.64(0.12)
3	23227(6)	90(11)	0.0030(0.0001)	0.52(0.07)

J1521+0430 (4C+04.51): In addition to the compact VLBI-scale double of this GPS source, which is unresolved in our 619-MHz observations, there is a separate component towards the south-east at an angular distance of $\sim 1'$ (Fig. 2.13). Comparing this with the NVSS image yields a spectral index of $\sim$0.7 between $\sim$620 and 1400 MHz. It is unclear

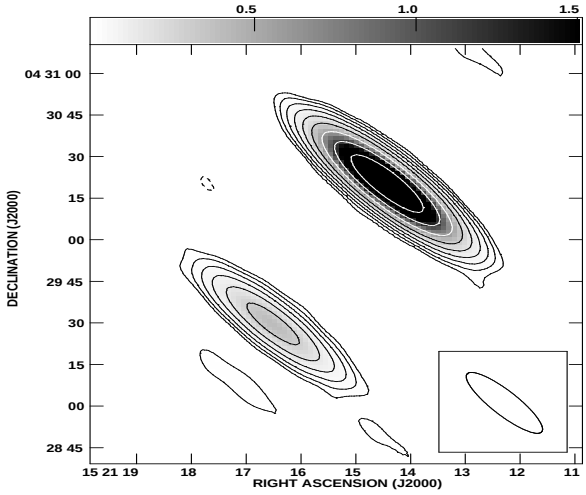

Figure 2.13: GMRT image of J1521+0430 (4C+04.51) at 619 MHz with an rms of 3 mJy/beam. The contour levels are $9\times(-2, -1, 1, 2, 4, 8, 16, 32, 64, 128$ and $256)$ mJy/beam. The restoring beam (see Table 2.3) is shown as an ellipse.

whether this component is related to our source, although $\sim$10% of GPS sources are known to have radio emission beyond kpc scales (Stanghellini et al. 1990). A more sensitive low-frequency image is required to establish whether this feature is related to the GPS source.
J1643+1715 (3C346): The parent galaxy of 3C346 has a double nucleus, the compact, north-western component being coincident with the radio core (Dey & van Breugel 1994). The source has a one-sided radio jet extending for $\sim 2''$ (Cotton et al. 1995), and diffuse

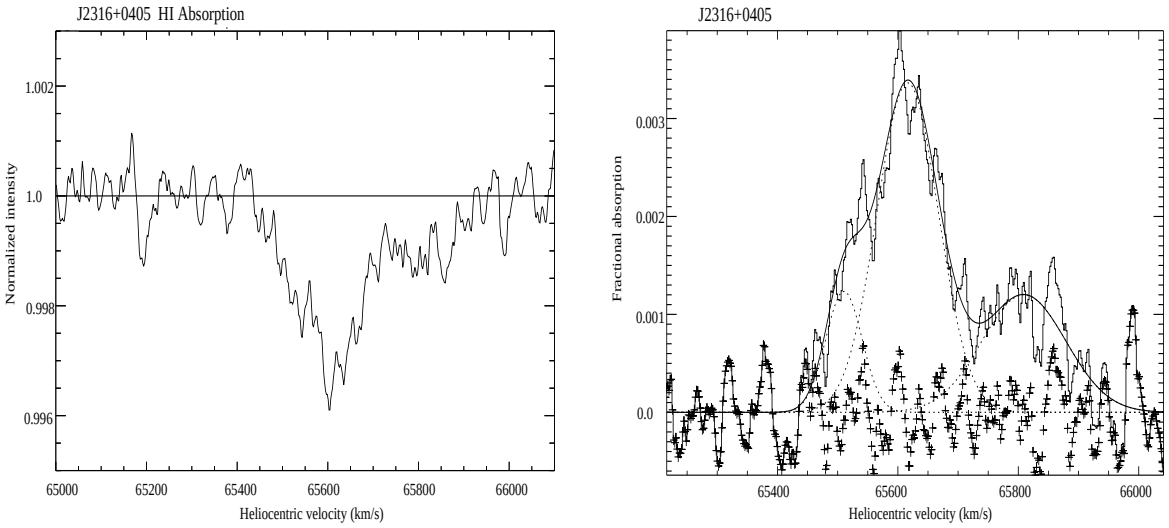

Figure 2.14: Right: The HI absorption spectrum for J2316+0405 (3C459). The velocity resolution is 17.2 km s^{-1}. Left: The same spectrum overlaid by the three Gaussians fitted to it. The line types are same as in Fig. 2.4.

extended emission on a scale of $\sim 12''$ (Akujor et al. 1995). The one-sided jet suggests a small angle of inclination to the line of sight. The HI spectrum for this source were corrupted by the effects of GPS-L2 transmissions. However, the OH spectrum is good, but neither emission nor absorption is detected.

J2250+1419 (4C+14.82): This CSS quasar has an angular size of $0''.2$ (Spencer et al. 1989). It was observed with the spectra centered on the then-best redshift, $z = 0.237$. A value of $z = 0.23478(8)$ has recently been published by Eracleous & Halpern (2004). However, this update is small, and any absorptions near the revised redshift would still lie well within the present spectra. In practice, 4C+14.82 has no detected line of either HI or OH. The N(HI) limit obtained here is a significant improvement over the spectrum of Vermeulen et al. (2003).

J2316+0405 (3C459): This highly-asymmetric radio galaxy with a steep-spectrum core is associated with a galaxy that exhibits tidal tails and has a high infrared luminosity (Thomasson, Saikia & Muxlow 2003). HI absorption has been reported for 3C459 by Morganti et al. (2001) and Vermeulen et al. (2003). The Arecibo HI observations confirm the presence of this line, (see Fig. 2.14: left). Three Gaussian components fit the line well, the best-fit parameters being listed in Table 2.10, and shown in Fig. 2.14: right.

A recently published redshift for this object by Eracleous & Halpern (2004) gives $z = 0.2201 \pm 0.0002$ (v = 65984 ± 60 km s^{-1}) from the average of 4 low-ionization lines. All

Table 2.10: Multiple-Gaussian fit to the HI absorption spectrum of J2316+0405 (3C459).

Id. no.	v_{hel} km s^{-1}	FWHM km s^{-1}	Frac. abs.	N(HI) 10^{20} cm^{-2}
1	65510(27)	71(34)	0.0012(0.0001)	0.17(0.08)
2	65616(6)	121(11)	0.0034(0.0001)	0.80(0.08)
3	65809(31)	164(63)	0.0012(0.0001)	0.38(0.15)

three fitted HI components are significantly blue-shifted relative to this, consistent with outflow from the galactic nucleus.

The OH spectrum for J2316+0405 reveals neither emission nor absorption. Like J1347+1217, this source was also in the Arecibo sample of Darling & Giovanelli (2002), but again no meaningful limit to its OH emission was set by them due to the effects of standing waves.

2.4 Discussion and analyses of the 'full sample'

Of 27 radio sources observed with the Arecibo telescope and GMRT, we detect associated HI absorption towards 6 and HI emission for one other. Individual HI emission- and absorption-line systems have been discussed in detail in Section 2.3.3. The source sample we have used contains objects ranging from the very compact GPS, CSS and CFS sources (sub-kpc to a few kpc) to large radio sources (a few hundred kpc). Hence, these observations allow us to use radio continuum emission spread over a variety of scales as background sources to search for associated neutral gas. In this Section, we combine our results with those of similar HI searches and discuss the trends in gas properties with respect to radio-source characteristics and redshift.

2.4.1 The 'full sample'

In order to have a large enough sample to investigate these trends, we consider the associated HI-absorption searches reported by van Gorkom et al. (1989), Peck et al. (2000), Morganti et al. (2001), Pihlström (2001), Vermeulen et al. (2003) and Pihlström et al. (2003). These used a variety of instruments and set-ups, each having different bandwidths, spectral and spatial resolutions. In the pioneering study of van Gorkom et al. (1989) a total bandwidth of 6.25 MHz ($\sim$1300 km s^{-1}) was used. It detected HI absorption in 4 of 29 galaxies,

all 4 being redshifted relative to the systemic velocity. Vermeulen et al. (2003) used a bandwidth of 10 MHz, which is amongst the widest, to search for HI absorption towards 57 radio sources. They detected absorption towards 19 of these and found a variety of line profiles from Gaussians with a FWHM of $\lesssim$10 km s^{-1} to irregular and multi-peaked profiles which sometimes span a few hundred km s^{-1}. However, the typical value is $\sim$150 km s^{-1}. Further, the velocities of the principal (strongest) absorption component with respect to the systemic velocity ranges from -1420 to $+318$ km s^{-1}, with 16 of 19 ($\sim$85%) lying within the velocity range of $\pm$500 km s^{-1}. In this phase of our study of HI absorption towards radio sources, the velocity coverage for the Arecibo and GMRT observations were typically $\sim$2500 and 1000 km s^{-1} respectively. The GMRT observations would hence not detect the highest-velocity components of Vermeulen et al., should these be present.

In the samples considered here, the spatial resolution was usually insufficient to resolve compact sources, while larger sources are often resolved. In order to have an average value of the HI optical depth, or an upper limit over the scale length of the radio source, we have considered only sources for which most of the radio continuum emission lies well within the resolution element of the telescopes. In some sources, HI absorption may be detected against a single component, such as the radio cores in PKS1318$-$43 and 3C353 (e.g. Morganti et al. 2001). We will consider such cases in the later chapters, along with our HI absorption observations towards the cores and hotspots of radio sources.

With the above selection criterion, we obtain a sample of 96 radio sources, called the 'full sample', which is a heterogeneous superset of sources with available HI information. This sample is the combination of Tables 4.1 and 2.11, with the omission of J1643+1715 for which no HI data exists. Data for J0901+2901 was taken from Vermeulen et al. (2003), rather than from our own shallower observations of the source. The sample includes 27 GPS, 35 CSS, 13 CFS and 21 LRG sources (see Table 2.12). Amongst the GPS and CSS objects, 17 are associated with quasars, and 44 with galaxies. All the CFS sources are associated with quasars or BL Lac objects, while the LRGs are associated with galaxies. The sample spans a wide range of $\sim$6 orders of magnitude in luminosity at 5 GHz and $z\lesssim$1.4. However, since most sources have been selected from strong flux-density limited samples, luminosity and redshift are strongly correlated (see Fig. 2.15).

2.4.2 HI column density versus linear size

For the 'full sample', Fig. 2.16 shows the 21-cm HI column density against projected linear size measured from the outermost peaks of radio emission. T_s =100 K and full coverage of

Table 2.11: Sample of radio sources from literature forming the 'full sample'.

Source name	Alt. name	Opt. ID	Redshift	P_{5GHz} 10^{25} W/Hz	LAS $''$	LLS kpc	Ref.	Radio class	N(HI) 10^{20} cm^{-2}	V_{shift} km s^{-1}	Ref.
(1)	(2)	(3)	(4)	(5)	(6)	(7)	(8)	(9)	(10)	(11)	(12)
J0025−2602	OB-238	G	0.322	112	0.65	3.02	1	CSS	2.42	−30	V
J0111+3906	OC314	G	0.669	99	0.005	0.036	2,3 4,5	GPS	79.8	0	C1
J0141+1353	3C49	G	0.621	134	0.99	6.71	6,7	CSS	1.17	−185	V
J0157−1043	OC-192	Q	0.616	121	5.0	33.8	8	LRG	<1.00		V
J0201−1132	3C57	Q	0.669	219	1.7	11.9	8	CSS	<0.68		V
J0224+2750	3C67	G	0.310	25.8	2.5	11.3	7,9	CSS	<1.45		V
J0348+3353	3C93.1	G	0.243	13.6	0.56	2.14	10	CSS	<1.38		V
J0401+0036	3C99	G	0.426	33.8	4.2	23.3	11	LRG	<1.13		V
J0410+7656	4C76.03	G	0.599	336	0.14	0.93	7,10	CSS	2.66	315	V
J0431+2037	OF247	G	0.219	32.8	0.29	1.02	10,12	GPS	3.66	318	V
J0503+0203	OG003	Q	0.585	196	0.011	0.073	13	GPS	6.65	43	C1
J0521+1638	3C138	Q	0.759	78.6	0.68	4.98	6,7,14	CSS	<0.48		V
J0522−3627	MRC	G	0.0553	5.6	8.3	9.1	15	CSS	<0.39		M
J0542+4951	3C147	Q	0.545	841	0.94	5.98	16	CSS	<0.30		V
J0556−0241		G	0.235	4.6	0.02	0.09	17	GPS	<6.27		V
J0609+4804	3C153	G	0.277	34.7	5.4	22.4	11	LRG	<0.65		V
J0627−3529	MRC	G	0.0546	1.5	0.21	0.23	18	CFS	<1.35		M
J0741+3112	OI363	Q	0.635	237	0.006	0.042	13,19	GPS	<0.99		V
J0815−0308	3C196.1	G	0.198	3.0	3.0	9.7	11	CSS	<1.53		V
J0834+5534	4C55.16	G	0.242	85	11.0	41.4	20	LRG	1.14	−399	V
J0901+2901	3C213.1	G	0.194	7.4	5.7	18.2	21	LRG	0.12	−14	V
J0909+4253	3C216	Q	0.670	301	9.2	64.5	22	LRG	1.30	102	V
J0927+3902	4C39.25	Q	0.695	654	3.1	22.1	23	LRG	<0.99		V
J0939+8315	3C220.3	G	0.685	145	7.8	55.1	24	LRG	<0.49		V
J0943−0819		G	0.228	15.5	0.020	0.072	25	GPS	<1.27		V
J0954+7435		G	0.695	462	0.021	0.150	26,27	GPS	<2.51		V
J1035+5628	OL553	G	0.459	72.0	0.034	0.020	28	GPS	<1.38		V
J1104+3812	Mrk421	G	0.0300	0.14	0.075	0.044	29	CFS	<1.16		G
J1120+1420	4C14.41	G	0.362	37.7	0.084	0.420	30	GPS	<0.61		V
J1159+2914	4C29.45	Q	0.729	241	5.4	39.1	31	LRG	<1.91		V
J1206+6413	3C268.3	G	0.371	55.0	1.3	6.6	7,16	CSS	2.07	258	V
J1220+2916	NGC4278	G	0.0022	0.0003	0.029	0.001	32	CFS	<2.12		G
J1252+5634	3C277.1	Q	0.321	26.8	1.7	7.7	7,16	CSS	<0.72		V
J1308−0950	OP-010	G	0.464	166	0.60	3.47	1	CSS	<1.35		V
J1313+5458		Q	0.613	72.0	0.037	0.250	26	GPS	<1.80		V
J1326+3154	4C32.44	G	0.370	88.7	0.056	0.285	33,34	GPS	0.75	−471	V
J1356+0515	NGC5363	G	0.004	0.0004	<1.0	<0.08	35	CFS	10.3	96	G
J1357+4354		G	0.646	58.6	0.017	0.117	36	GPS	35.42	−165	V
J1400+6210	4C62.22	G	0.431	108	0.065	0.362	10	GPS	1.99	−258	V
J1407−2701	IC4374	G	0.022	0.056	0.009	0.004	25	CFS	<3.28		G
J1415+1320	OQ122	G/Q	0.247	12.9	0.114	0.437	27,37	CSS	10.60	0	C2
J1421+4144	3C299	G	0.367	39.4	11.2	56.7	21	LRG	<0.70		V
J1443+7707	3C303.1	G	0.267	10.1	1.8	7.3	16	CSS	<1.50		V
J1540+1447	4C14.60	Q	0.605	120	4.0	26.8	38	LRG	<0.62		V
J1546+0026		G	0.550	104	0.010	0.064	27	GPS	<1.05		V
J1556−7914	MRC	G	0.1501	24.8	0.120	0.300	39	CFS	3.82	*a*	M
J1642+6856	4C69.21	Q	0.751	236	8.3	61.0	40	LRG	<1.34		V
J1653+3945	Mrk501	G	0.034	0.35	0.025	0.017	29	CFS	<4.44		G
J1658+0741	OS092	Q	0.621	130	7.1	48.2	40	LRG	<1.56		V
J1815+6127		Q	0.601	54.2	0.010	0.068	26	GPS	4.61	−1258	V
J1816+3457		G	0.245	5.6	0.039	0.149	27	CSS	5.40	−184	P1
J1819−6345	MRC	G	0.0645	4.2	0.33	0.400	1,42	CSS	21.2	−160	M
J1821+3942	4C39.56	G	0.798	319	0.47	3.53	10,12	CSS	1.75	−806	V
J1823+7938		G	0.224	6.3	0.015	0.054	26	GPS	<26.7		V
J1829+4844	3C380	Q	0.692	912	1.3	9.0	16	CSS	<0.19		V

Source name	Alt. name	Opt. ID	Redshift	P_{5GHz} $\times 10^{25}$ W/Hz	LAS $''$	LLS kpc	Ref.	Radio class	N(HI) $\times 10^{20}$ cm^{-2}	V_{shift} km s^{-1}	Ref.
(1)	(2)	(3)	(4)	(5)	(6)	(7)	(8)	(9)	(10)	(11)	(12)
J1831+2907	4C29.56	G	0.842	357	2.6	19.9	43	LRG	<1.70		V
J1845+3541	OU373	G	0.764	126	0.010	0.071	44	GPS	<11.0		V
J1944+5448	OV573	G	0.263	17.3	0.040	0.161	12,44	GPS	5.21	−1420	V
J1945+7055		G	0.101	1.5	0.035	0.064	45	GPS	30.0	−172	P2
J2022+6136	OW637	Q	0.227	32.4	0.010	0.036	28	GPS	<0.38		V
J2052+3635		G	0.355	117	0.060	0.297	46	GPS	7.69	−95	V
J2137−2042	OX-258	G	0.635	223	0.200	1.370	1,47	CSS	<1.18		V
J2151+0552		G	0.74	112	0.004	0.027	48	GPS	<16.9		C1
J2202+4216	DA571	Q	0.069	3.8	0.010	0.013	2	CFS	<1.74		G
J2209−2331	MRC	G	0.087	1.7	<2.0	<3.2	49	CSS	<1.35		G
J2255+1313	3C455	Q	0.543	102	2.6	16.5	21	LRG	0.45	30	V
J2257−3627	MRC	G	0.006	0.009	0.030	0.004	47	CFS	<1.74		G
J2321+2346	3C460	G	0.268	9.4	5.8	23.7	41	LRG	<2.04		V
J2333−2343	OZ-252	G	0.048	0.46	0.037	0.034	28	CFS	<1.54		G
J2344+8226		Q	0.735	292	0.267	1.940	10,12	GPS	<0.75		V
J2355+4950	OZ488	G	0.238	22.3	0.069	0.256	50,51	GPS	3.01	−12	V

Col. 1: source name; col. 2: alternative name; col. 3: optical identification; col. 4: redshift; col. 5: 5-GHz luminosity in the rest frame of the source; cols. 6 & 7: largest projected angular (LAS) and linear (LLS) size in arcsec and kpc respectively, as measured from the outermost radio peaks; col. 8: references for the radio structure; col. 9: radio class; col. 10: HI column density or a 3σ upper limit to it; col. 11: the shift of the primary HI component relative to the systemic velocity as measured from the optical emission lines, with a negative sign indicating a blue-shift, and column 12: references for the HI observations.

References for the structural information and LLS: 1: Tzioumis et al. (2002); 2: Pearson & Readhead (1988); 3: Owsianik, Conway & Polatidis (1998); 4: Zensus et al. (2002); 5: Baum et al. (1990); 6: Fanti et al. (1989); 7: Saikia et al. (1995); 8: Reid, Kronberg & Perley (1999); 9: Sanghera et al. (1995); 10: Dallacasa et al. (1995); 11: Neff, Roberts & Hutchings (1995); 12: Saikia et al. (2001); 13: Stanghellini et al. (2001); 14: Akujor et al. (1991); 15: Keel (1986); 16: Lüdke et al. (1998); 17: Petrov et al. (2005); 18: Venturi et al. (2000); 19: Saikia & Kulkarni (1998); 20: Whyborn et al. (1985); 21: Akujor & Garrington (1995); 22: van Breugel et al. (1992); 23: Browne et al. (1982); 24: Jenkins, Pooley & Riley (1977); 25: Beasley et al. (2002); 26: Taylor et al. (1994); 27: Peck et al. (2000); 28: Fomalont et al. (2000); 29: Giovannini, Feretti & Venturi (1999); 30: Bondi, Garrett & Gurvits (1998); 31: Antonucci & Ulvestad (1985); 32: Giovannini et al. (2001); 33: Mutel et al. (1981); 34: Fey, Clegg & Fomalont (1996); 35: van Gorkom et al. (1989); 36: Taylor et al. (1996); 37: Perlman et al. (1996); 38: Ulvestad, Johnston & Weiler (1983); 39: Morganti et al. (2001); 40: Murphy, Browne & Perley (1993); 41: Giovannini et al. (1988); 42: Ojha et al. (2004); 43: Spencer et al. (1989); 44: Xu et al. (1995); 45: Taylor & Vermeulen (1997); 46: Philips & Mutel (1981); 47: Fomalont et al. (2003); 48: Stanghellini, O'Dea & Murphy (1999); 49: Kapahi et al. (1998a); 50: Polatidis et al. (1995); 51: Taylor et al. (2000).

References for HI observations: C1: Carilli et al. (1998); C2: Carilli et al. (1992); M: Morganti et al. (2001); G: van Gorkom et al. (1989); M: Morganti et al. (2001); P1: Peck et al. (2000); P2: Peck, Taylor & Conway (1999); V: Vermeulen et al. (2003)

a Errors in the systemic velocity are too large.

Table 2.12: Summary of the 'full sample'.

Radio class.	Detections	Non-detections
GPS	12	15
CSS	11	24
CFS	3	10
LRG	5	16

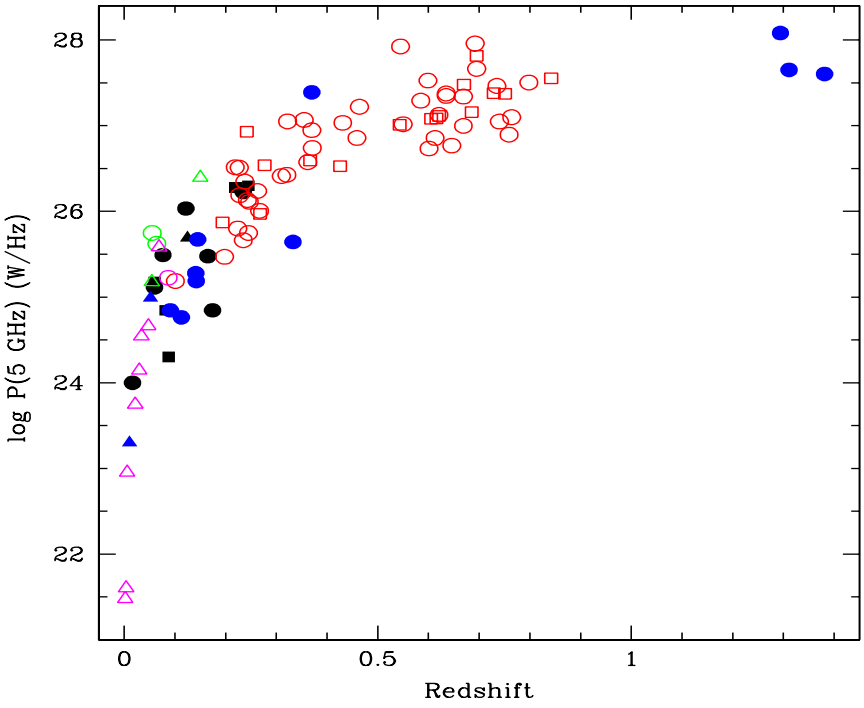

Figure 2.15: Luminosity of sample sources at 5 GHz versus redshift. The solid symbols are sources from our observations, while open symbols are data from the literature. The circles denote GPS/CSS, triangles CFS, and squares LRG sources. For our observations, black represents Arecibo sources and blue the GMRT's. Red corresponds to data from Vermeulen et al. (2003) and Pihlström et al. (2003), green to Morganti et al. (2001) and magenta to van Gorkom et al. (1989).

the background source have been assumed to estimate the column density using eqn. 2.1. The upper limits on N(HI) for non-detections are calculated from the 3σ limit on the peak optical depth as estimated from the spectrum or given in the literature, and a velocity width of 100 km s^{-1}. Fig. 2.16 shows that the incidence of HI absorption is much higher for the compact sources. In particular, for sources with sizes less than 15 kpc, HI absorption is detected towards 26 out of 75 ($\sim$35%), while only 5 out 21 ($\sim$25%) LRG sources exhibit HI absorption. The detection rate ($\sim$45%) is maximum for the most compact class, the GPS sources (see Table 2.12).

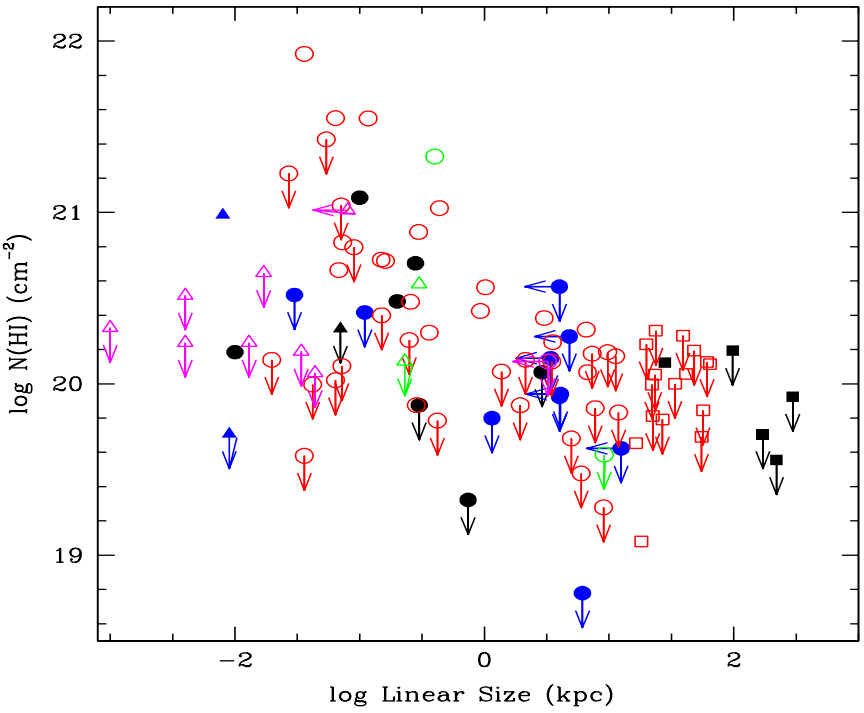

Figure 2.16: HI column density as a function of projected linear source size. Arrows mark the 3σ upper limit to the column density or to the linear size. See the caption of Fig. 2.15 for the meaning of the colours and symbols.

The 'full sample' shows an anticorrelation between N(HI) and source size (Fig. 2.16), which was first noted by Pihlström et al. (2003) for the GPS and CSS sources. However, when interpreting this relationship, we need to bear in mind the uncertainties in the values of spin temperature and covering factor for the different objects. The small sources are capable of probing gas closer to the AGN so that T_s could be greater than 100 K. If this were so, it would only increase our estimate of the column density for the smaller sources thereby increasing the difference in HI column density between the smaller and the larger

objects. The other factor influencing this relationship is the covering factor which could in principle increase the estimates of column density for the larger objects. This depends on the size of the absorber relative to the radio source and can be probed by high-resolution spectroscopic observations.

It is relevant to note that the above anti-correlation is consistent with the optical spectroscopic observations of van Ojik et al. (1997), who interpreted deep troughs in the Lyα emission profiles of 18 high-redshift ($z > 2$) radio galaxies (HZRGs) to be absorption due to HI with column densities in the range 10^{18}–$10^{19.5}$ cm^{-2}. Interestingly, 9 out of the 10 HZRGs with sizes <50 kpc have associated HI absorption compared with 2 of the 8 larger (>50 kpc) ones.

2.4.3 HI column density versus redshift

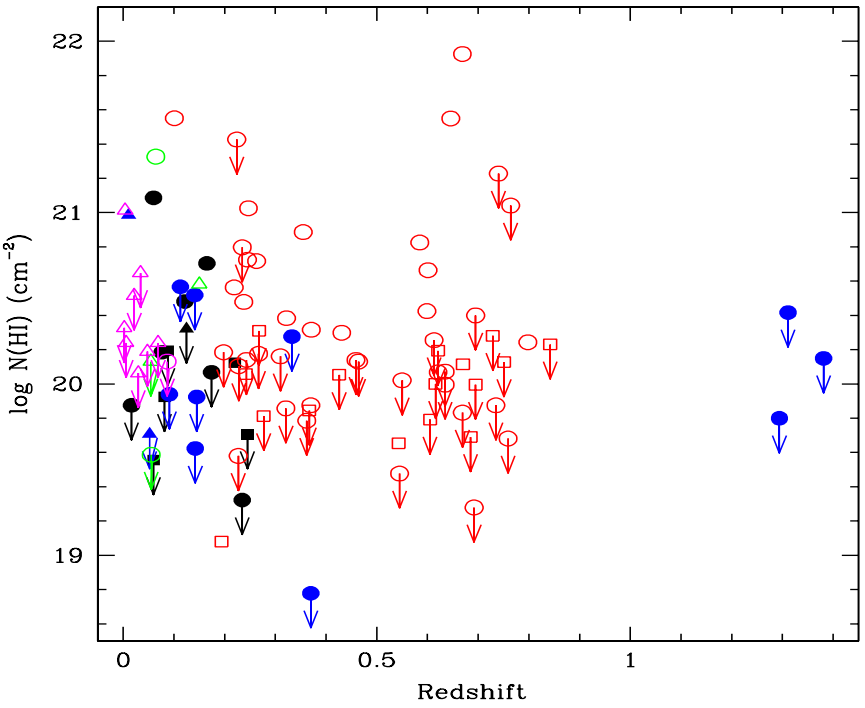

Figure 2.17: HI column density versus redshift. See the caption of Fig. 2.15 for the meaning of the colours and symbols.

The HST studies of distant galaxies ($z \lesssim 1$; e.g. Abraham et al. 1996; Brinchmann et al. 1998) show remarkable morphological evolution and suggest larger incidences of mergers and interactions in the past. Such mergers and interactions could trigger gas inflows towards the central regions of galaxies leading to the formation of circumnuclear starbursts, tori and the

fuelling of nuclear black holes (Sanders et al. 1988; Hopkins et al. 2005). It is thus pertinent to enquire whether the environments of radio sources as probed by HI absorption bear any signature of evolution with redshift. In Fig. 2.17, we plot N(HI) against redshift for the 'full sample'. Clearly, no trend exists for N(HI) to vary with redshift out to z∼1. However, it is

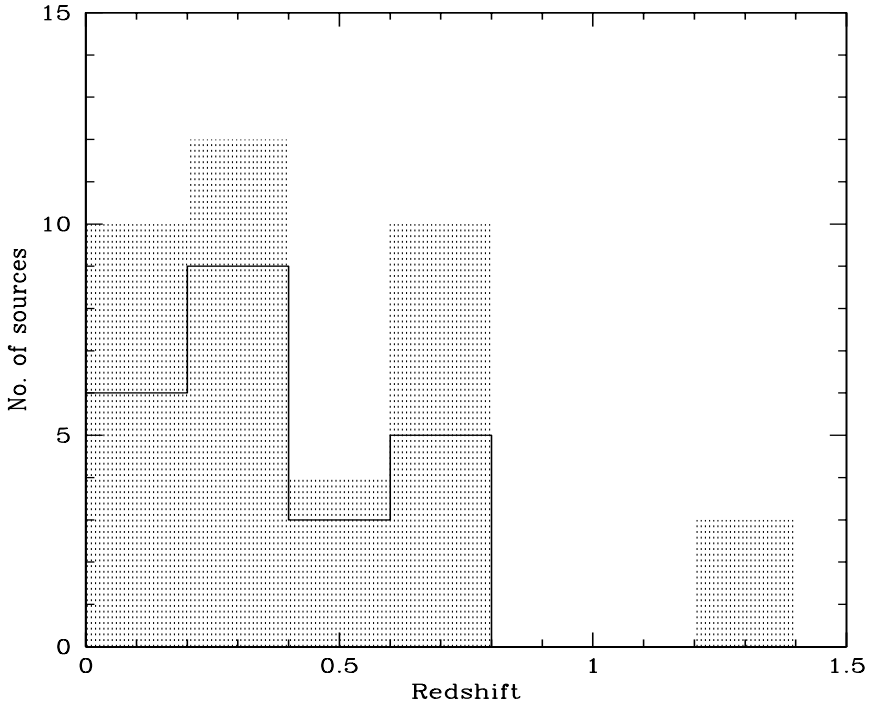

Figure 2.18: The redshift distribution of GPS and CSS sources with detections (solid lines) and non-detections (shaded).

possible that any such dependence is not apparent for the 'full sample' as it contains sources with luminosities and projected linear sizes spanning a range of ∼6 orders of magnitude in luminosity and 4−5 orders of magnitude in linear size. The parameter space can be constrained to some extent by considering the sub-sample consisting of just GPS and CSS sources. This sub-sample contains 62 sources with projected linear size $\leq$ 15 kpc, ∼85% of which have luminosities spanning ∼2 orders of magnitude. In Fig. 2.18, we plot the redshift distributions of these GPS and CSS sources separately for HI detections and non-detections. There is again no significant difference between the two redshift distributions, suggesting that the environments of radio sources on GPS and CSS scales as probed by the neutral gas component are similar at different redshifts. Interestingly, this is consistent with the polarization asymmetry study of CSS and larger sources by Saikia & Gupta (2003), whose sample of sources with z $\lesssim$ 2, showed no significant dependence of polarization asymmetry

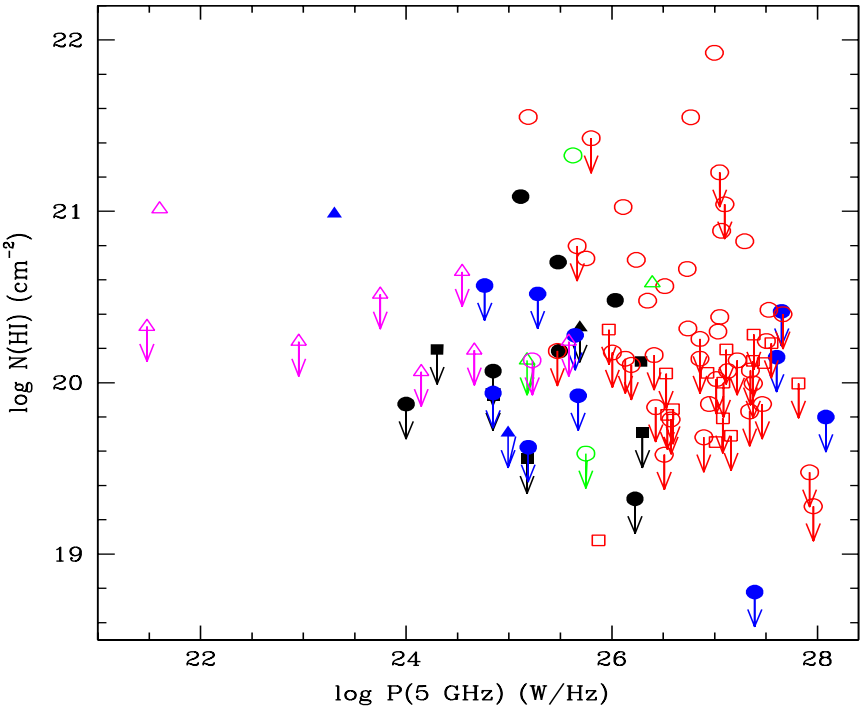

Figure 2.19: HI column density versus source luminosity at 5 GHz. See the caption of Fig. 2.15 for the meaning of the colours and symbols.

on redshift. A study of the fraction of CSS objects at different redshifts in well-defined complete samples led Röttgering et al. (1996) to suggest that the environments of CSS objects do not vary significantly with redshift.

2.4.4 HI column density versus luminosity

It is widely believed that the energy output from AGN is triggered by the supply of gas to the central engine, presumably a supermassive black hole (e.g. Rees 1984). Although there have been a number of studies of gas kinematics of nearby AGN in order to understand the fuelling of such activity, the dependence of N(HI) on radio luminosity could provide clues towards understanding this phenomenon. In Fig. 2.19, we plot N(HI) against the radio luminosity at 5 GHz for the 'full sample'. There is no significant dependence of N(HI) on radio luminosity. Since luminosity and redshift are strongly correlated in our sample, and there is no signficant dependence of N(HI) on redshift, this is not surprising. In order to investigate any dependence of N(HI) on luminosity, one requires objects with HI detections covering a large range in luminosity but confined to a narrow range in redshift for a given class of objects. Although the 'full sample' contains objects spanning ∼4 orders of

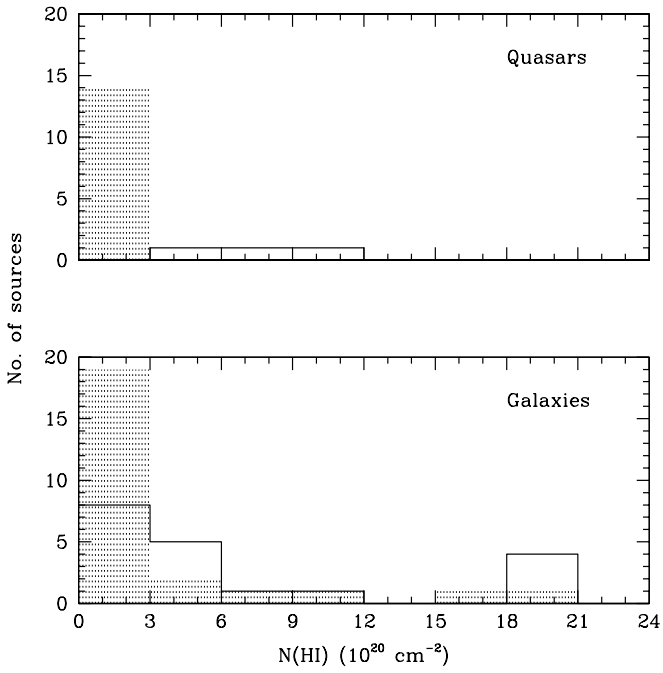

Figure 2.20: The HI column density distribution of GPS and CSS quasars (top panel) and galaxies (bottom panel). The detections are marked by solid lines while the shaded regions represent non-detections. The four detections and one non-detection for galaxies with log N(HI)>19.5 have been put in the last bin.

magnitude in luminosity in the lowest redshift range, these are a "mixed bag" with very few HI detections. To address this issue satisfactorily, one needs to extend the HI observations of radio sources, especially GPS and CSS sources, to lower luminosities of (say) 10^{24} to 10^{26} W Hz^{-1} at 5 GHz in the redshift range of $\sim$0.5 to 1.

2.4.5 HI absorption and unification scheme

GPS and CSS sources are believed to be young, seen at an early stage of their evolution. Though it is possible that a few (e.g. 3C216) have small linear sizes due to projection effects, most are intrinsically compact (Fanti et al. 1990). An interesting question is whether GPS and CSS objects are consistent with the unification scheme for radio galaxies and quasars, in which quasars are inclined at $\lesssim$45° to the line of sight while galaxies lie at larger angles (Barthel 1989; Antonucci 1993). Saikia et al. (1995, 2001) have argued from the prominence of their radio cores and their symmetry parameters that GPS and CSS objects are also consistent with the unified scheme. If this is so, then one might also expect a dependence of the detection rate of HI absorption and HI column density on the optical identification

of the parent optical object and the fraction of emission from the core (Pihlström et al. 2003), which is a reasonable statistical indicator of the source-axis orientation to the line of sight (Orr & Browne 1982; Kapahi & Saikia 1982). The exact nature of the variation would depend on the form of the disk or torus, which is not well constrained.

As a first step, we examine whether the detection rate for the 'full sample' is consistent with the unification scheme. In Fig. 2.20, we plot the N(HI) distributions for GPS and CSS quasars and galaxies. Clearly, the detection rate (∼40%) for galaxies is higher than that (∼20%) for quasars. Considering just the GPS and CSS objects separately, one finds for both a similar difference in the detection rates for galaxies and quasars. This is consistent with the unification scheme for radio galaxies and quasars (e.g. Pihlström et al. 2003). In addition to the geometries considered by Pihlström et al., the distribution of HI gas clouds is likely to be anisotropic since those close to the path of the radio jet, or within the ionisation cone, are more likely to be ionised than those at larger angles to the jet axis (cf. van Ojik et al. 1997). This could also cause a higher detection rate of HI absorption in galaxies relative to quasars in the framework of orientation-based unification schemes.

2.4.6 Blue-shifted absorption lines: Evidence of jet-cloud interaction?

Although blue-shifted absorption lines could arise due to either halo gas or circumnuclear gas kinematically affected by nuclear winds and/or radiation pressure, the jet-cloud interaction may also play a significant role in sub-galactic sized radio sources. The structure of GPS and CSS sources often appear to be affected by the ambient gas, suggesting dynamical interaction with the external medium (Spencer et al. 1991; Schilizzi et al. 2000). In particular, CSS sources tend to be more asymmetric in brightness, location and polarization of the outer radio components when compared with the larger sources (Saikia et al. 1995, 2001; Arshakian & Longair 2000; Saikia & Gupta 2003). They also tend to exhibit high rotation measures (see O'Dea 1998 for a review). The properties of emission-line gas in the galaxies associated with these sources are also consistent with the scenario in which ambient gas has been ionized and accelerated by shocks caused by interaction with the radio jet (Gelderman & Whittle 1994; Labiano et al. 2005). In the archetypal CSS object 3C48, the kinematical properties of the blue-shifted gas seen in emission and absorption (Chatzichristou et al. 1999; Gupta et al. 2005) suggest that the complex radio structure of the source (Wilkinson et al. 1991) could be caused by interaction of the jet with the external gas clouds. Baker et al. (2002) studied absorption spectra for a sample of quasars from the Molonglo Reference Catalogue, and find a slight excess of blue-shifted C IV absorption

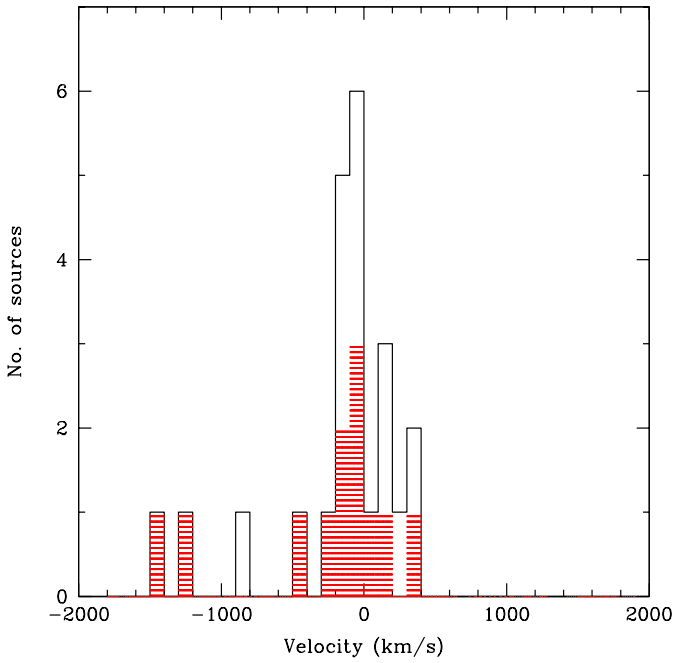

Figure 2.21: The distribution of velocities for the principal HI absorption components with respect to the systemic velocity estimated from optical lines. The solid line is the distribution for both CSS and GPS sources, while the distribution for GPS sources is shown shaded.

lines in CSS sources as compared with the larger objects. van Ojik et al. (1997) also found an excess of blue-shifted Lyα absorption lines in their sample of HZRGs, and demonstrated strong evidence for interaction of the radio sources with the external environment. In principle jet-cloud interaction can give rise to blue-shifted as well as red-shifted absorption lines. However, 21-cm absorption line experiments towards a sample of sources which are randomly oriented towards us could exhibit an excess of blue-shifted lines. This is because for the sources oriented significantly away from the sky plane, a) the approaching jet will be stronger than the receding jet due to Doppler boosting and b) the absorbing gas towards the approaching hot-spot/lobe is likely to have a larger covering factor. These effects possibly play a role in the fact that broad ($\sim$1000 km s^{-1}) 21-cm absorption lines towards radio sources, which are believed to have been caused by jet-cloud interaction, are all blue-shifted (Morganti, Tadhunter & Oosterloo 2005).

In Fig. 2.21, we plot the distribution of the velocity shifts of the principal (strongest) 21-cm absorption component detected towards the CSS and GPS sources in the 'full sample'. Though hampered by small number statistics, and uncertainties in systemic velocities (cf.

Mirabel 1989; Morganti et al. 2001), the distribution does indicate that HI absorption for compact radio sources tends to be blue-shifted, with 14 out of the 23 principal absorption-line components displaying such an effect. We note that the skewness of the distribution comes largely from the principal components detected towards GPS sources. Of the 12 principal components detected towards GPS sources 8 have blue-shifted velocities with respect to the systemic velocity. Also, 6 of the 9 secondary components listed by Vermeulen et al. (2003) appear blue shifted. The higher incidence of blue-shifted features suggests that some of the absorption could be due to gas clouds accelerated by the radio jets.

2.4.7 OH upper limits and their implications

The parameters of the 9 OH non-detections at Arecibo are given in Table 2.13. Upper limits on thermal OH column densities can be calculated using

$$\mathrm{N(OH)} = 2.25 \times 10^{14} \frac{\mathrm{T_{ex}} \int \tau_{1667}(v) dv}{f_c} \,\mathrm{cm^{-2}} \tag{2.2}$$

where $\tau_{1667}(v)$ is the optical depth in the 1667.3-MHz OH main-line at radial velocity v km s^{-1} (e.g. Boyce & Cohen 1994). Below, a covering factor of f_c=1.0 and an excitation temperature of $\mathrm{T_{ex}} = 10\,\mathrm{K}$ are adopted.

Assuming that a velocity equivalent width from the HI absorption of $v_{eq} = \int \tau_{HI}(v)\, dv/\tau_p$ also applies to any OH absorption, we have computed upper limits on the OH column densities for the three sources for which both an HI absorption was detected at Arecibo and an upper limit obtained on OH absorption. An optical depth limit for OH absorption of $3 \times \sigma_{\mathrm{FA}}^{\mathrm{OH}}$ was adopted, where $\sigma_{\mathrm{FA}}^{\mathrm{OH}}$ is taken from Table 2.2. This gives column densities of $< 1.1{\times}10^{14}\,\mathrm{cm^{-2}}$ for J1124+1919, $< 3.3{\times}10^{14}\,\mathrm{cm^{-2}}$ for J1347+1217, and $< 10.9{\times}10^{14}\,\mathrm{cm^{-2}}$ for J2316+0405. Of course, these upper limits need to be interpreted in the light of the expected covering factors for potential absorbers obtained from VLBI imaging and the projected angular sizes for diffuse clouds and giant molecular clouds (GMCs). However, we note that in our Galaxy, the column densities of OH in respect of diffuse clouds are of the order of N(OH)$\sim 10^{13-14}\,\mathrm{cm^{-2}}$, while typical values for GMCs are N(OH)$\sim 10^{15-16}\,\mathrm{cm^{-2}}$. The above column densities for HI and OH imply an abundance ratio of N(HI)/N(OH) $\geq 4.4 \times 10^6$ for J1124+1919, the source with the lowest limit on N(OH), given the values adopted for HI and OH temperatures, and assuming similar covering factors. Other upper limits for N(OH) in Table 2.13 are 3-σ values, assuming a velocity width of 100 km s^{-1}. It is worth noting for comparison that although there are only a few OH main-line absorption systems seen towards extragalactic sources, the typical column density for the detected ones is a few times $\sim 10^{15}$ cm^{-2} (e.g. Darling & Giovanelli 2002; Kanekar & Chengalur 2002).

Table 2.13: Results of the Arecibo search for associated OH absorption.

Source name	Date	$\sigma_{\rm FA}^{\rm OH}$ 10^{-3}	$\Delta v^{\rm OH}$ km s^{-1}	N(OH) 10^{14} cm^{-2}	log $L_{\rm OH}^{\rm max}$ $h_{75}^{-2} L_\odot$
J0034+3025	2002 Dec	2.0	13.6	<13.5	<1.99
J0645+2121	2002 Dec	0.79	15.3	<5.3	<2.89
	2004 Sep				
J0725−0054	2002 Dec	2.1	12.6	<14.2	<2.48
J0901+2901	2002 Nov	0.46	14.1	<3.1	<2.34
	2002 Dec				
J1124+1919	2002 Nov	0.61	13.4	<1.1	<1.96
	2003 Jan				
J1347+1217	2002 Nov	0.37	12.4	<3.3	<2.25
	2003 Jan				
J1643+1715	2004 Mar	0.44	13.3	<3.0	<2.42
J2250+1419	2002 Dec	0.38	15.1	<2.6	<2.41
J2316+0405	2002 Dec	0.76	14.7	<10.9	<3.03

Col. 1: source name; col. 2: dates of the observations; col. 3 & 4: 1-σ noise for the OH fractional absorption, and the corresponding velocity resolution; cols. 5 & 6: upper limits on OH column density and luminosity, respectively.

The non-detection of megamaser emission in the 1667-MHz OH main line provides us with upper limits on (isotropic) luminosities for this line. Adopting exactly the prescription used for their non-detections by Darling & Giovanelli (2002), which assumes a line intensity of $1.5\,\sigma$, a rest-frame velocity width of 150 kms^{-1}, and normalization to $H_0 = 75\,{\rm km\ s^{-1} Mpc^{-1}}$, $q = 0$, upper limits have been computed for the 9 sources for which good OH spectra were obtained. These luminosity limits, $L_{\rm OH}^{\rm max}$, are given in Table 2.13 and agree within 5% with the estimated luminosities were the same cosmological parameters to be adopted as in the rest of this paper. Of these, only J1347+1217 and J2316+0405 were detected by IRAS. From the $L_{\rm OH}$ – $L_{\rm FIR}$ relationship of Kandalian (1996), Darling & Giovanelli predict luminosity values for these of $L_{\rm OH} = 2.36$ and $2.46\,h_{75}^{-2}\,L_\odot$ respectively. While our luminosity upper limit for J2316+0405 is about a factor of 4 higher than the predicted OH luminosity, that for J1347+1217 is somewhat below the predicted value. As mentioned in Section 2.3.3, obtaining a spectrum of increased sensitivity for J1347+1217 would be valuable.

In respect of the non-detection of OH emission for any of the AGNs observed by us, we

note that Darling & Giovanelli (2000) failed to detect any OH megamasers for a sample of nearby AGNs situated in quiescent (non-interacting) systems and which were undetected by IRAS.

2.5 Summary

I have presented results from our search for associated HI absorption towards 27 radio sources using the Arecibo and GMRT telescopes. We detect HI absorption towards six and HI emission from one. A totally new HI absorption system was detected against the radio galaxy 3C258, whose HST image shows an odd-shaped galaxy with an arc-like structure of high surface brightness, and a larger, fainter tail extending to the northeast. The HI absorption spectrum is complex, possibly due to interaction of the compact radio source with the ISM of the host galaxy.

The results of OH observations towards 9 sources using the Arecibo telescope have also been presented. No OH was detected towards any of these sources either in emission or absorption. The estimated column densities for HI and OH imply an abundance ratio of $N(HI)/N(OH) \gtrsim 4 \times 10^6$ for 3C258, adopting typical values for HI and OH temperatures and assuming similar covering factors.

We combine our HI results with similar, previously published, searches to obtain a 'full sample' of 96 radio sources consisting of 27 GPS, 35 CSS, 13 CFS and 21 LRG radio sources. The resultant sample has sources with 5-GHz integrated powers spread over $\sim$6 orders of magnitude and with redshifts up to $z \sim 1.4$. In the 'full sample' we find that the HI absorption detection rate is highest ($\sim$45%) for the compact GPS sources and least ($\sim$25%) for the large LRG sources. The anticorrelation between the HI column density and source size for GPS and CSS sources, first noted by Pihlström et al. (2003), is confirmed by this enlarged sample. This anticorrelation is also consistent with the optical spectroscopic results of van Ojik et al. (1997) as described in Section 2.4.2.

The HI column density, as probed by 21-cm absorption, shows no significant dependence on redshift for the 'full sample' or for the sub-sample of GPS and CSS sources, suggesting that the environments on these scales are similar for different redshifts. This is consistent with finding no significant dependence of polarization asymmetry of the lobes of these sources on redshift (Saikia & Gupta 2003), and also the fraction of these small sources being similar at different redshifts (Röttgering et al. 1996).

For the subsample of CSS and GPS sources, the HI detection rate is higher ($\sim$40%) for galaxies than for quasars ($\sim$20%). This is consistent with the unification scheme. The

principal (strongest) absorption component detected towards GPS sources appears to be blue-shifted in 65% of the cases. This could be due to the interaction of radio sources with the ambient environment.

Bibliography

[1] Abraham R.G., van den Bergh S., Glazebrook K., Ellis R.S., Santiago B.X., Surma P., Griffiths R.E., 1996, ApJS, 107, 1

[2] Akujor C.E, Garrington S.T., 1995, A&AS, 112, 235

[3] Akujor C.E., Spencer R.E., Zhang F.J., Davis R.J., Browne I.W.A., Fanti C., 1991, MNRAS, 250, 215

[4] Antonucci R., 1993, ARA&A, 31, 473

[5] Antonucci R.R.J., Ulvestad J.S., 1985, ApJ, 294, 158

[6] Arshakian T.G., Longair M.S., 2000, MNRAS, 311, 846

[7] Baker J.C., Hunstead R.W., Athreya R.M., Barthel P.D., de Silva E., Lehnert M.D., Saunders R.D.E., 2002, ApJ, 568, 592

[8] Barthel P.D., 1989, ApJ, 336, 606

[9] Baum S.A., Heckman T., Bridle A., van Breugel W., Miley G., 1988, ApJS, 68, 643

[10] Baum S.A., O'Dea C.P., de Bruyn A.G., Murphy D.W., 1990, A&A, 232, 19

[11] Beasley A.J., Gordon D., Peck A.B., Petrov L., MacMillan D.S., Fomalont E.B., Ma C., 2002, ApJS, 141, 13

[12] Bondi M., Padrielli L., Fanti R., Ficarra A., Gregorini L., Mantovani F., 1996, A&AS, 120, 89

[13] Bondi M., Garrett M.A., Gurvits L.I., 1998, MNRAS, 297, 559

[14] Boyce P.J., Cohen R.J., 1994, A&AS, 107, 563

[15] Briggs F.H., Sorar E., Taramopoulos A., 1993, ApJ, 415, 99

[16] Brinchmann J. et al., 1998, ApJ, 499, 112

[17] Browne I.W.A., Orr M.J.L., Davis R.J., Foley A., Muxlow T.W.B., Thomasson P., 1982, MNRAS, 198, 673

[18] Capetti A., de Ruiter H.R., Fanti R., Morganti R., Parma P., Ulrich M.H., 2000, A&A, 362, 871

[19] Carilli C.L., Perlman E.S., Stocke J.T., 1992, ApJ, 400, L13

[20] Carilli C.L., Menten K.M., Reid M.J., Rupen M.P., Yun M.S., 1998, ApJ, 494, 175

[21] Chamaraux, P., Balkowski C., Fontanelli I.P., 1987, A&AS, 69, 263

[22] Chatzichristou E.T., Vanderriest C., Jaffe W., 1999, A&A, 343, 407

[23] Conway J.E., 1999, NewAR, 43, 509

[24] Conway J.E., Blanco P.R., 1995, ApJ, 449, 131

[25] Cotton W.D., Feretti L., Giovanni G., Venturi T., Lara L., 1995, ApJ, 452, 605

[26] Dallacasa D., Fanti C., Fanti R., Schilizzi R.T., Spencer R.E., 1995, A&A, 295, 27

[27] Darling J., Giovanelli R., 2000, NAIC Newsletter No. 31, p. 7

[28] Darling J., Giovanelli R., 2002, AJ, 124, 100

[29] de Breuck C., Röttgering H., Miley G., van Breugel W., Best P., 2000, A&A, 362, 519

[30] de Vaucouleurs G., de Vaucouleurs A., Corwin H.G. Jr., Buta R.J., Paturel G., Fouque P., 1991, Third Reference Catalogue of Bright Galaxies, Springer-Verlag, Berlin

[31] de Vries W. H. et al., 1997, ApJS, 110, 191

[32] Dey A., van Breugel W.J.M., 1994, AJ, 107, 1977

[33] Dickey J.M., Planesas P., Mirabel I.F., Kaàżes I., 1990, AJ, 100, 1457

[34] Eracleous M., Halpern J.P., 2004, ApJS, 150, 181

[35] Fanti C. et al., 1989, A&A, 217, 44

[36] Fanti R., Fanti C., Schilizzi R.T., Spencer R.E., Nan Rendong, Parma P., van Breugel W.J.M., Venturi T., 1990, A&A, 231, 333

[37] Feng W.X., An T., Hong X.Y., Zhao Jun-Hui, Venturi T., Shen Z.-Q., Wang W.H., 2005, A&A, 434, 101

[38] Fey A.L., Clegg A.W., Fomalont E.B., 1996, ApJS, 105, 299

[39] Fey A.L., Charlot P., 1997, ApJS, 111, 95

[40] Fey A.L., Charlot P., 2000, ApJs, 128, 17

[41] Fomalont E.B., 1971, AJ, 76, 513

[42] Fomalont E.B., Bridle A.H., 1978, AJ, 83, 725

[43] Fomalont E.B., Frey S., Paragi Z., Gurvits L.I., Scott W.K., Taylor A.R., Edwards P.G., Hirabayashi H., 2000, ApJS, 131, 95

[44] Fomalont E.B., Petrov L., MacMillan D.S., Gordon D., Ma C., 2003, AJ, 126, 2562

[45] Gelderman R., Whittle M., 1994, ApJS, 91, 491

[46] Ghosh T., Salter C.J., 2002, ASPC, 278, 521

[47] Gilmore G., Shaw M.A., 1986, Nature, 321, 750

[48] Giovannini G., Feretti L., Gregorini L., Parma P., 1988, A&A, 199, 73

[49] Giovannini G., Feretti L., Venturi T., 1999, ASPC, 159, 439

[50] Giovannini G., Cotton W.D., Feretti L., Lara L., Venturi T., 2001, ApJ, 552, 508

[51] Gupta Neeraj, Srianand R., Saikia D.J., 2005, MNRAS, 361, 451

[52] Gupta Neeraj, Saikia D.J., 2006, MNRAS, 370, 738

[53] Heckman T.M., Balick B., van Breugel W.J.M., Miley G.K., 1983, AJ, 88, 583

[54] Holt J., Tadhunter C.N., Morganti R., 2003, MNRAS, 342, 227

[55] Hopkins P.F., Hernquist L., Cox T.J., Di Matteo T., Martini P., Robertson B., Springel V., 2005, ApJ, 630, 705

[56] Huchra J.P., Geller J.M., de Lapparent V., Corwin Jr., H.G., 1990, ApJS, 72, 433

[57] Jenkins C.J., Pooley G.G., Riley J.M., 1977, MmRAS, 84, 61

[58] Kandalian R.A., 1996, Astrophysics, 39, 237

[59] Kanekar N., Chengalur J.N., 2002, A&A, 381, L73

[60] Kapahi V.K., Saikia D.J., 1982, JA&A, 3, 465

[61] Kapahi V.K., Athreya R.M., van Breugel W., McCarthy P.J., Subrahmanya, C.R., 1998a, ApJS, 118, 275

[62] Kapahi V.K., Athreya R.M., Subrahmanya C.R., Baker J.C., Hunstead R.W., McCarthy P.J., van Breugel W., 1998b, ApJS, 118, 327

[63] Karachentsev I.D., 1980, ApJS, 44, 137

[64] Keel W.C., 1986, ApJ, 302, 296

[65] Labiano A., O'Dea C.P., Gelderman R., et al., 2005, A&A, 436, 493

[66] Large M.I., Mills B.Y., Little A.G., Crawford D.F., Sutton J.M., 1981, MNRAS, 194, 693

[67] Leon S., Lim J., Combes F., Dinh-v-Trung, 2003, ASPC, 290, 525

[68] Lim J., Leon S., Combes F., Dinh-V-Trung, 2000, ApJ, 545, 93L

[69] Lister M.L., Kellermann K.I., Vermeulen R.C., Cohen M.H., Zensus J.A., Ros E., 2003, ApJ, 584, 135

[70] Lüdke E., Garrington S.T., Spencer R.E., Akujor C.E., Muxlow T.W.B., Sanghera H.S., Fanti, C., 1998, MNRAS, 299, 467

[71] McCarthy P.J., Kapahi V.K., van Breugel W., Persson S.E., Athreya R.M., Subrahmanya C.R., 1996, ApJS, 107, 19

[72] Mirabel I.F., 1989, ApJ, 340, L13

[73] Mirabel I.F., 1990, ApJ, 352, 37

[74] Mirabel I.F., Sanders D.B., Każes I., 1989, ApJ, 340, L9

[75] Morganti R., Oosterloo T.A., et al., 2001, MNRAS, 323, 331

[76] Morganti R., Oosterloo T.A., Tadhunter C.N., Vermeulen R., Pihlström Y.M., van Moorsel G., Wills K.A., 2004, A&A, 424, 119

[77] Morganti R., Tadhunter C.N., Oosterloo T.A., 2005, A&A, 444, L9

[78] Murphy D.W., Browne I.W.A., Perley R.A., 1993, MNRAS, 264, 298

[79] Mutel R.L., Phillips R.B., Skuppin R., 1981, AJ, 86, 1600

[80] Neff S.G., Roberts L., Hutchings J.B., 1995, ApJS, 99, 349

[81] O'Dea C.P., 1998, PASP, 110, 493

[82] Ojha R. et al., 2004, AJ, 127, 3609

[83] Orr M.J.L., Browne I.W.A., 1982, MNRAS, 200, 1067

[84] Owsianik I., Conway J.E., Polatidis A.G., 1998, A&A, 336, L37

[85] Pearson T.J., Readhead A.C.S., 1988, ApJ, 328, 114

[86] Peck A.B., Taylor G.B., 1998, ApJ, 502,23

[87] Peck A.B., Taylor G.B., Conway J.E., 1999, ApJ, 521, 103

[88] Peck A.B., Taylor G.B., Fassnacht C.D., Readhead A.C.S., Vermeulen R.C., 2000, ApJ, 534, 104

[89] Perlman E.S., Carilli C.L., Stocke J.T., Conway J., 1996, AJ, 111, 1839

[90] Perlman E.S., Padovani P., Giommi P., Sambruna R., Jones L.R., Tzioumis A., Reynolds J., 1998, AJ, 115, 1253

[91] Petrov L., Kovalev Y.Y., Fomalont E., Gordon D., 2005, AJ, 129, 1163

[92] Phillips R.B., Mutel R.L., 1981, ApJ, 244, 19

[93] Pihlström Y.M., 2001, PhD Thesis, Chalmers University of Technology

[94] Pihlström Y.M., Conway J.E., Vermeulen R.C., 2003, A&A, 404, 871

[95] Polatidis A.G., Wilkinson P.N., Xu W., Readhead A.C.S., Pearson T.J., Taylor G.B., Vermeulen R.C., 1995, ApJS, 98, 1

[96] Rees M.J., 1984, ARA&A, 22, 471

[97] Reid R.I., Kronberg P.P., Perley R.A., 999, ApJS, 124, 285

[98] Rines K., Geller M.J., Kurtz M.J., Diaferio A., 2003, AJ, 126, 2152

[99] Röttgering H., Best P., Carilli C., Longair M., 1996, in Snellen I.A.G., Schilizzi R.T., Röttgering H.J.A., Bremer M.N., eds, The second workshop on gigahertz peaked spectrum and compact steep spectrum radio sources. Leiden Observatory, p. 48

[100] Rupen M.P., 1997, in The nature of elliptical galaxies, eds M. Arnoboldi, G.S. Da Costa, P. Saha, ASP Conf. Ser., 116, 322

[101] Saikia D.J., Gupta N., 2003, A&A, 405, 499

[102] Saikia D.J., Kulkarni A.R., 1998, MNRAS, 298, 45

[103] Saikia D.J., Jeyakumar S., Wiita P.J., Sanghera H.S., Spencer R.E., 1995, MNRAS, 276, 1215

[104] Saikia D.J., Jeyakumar S., Salter C.J., Thomasson P., Spencer R.E., Mantovani F., 2001, MNRAS, 321,37

[105] Saikia D.J., Thomasson P., Spencer R.E., Mantovani F., Salter C.J., Jeyakumar S., 2002, A&A, 391, 149

[106] Sanders D.B., Soifer B.T., Elias J.H., Neugebauer G., Matthews K., 1988, ApJ, 328, 35

[107] Sanghera H.S., Saikia D.J., Lüdke E., Spencer R.E., Foulsham P.A., Akujor C.E., Tzioumis A.K., 1995, A&A, 295, 629

[108] Schilizzi R.T. et al., 2000, AdSpR, 26, 709

[109] Scoville N.Z. et al., 2000, AJ, 119, 991

[110] Snellen I.A.G., Lehnert M.D., Bremer M.N., Schilizzi R.T., 2002, MNRAS, 337, 981

[111] Spencer R.E., McDowell J.C., Charlesworth M., Fanti C., 1989, MNRAS, 240, 657

[112] Spencer R.E. et al., 1991, MNRAS, 250, 225

[113] Spinrad H., Djorgovski S., Marr J., Aguilar L., 1985, PASP, 97, 932

[114] Stanghellini C., Baum S.A., O'Dea C.P., Morris G.B., 1990, A&A, 233, 379

[115] Stanghellini C., O'Dea C.P., Baum S.A., Laurikainen E., 1993, ApJS, 88, 1

[116] Stanghellini C., O'Dea C.P., Murphy D.W., 1999, A&AS, 134, 309

[117] Stanghellini C., Dallacasa D., O'Dea C.P., Baum S.A., Fanti R., Fanti C., 2001, A&A, 377, 377

[118] Strom R.G., Riley J.M., Spinrad H., van Breugel W.J.M., Djorgovski S., Liebert J., McCarthy P.J., 1990, A&A, 227, 19

[119] Taylor G.B., Vermeulen R.C., Pearson T.J., Readhead A.C.S., Henstock D.R., Browne I.W.A., Wilkinson P.N., 1994, ApJS, 95, 345

[120] Taylor G.B., Vermeulen R.C., 1997, ApJ, 485, L9

[121] Taylor G.B., Readhead A.C.S., Pearson T.J., 1996, ApJ, 463, 95

[122] Taylor G.B., Wrobel J.M., Vermuelen R.C., 1998, ApJ, 498, 619

[123] Taylor G.B., Marr J.M., Pearson T.J., Readhead A.C.S., 2000, ApJ, 541, 112

[124] Thomasson P., Saikia D.J., Muxlow T.W.B., 2003, MNRAS, 341, 91

[125] Tzioumis A. et al., 2002, A&A, 392, 841

[126] Ulvestad J.S., Johnston K.J., Weiler K.W., 1983, ApJ, 266, 18

[127] van Breugel W.J.M., Fanti C., Fanti R., Stanghellini C., Schilizzi R.T., Spencer R.E., 1992, A&A, 256, 56

[128] van Gorkom J.H., Knapp G.R., Ekers, R.D., Ekers, D.D., Laing, R.A., Polk, K.S., 1989, AJ, 97, 708

[129] van Ojik R., Röttgering H.J.A., Miley G.K., Hunstead R.W., 1997, A&A, 317, 358

[130] Veilleux S., Sanders D.B., Kim D.C., 1997, ApJ, 484, 92

[131] Venturi T., Morganti R., Tzioumis T., Reynolds J., 2000, A&A, 363, 84

[132] Verdoes Kleijn G.A., Baum S.A., dw Zeew P.T., O'Dea C.P., 1999, AJ, 118, 2592

[133] Vermeulen R.C. et al., 2003, A&A, 404, 861

[134] Wall J.V., Peacock J.A., 1985, MNRAS, 216, 173

[135] Walsh D.E.P., Knapp G.R., Wrobel J.M., Kim D.-W., 1989, ApJ, 337, 209

[136] Wegner G., Haynes M.P., Giovanelli R., 1993, AJ, 105, 1251

[137] Whyborn N.D., Browne I.W.A., Wilkinson P.N., Porcas R.W., Spinrad H., 1985, MNRAS, 214, 55

[138] Wilkinson P.N., Tzioumis A.K., Benson J.M., Walker R.C., Simon R.S., Kahn F.D., 1991, Nature, 352, 313

[139] Xiang L., Stanghellini C., Dallacasa D., Haiyan Z., 2002, A&A, 385, 768

[140] Xu W., Readhead A.C.S., Pearson T.J., Polatidis A.G., Wilkinson P.N., 1995, ApJS, 99, 297

[141] Zensus J.A., Ros E., Kellermann K.I., Cohen M.H., Vermeulen R.C., Kadler M., 2002, AJ, 124, 662

Chapter 3

Outflowing material in the CSS quasar 3C48: evidence of jet-cloud interaction?

3.1 Introduction

High-resolution radio images of Compact steep-spectrum sources (CSSs) show that there is a wide variety of structures, ranging from double-lobed and triple sources to those which are very complex and distorted (e.g. Phillips & Mutel 1982; Spencer et al. 1989; Fanti et al. 1990; Conway et al. 1994; Wilkinson et al. 1994; Sanghera et al. 1995; Dallacasa et al. 1995; Readhead et al. 1996a; Taylor et al. 1996; Snellen et al. 2000a; Stanghellini et al. 2001; Orienti et al. 2004). Although there is a consensus of opinion that most CSSs are young radio sources (Fanti et al. 1995; Readhead et al. 1996b; O'Dea 1998 for a review; Snellen et al. 2000b), a small fraction could be confined to small dimensions due to either a dense medium or interactions of the jet with dense clouds. Radio studies have shown that CSSs tend to be more asymmetric than the larger sources, possibly due to interaction with an asymmetric distribution of gas in the central regions (Saikia et al. 1995, 2001; Saikia & Gupta 2003). These authors speculated that this might be due to collisions with clouds of gas, some of which fuel the nuclear activity. Arshakian & Longair (2000) also concluded that intrinsic/environmental asymmetries are more important for sources of small physical sizes. Radio polarization studies often indicate large Faraday depths (e.g. Mantovani et al. 1994; Fanti et al. 2004), and also sometimes show evidence of asymmetrically-located clouds as a huge differential rotation measure between the oppositely directed lobes as in the CSS

quasar 3C147 (Junor et al. 1999), or high rotation measure where the jet bends sharply suggesting collision of the jet with a dense cloud as in 3C43 (Cotton et al. 2003). Optical studies of CSSs have also often shown evidence of interaction of the radio jets with the external medium (e.g. Gelderman & Whittle 1994; de Vries et al. 1999; Axon et al. 2000; O'Dea et al. 2002). The physical conditions under which a jet may be bent or distorted by such clouds, as well as the effects of an asymmetric gas distribution on opposite sides of the nucleus have been explored via analytical calculations as well as numerical simulations (Carvalho 1998; Higgins, O'Brien & Dunlop 1999; Wang, Wiita & Hooda 2000; Jeyakumar et al. 2005).

An interesting way of investigating interaction of the jet with the external clouds/medium could be via the absorption lines arising from the clouds accelerated by the jet. Baker et al. (2002) have studied the absorption spectra in a sample of quasars selected from the Molonglo Reference Catalogue, and find a slight excess of blue-shifted C IV absorption lines in CSSs compared with the larger objects. In a sample of high-redshift radio galaxies, van Ojik et al. (1997) reported a high incidence of H I absorption (9 out of 10) in the smaller objects (<50 kpc) compared with the larger ones (2 out of 8). Their study also showed an excess of blue-shifted Lyα absorption lines, and showed strong evidence of interaction of the radio source with the external environment. In the Section 2.4.6 we showed that the distribution of the velocity shifts of the principal (strongest) 21-cm absorption component does indicate that HI absorption for compact radio sources tends to be blue-shifted. Although blue-shifted absorption lines could arise due to either halo gas or circumnuclear gas kinematically affected by nuclear winds and/or radiation pressure, such studies suggest that jet-cloud interaction may also play a significant role in these objects.

To explore this theme, we have studied the well-known CSS quasar 3C48, which has a highly complex and distorted radio structure, speculated to be due to disruption of the jet by interaction with a cloud (e.g. Wilkinson et al. 1991; Worrall et al. 2004; Feng et al. 2005). We explore evidence of blue-shifted absorption line gas at radio and ultraviolet (UV) wavelengths using the Giant Metrewave Radio Telescope (GMRT) and archival data from the Hubble Space Telescope (HST) Space Telescope Imaging Spectrograph (STIS) and the Goddard High Resolution Spectrograph (GHRS), the Far Ultraviolet Spectroscopic Explorer (FUSE) and the International Ultraviolet Explorer (IUE). Physical properties of the blue-shifted absorber detected by us in the UV spectra and the possibility that absorbing material might be accelerated by interaction with the radio jet are discussed in this chapter.

3.2 3C48

3C48, the second quasar to be identified (Mathews & Sandage 1963), is an enigmatic CSS source. It has unusually strong IR emission (Neugebauer, Soifer & Miley 1985), comparable with most luminous IR galaxies. The detection of CO emission (Scoville et al. 1993; Wink, Guilloteau & Wilson 1997) at z=0.3695 implies the presence of about twice as much molecular gas as in ULIRGs. At radio wavelengths, the VLBI images resolve this highly compact radio source into a one-sided core-jet structure confined well within the optical host galaxy. Briggs (1995) and Feng et al. (2005) have reported the detection of a weak counter-jet on subarcsec scales. Wilkinson et al. (1991) interpret the complex structure of 3C48 as due to collision of the jet with a dense clump of gas in the host galaxy's interstellar medium. The radio jet is also aligned with the excess optical continuum, and [OII] λ3727 and [OIII] $\lambda\lambda$4959,5007 emission-line nebulosity seen close to the quasar core, and in particular the peak of continuum light at about 1 arcsec from the nucleus. This has been variously interpreted as the nucleus of a galaxy, merging with the host of 3C48 (Stockton & Ridgway 1991) or a star-forming region triggered by the radio jet (Chatzichristou et al. 1999).

The redshift of 3C48 as measured by several authors (Greenstein & Mathews 1963; Wampler et al. 1975; Thuan, Oke & Bergeron 1979) differ by about $\sim$500 km s^{-1}. In particular, Boroson & Oke (1982) noted that redshift of 3C48 as determined from the forbidden emission lines turns out to be slightly less than the value of 0.3700$\pm$0.0002 determined from the permitted emission lines. The discrepancy arose largely due to the lower spectral resolution data. In the higher resolution data of Chatzichristou et al. (1999), the forbidden lines are resolved into two components, one of which shows velocities similar to the permitted lines. The value of 0.3700 is also in agreement with the emission lines and stellar absorption lines seen from the fuzz around the source. The MgII emission line (Tytler et al. 1987) and CO emission (Scoville et al. 1993) have also been seen at redshifted frequencies corresponding to $\sim$0.370. Therefore, throughout this paper we use $z_{\rm em}$=0.3700 to represent the quasar redshift.

3.3 Observations and data analyses

We first describe the analyses of the UV data from HST STIS and GHRS, FUSE and IUE. These data have been obtained from the Multimission Archive at Space Telescope (MAST). We then describe the radio observations with the GMRT to detect redshifted H I in absorption towards 3C48.

Table 3.1: Observational log of UV data

Program ID	Instrument used	PI	Exposure time (s)	Wavelength coverage (Å)	Resolving power (R)	Signal-to-noise (per spectral resolution)
9280	HST STIS	A. Siemiginowska	8,113	2049−2139	11,000	7
8299	HST STIS	W. Jaffe	5,280	8540−9107	8,500	20
6707	HST GHRS	D. Bowen	21,760	1287−1575	2,000	15−25
Z002	FUSE	P. Wannier	8,347	985−1084	20,000	7[a]
KQ003	IUE	O'Brien	24,960	1150−1979	250	4

[a] The FUSE spectrum has been smoothed over 15 pixels.

3.3.1 UV data

The data from HST STIS and GHRS, FUSE and IUE instruments were reduced using the standard pipeline tasks `calstis, calhrs, calfuse and caliue` respectively. The pipeline processing keeps track of errors associated with each pixel at every stage of the reduction. The spectra corresponding to various exposures for each instrument along with the error spectra were then combined separately. The resulting signal-to-noise ratio applicable over most of the wavelength range and some of the basic details of the data sets used are summarised in Table 3.1. The spectra for each of the data sets were then continuum fitted using absorption free regions to get the final spectrum shown in Fig. 3.1.

The pipeline tasks also process the line lamp exposures to determine the zero point offset of wavelength and spatial scales in the image. We also made use of the Galactic absorption lines detected in each of the spectra to determine the zero point offsets. In particular, for the GHRS spectrum we find that it is required to shift the spectrum by approximately +0.8 Å. This is also consistent with the rms of approximately one diode (roughly 0.6 Å) in the default wavelength scale of GHRS pipeline calibration. The one diode rms in the wavelength scale arises due to the errors in the carrousel positioning and uncertainties caused due to the changing temperatures within the spectrograph and geomagnetically induced image motions (see *Instrument Handbook for the GHRS* for details). The spectrum corresponding to three GHRS exposures were combined after applying this offset.

3.3.2 Radio observations with GMRT

We observed 3C48 with GMRT to investigate redshifted 21-cm absorption with a bandwidth of 4 MHz in the 1060 MHz subband. The FX correlator system at GMRT splits the baseband bandwidth into 128 spectral channels, yielding a spectral resolution of 8.75

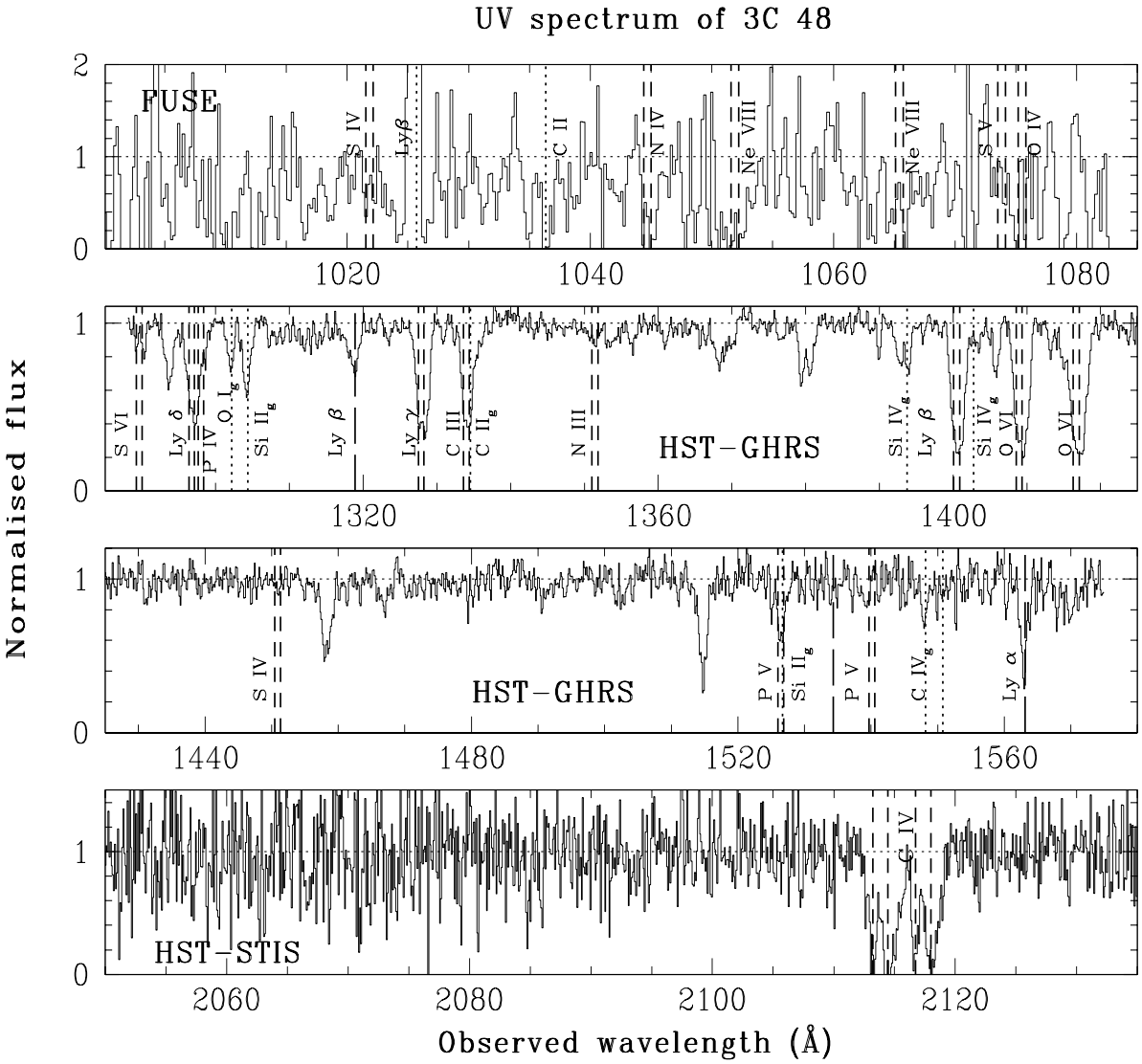

Figure 3.1: UV spectrum of the $z_{\rm em}$= 0.3700 quasar 3C48. Different absorption lines are labelled. Vertical dashed lines represent the positions of the absorption components associated with the $z_{\rm abs}$=0.3649 and 0.3658 systems. Short-dashed lines with the label 'g' correspond to Galactic absorption. Long dashed lines mark a possible intervening system, $z_{\rm abs}$=0.286. A number of unidentified absorption features (left unmarked) are also present in the spectrum. It is most likely that these are intervening Lyα absorption lines.

km $s^{-1}$for the chosen bandwidth. We observed 3C48 on a number of occasions with the redshifted 21-cm frequencies corresponding to $z_{\rm abs}$= 0.3654, the redshift at which we detect outflowing gas (Section 3.4) and 0.3695 and 0.3700, the emission-line redshifts from CO and optical observations respectively. This object was observed as part of our larger survey of H I absorption towards CSSs (Chapter 2), and the observational details have been described in Section 2.2.3. The radio data were reduced in the standard way using the Astronomical Image Processing System.

3.4 Observational results

3.4.1 UV spectra

We detect blue-shifted absorption lines with $z_{\rm abs}\simeq z_{\rm em}$in the UV spectra of 3C48. Fig. 3.1 shows the normalised UV spectrum obtained with HST and FUSE. Expected positions of absorption lines from our Galaxy, the associated system at $z_{\rm abs}$= 0.3654 and an intervening Lyα system at $z_{\rm abs}$= 0.286 are marked with short-dashed, dashed and long-dashed vertical lines respectively. In the case of the $z_{\rm abs}$= 0.3654 system we have marked the locations of the two velocity components identified from the C IV$\lambda\lambda$1548,1550 absorption lines seen in the STIS spectrum. It is clear from the figure that Lyβ, Lyγ, Lyδ, C IV, O VI and S VI absorption lines from the $z_{\rm abs}$= 0.3654 system are present in the HST-STIS and GHRS spectra. The C IIIλ977 absorption line is possibly blended with C IIλ1334 absorption from our Galaxy. We find Lyδ to be slightly stronger than the Lyγ line, which is possibly because of blending with the P IV absorption line.

Absorption lines of P V doublets and S IV are clearly absent. The available spectra do not cover the wavelength range where Lyα, N V and Si IV absorption lines are expected. The FUSE spectrum is noisier and we have examined the different exposures independently to verify the reliability of absorption lines. We have detected N IV and possibly O IV and Ne VIII . To our knowledge, Ne VIII absorption has been reported for 5 other systems, namely 3C288.1, UM 675, HS 1700+6416, J2233−606 and SBS 1542+531 (Petitjean, Riediger & Rauch 1996; Petitjean & Srianand 1999; Hamann et al. 1997; Telfer et al. 1998; Hamann, Netzer & Shields 2000). Based on the presence of absorption due to very highly ionized species and $z_{\rm abs}\simeq z_{\rm em}$it is most likely that the gas responsible for the absorption is located close to the nuclear region of 3C48.

The C IV$\lambda\lambda$1548,1550 absorption doublet detected in the STIS data is clearly resolved into two components at $z_{\rm abs}$=0.3649 and 0.3658 (Fig. 3.2). Voigt profile decomposition

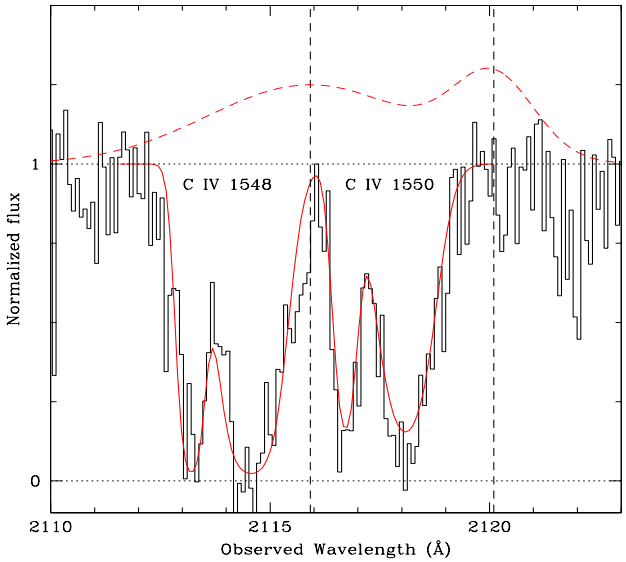

Figure 3.2: Profile of C IV$\lambda\lambda$1548,1550 absorption lines detected in the STIS spectrum of 3C48 (histogram) overplotted with the best-fitted Voigt profiles (smooth curves). Two well-detached absorption components are detected clearly at $z_{\rm abs}$= 0.3649 and 0.3658. Vertical long-dashed lines mark the expected location of C IVλ1548 emission based on the two velocity components detected in [OIII]$\lambda\lambda$4959,5007 and [OII]λ3727 emission lines (Chatzichristou et al. 1999). The figure also shows the expected velocity range of emitting gas (Gaussians with long-dashed lines) reconstructed using the parameters of Chatzichristou et al. (1999). The gas producing the C IV absorption is well detached from the nuclear line-emitting gas and has a velocity consistent with the blue component of the narrow line-emitting gas.

gives, N(C IV)=3.44$\pm$0.55$\times10^{14}$ cm^{-2} , b =39.8$\pm$4.3 km s^{-1}and N(C IV)=7.91$\pm$0.74$\times10^{14}$ cm^{-2}, b =92.6$\pm$5.9 km s^{-1}respectively for these components. Within the errors of the STIS spectrum, it cannot be ruled out that the C IV$\lambda\lambda$1548,1550 absorption lines are not saturated. Therefore, we take the column density estimates from the Voigt profile fits as a lower limit. In Fig. 3.2, alongwith the Voigt-profile fits to C IV absorption line, we show the location of C IVλ1548 emission as expected from the two components detected in the [OIII] $\lambda\lambda$4959,5007 and [OII] λ3727 emission lines (Chatzichristou et al. 1999). From the two-component profile decomposition of the emission-line spectrum integrated over the central 1.9 arcsec^2, Chatzichristou et al. (1999) find that one of the components (referred to as the red component) have redshift similar to the systemic redshift of the quasar while the other component (referred to as the blue component) is blue shifted by $\sim$580$\pm$15 km s^{-1}. The systemic red component is much narrower (FWHM $\sim$400 km s^{-1}) and shows a sys-

tematic trend in the velocity structure suggesting association with the rotational velocity field of the galaxy. The blue component on the other hand has much wider (FWHM $\sim$1010 km s^{-1}) line profile and shows no clear trend in the velocity field structure. From Fig. 3.2 it is clear that (i) the absorbing gas completely covers the background source and (ii) the velocity range spanned by the absorbing gas is consistent with that of the outflowing gas responsible for the blue-shifted [O III] $\lambda\lambda$4959,5007 and [O II] λ3727 emission detected by Chatzichristou et al. (1999).

In the lower-resolution GHRS data, the two absorption components detected in the STIS spectrum are unresolved. However the widths of the detected absorption lines are consistent with the presence of two components that are detected in the C IV profile. To keep the analysis simple, we do not try to get the column densities of individual components by fitting two components to the low dispersion data. Instead we estimate the total integrated column density in both the components.

For the absorption lines detected in the GHRS and FUSE data sets, we estimate column density at each velocity pixel using the relation

$$N(v) = 3.768 \times 10^{+14}\ \tau(v)/f\lambda\ \mathrm{cm}^{-2}\ \mathrm{km}^{-1}\mathrm{s} \tag{3.1}$$

where, τ, f and λ are the optical depth, oscillator strength and rest wavelength respectively. The latter two parameters have been taken from Verner et al. (1994). The total column density is obtained by integrating $N(v)$ over the velocity range over which absorption is detected (see Table 3.2). The typical 3σ errors are 25% of the estimates.

Although absorption is a direct indicator of the optical depth, in the case of partial coverage of the background source or when optical depth varies much more rapidly as a function of frequency than the spectral resolution, the depth of the absorption line provides only an under-estimate of the true column density. In case of poor spectral resolution, it is possible that the absorption in many cases may be actually optically thick. For example, for O VI$\lambda\lambda$1031,1037 doublet detected in the GHRS data, the column density estimates for the members of the doublet just scale by their respective oscillator strengths. This suggests that the O VI absorption lines are actually saturated. Therefore, we take the estimated value based on O VIλ1036 as a lower limit.

Similar to O VI , it is possible that neutral hydrogen column density estimated from Lyβ and Lyγ are at best the lower limits only. In the IUE spectrum, there is no apparent drop in the flux density at $\sim$1250 Å corresponding to the Lyman edge absorption at the redshift of the quasar ($z_{\rm em}$=0.3700) and the absorber ($z_{\rm abs}$=0.3654). By taking 20 Å on the blue side and 50 Å on the red side of the expected Lyman edge, we find N(H I)$\leq$3.06$\times$10^{16}

Table 3.2: Column density estimates for the various species.

Species	N (cm^{-2})	Instrument
Lyβ	2.57×10^{15}	HST-GHRS
Lyγ	5.50×10^{15}	"
Lyman-Limit	$\leq 3.06 \times 10^{16}$	IUE
C IV	$\geq 1.14\times10^{15}$	HST-STIS
S VI	8.62×10^{13}	HST-GHRS
O VI	$\geq 1.58 \times 10^{15}$	"
S IV	$\leq 9.32 \times 10^{13}$	"
P V	$\leq 2.91 \times 10^{13}$	"
N III	$\leq 1.30 \times 10^{14}$	"
N IV	5.15×10^{14}	FUSE
Ne VIII	5.45×10^{15}	"
S V	$\leq 4.01 \times 10^{13}$	"
O IV	3.86×10^{15}	"

cm^{-2}. This is consistent with the N(H I) values listed in Table 3.2 based on Lyβ and Lyγ . Thus the actual value of N(H I) is estimated to be between $\sim 5 \times 10^{15}$ cm^{-2} and 3×10^{16} cm^{-2}.

We evaluate the upper limits for column densities of the species that are not detected using the Lyγ absorption profile as the template (cf. Gupta et al. 2003 or see Chapter 6). The scaling factor $k = [Nf\lambda]_{X^+}/[Nf\lambda]_{template}$ between the two optical depths $\tau_{template}$ and τ_{X^i} for species X^i is then obtained by minimizing

$$\alpha = \Sigma(\tau_{\rm X^i} - k * \tau_{template})^2 \tag{3.2}$$

The upper limits calculated in this manner are tabulated in Table 3.2.

3.4.2 21-cm absorption

The column density of H I derived towards the optical point source is very low and the gas will not produce any detectable 21-cm absorption. A tentative detection of H I absorption (with a FWHM of 100 km s^{-1}) towards 3C48 was reported by Pihlström (2001). High-

resolution VLBI observations show that most of the radio emission is extended (Wilkinson et al. 1991; Worrall et al. 2004). Only 10% of the flux density at 1.53 GHz is in the collimated core-jet structure with only 1% of the flux density being associated with the radio core that is coincident with the optical point source. Thus the tentative detection of 21-cm absorption by Pihlström (2001), if true, has to be towards the extended radio emission.

Our deep GMRT observations fail to reveal any detectable 21-cm absorption at the systemic redshift of 3C48 as well as the gas responsible for UV absorption lines (Fig. 3.3). At the resolution of the GMRT observations, 3C48 is unresolved. Using the flux density of

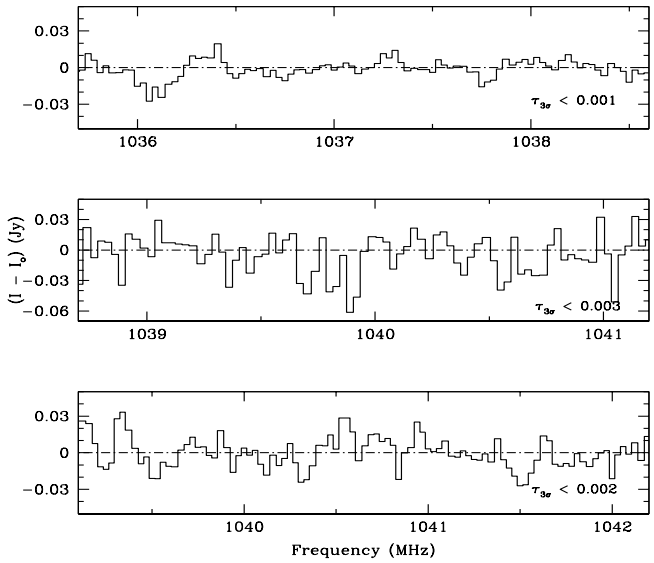

Figure 3.3: GMRT spectra covering the redshifted 21-cm frequency corresponding to $z_{\rm em}$=0.3700 from the optical emission lines, $z_{\rm em}$=0.3695 from the CO emission spectrum (upper panel), and $z_{\rm abs}$=0.3654 corresponding to the blue-shifted absorbing material reported here (middle and bottom panels).

20.3 Jy estimated from our observations, we obtain the 3σ upper limit on optical depth to be in the range of 0.001 to 0.003. We obtain an upper limit on average N(H I) across the radio source using the equation 2.1. Using the measured 3σ upper limit on τ (instead of τ_p) we get N(H I)$\lesssim$1.9$\times$10^{19}cm^{-2} for $\tau_{3\sigma}$ = 0.001 and assuming T$_s$=100 K and Δv=100 km s^{-1}. This is consistent with low N(H I) measured towards the optical point source. However, it should be noted that due to the extended nature of the radio source, low-resolution observations will fail to detect the presence of high N(H I) gas in front of say knot B (at about 0.3 kpc from the compact core A: see Worrall et al. 2004), near which the jet gets disrupted. Knot

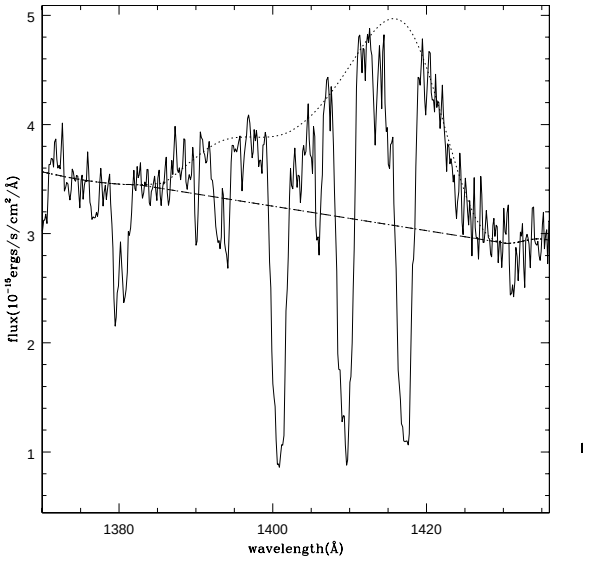

Figure 3.4: Portion of the HST GHRS spectrum showing Lyβ and O VI$\lambda\lambda$1031,1037 absorption lines detected on top of the O VI emission line. The low-order polynomial used to fit the continuum to the spectrum and model the emission line is shown as the dotted line. Dashed line represents the fit to the underlying continuum emission.

B has a 1.53 GHz flux density of 250 mJy that is $\sim$ 2% of the total flux density. This then implies that log N(H I) (cm^{-2}) $<$ 21.30 along our line of sight towards knot B. Thus our GMRT observations cannot rule out the presence of high column density H I towards individual knots or compact features.

3.5 Discussion

The UV spectra show clear evidence of blue-shifted gas with $z_{\rm abs}$=0.3654. Compared with $z_{\rm em}$=0.3700 this corresponds to a modest outflow velocity of $\sim$ 1000 km s^{-1}. We can further constrain the location of the outflowing material by comparing the absorption features with the emission lines. From Fig. 3.2, we can conclude that the members of the C IV$\lambda\lambda$1548,1550 doublet have optical depths consistent with a full coverage of the background source. As C IV , Lyβ and O VI absorption lines are detected on top of the emission lines (see Fig. 3.4) complete coverage means that the gas is outside the broad-line region (BLR) and has a projected size more than that of the BLR (see Srianand & Shankara-

narayanan 2000). We estimate the radius of BLR (R_{BLR}) using the empirical relation

$$R_{BLR} = 27.4\left(\frac{\lambda L_{5100}}{10^{44}\text{ergs s}^{-1}}\right)^{0.68} \text{lt days} \tag{3.3}$$

obtained by Corbett et al. (2003) using the reverberation mapping technique. The quasar rest frame luminosity at 5100 Å (i.e. $L_{5100\mathring{A}}$) is calculated using the observed flux density of F(8780 Å)=8.03×10^{-16} ergs s^{-1} $Å^{-1}$ cm^{-2}, estimated from the STIS data set (05AB1030, program ID 8299; see Table 3.1) and a spectral index of 1.0. Substituting the numerical value of $\lambda L_{5100\mathring{A}} = 3.28\times10^{45}$ ergs s^{-1} in equation (3.3), the radius of BLR is estimated to be 0.25 pc. Therefore we can conclude that size of the absorbing cloud should be larger than 0.5 pc and at least 0.25 pc away from the central engine.

In the following subsections we discuss the physical properties of the outflowing absorbing gas and explore the possibility that these might be affected by the interaction with the radio jet.

3.5.1 Physical conditions of the absorber

The observed column densities of different species can be used to obtain physical conditions of the absorbing gas. As $z_{\rm abs}\approx z_{\rm em}$for the outflowing material, it is most likely that the ionization state of the gas will be influenced by the radiation field of the quasar. In addition, jet-cloud interaction can also play an important role in determining the observed kinematics and ionization state of the gas in radio sources. First we consider the case of the absorbing gas in photoionization equilibrium with the UV radiation from 3C48. For this purpose, we run grids of photoionization models using CLOUDY (Ferland 1996; Ferland et al. 1998) considering the gas to be ionised by a Mathews & Ferland (1987; hereinafter referred to as the MF) spectrum and having Solar abundances. The neutral hydrogen column density used is log N(H I) = 16.0 cm^{-2}. We present the results of our calculations in Fig. 3.5 as a function of the dimensionless quantity, the ionization parameter U, which is defined as

$$\text{U} = \frac{Q(H^o)}{4\pi r^2 c n_H} \qquad \text{where} \qquad Q(H^o) = \int_{\nu_{LL}}^{\infty} \frac{L_\nu}{h\nu} d\nu \tag{3.4}$$

is the number of hydrogen ionizing photons per unit time, ν_{LL} is the frequency corresponding to the Lyman edge and r is the distance from the central source. In the right-hand panel of Fig. 3.5 we plot different column density ratios as a function of U. The vertical short dashed line in the right hand side of the figure marks the upper limit of U (i.e. log U≤ -1.18). Here we use the fact that N(H I)/N(H) cannot be less than 10^{-4}. The constraint on the total hydrogen column density, N(H), comes from the Chandra observations of Worrall et al.

(2004). They find no evidence for any intrinsic absorption in excess of 5×10^{19} cm^{-2} in the direction of 3C48. A conservative lower limit of log U=−1.82 is obtained from the column density ratios N(N IV)/N(N III) and N(S VI)/N(S IV). From Fig. 3.5, it is apparent that the ratio N(C IV)/N(N IV) is independent of U when log U≤ -1.0. As the gas is optically thin our choice of N(H I) and Solar abundance ratios, $Z_\odot$ will not alter these constraints. The observed ratio of N(C IV)/N(N IV) is ∼0.1 dex below the predictions of our model. This is within the measurement uncertainties of our data. Therefore, within the measurement uncertainties, [N/C] is very close to Solar values. This is in contrast with the systematically higher supersolar [N/C] ratios observed in most of the QSOs, especially the ones at high redshift or having high luminosities (Hamann & Ferland 1992, 1993, 1999; Petitjean & Srianand 1999). The rapid star-formation models enhancing the nitrogen abundance by the secondary CNO nucleosynthesis have been used to explain the [N/C]>$[N/C]_\odot$ ratios in these high redshift/luminosity systems. Using the observed flux density, F(1246.7Å)=3.13×10^{-15} erg s^{-1} cm^{-2} Å^{-1} from the IUE data, a luminosity distance of 1950.7 Mpc and a spectral index of α=0.5, we estimate the luminosity, νL_ν, at 1450 Å for 3C48 to be 3.5×10^{11} $L_\odot$. From Fig. 7 of Hamann et al. (1999), it can be seen that Solar values of [N/C] are not unusual for 3C48 with $z_{\rm em}$=0.3700 and above estimated luminosity at 1450 Å. In the right panel of Fig. 3.5, we plot the predicted values of column densities of various species as a function of U. Horizontal lines mark the observed values. Clearly, observed column densities of C IV and S VI are lower by ∼0.5 dex compared to the model predictions within the allowed range of ionization parameter. As the absorbing gas is optically thin, this difference can be accounted for by lowering either the value of N(H I) or the metallicity. The allowed range of N(H I) listed in Table 3.2, constrains the metallicity of the absorbing gas to be in range $0.1\leq Z/Z_\odot\leq1.3$.

The column density of Ne VIII as predicted by the photoionization models is more than two orders of magnitude lower than the Ne VIII column density estimated from the possible detection of this line. Reconciliation of the observed Ne VIII value requires neon abundance enhancement or postulating regions with different levels of ionisation (multiply-ionized regions). Since the rest of the observed species can be explained by Solar abundance ratios it seems unlikely that only Ne has an unusual abundance. Thus the possible detection of Ne VIII in the poor signal-to-noise ratio FUSE data can be understood by the existence of multiply-ionized regions. Such multiply-ionized regions have been used to explain the observed column densities of highly ionised species (including Ne VIII) in J2233−606, UM675 and 3C288.1 (Petitjean & Srianand 1999; Hamann et al. 1997; Hamann et al.

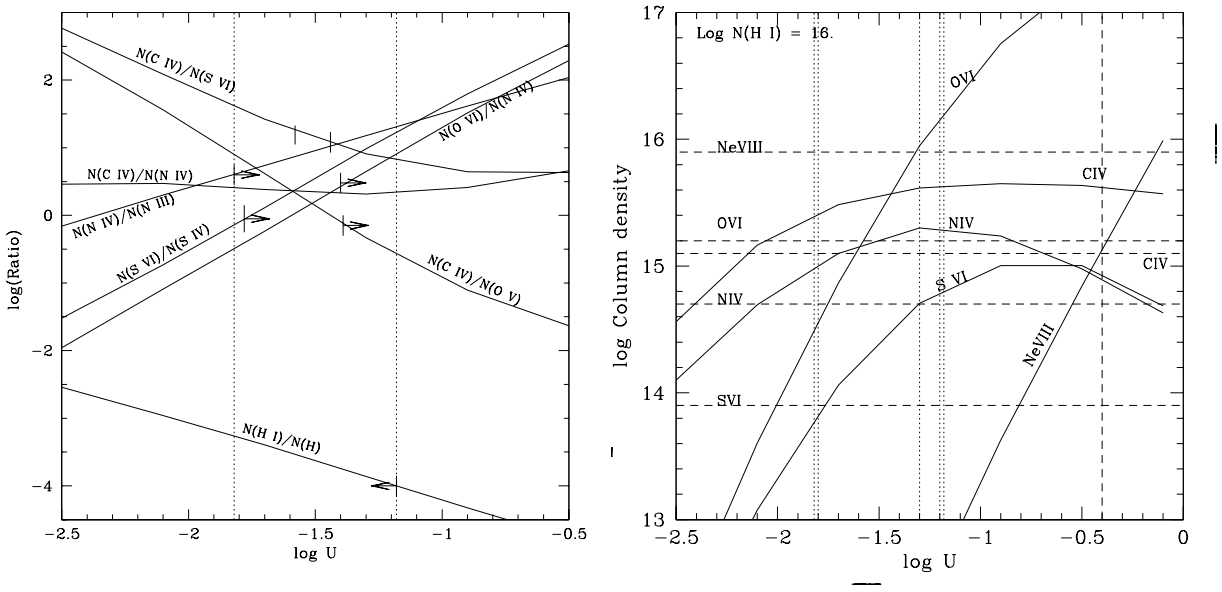

Figure 3.5: Results of model calculations with N(H I) = 10^{16} cm^{-2}, QSO spectrum given by MF and Z = Z$_\odot$. Left panel shows different ion ratios predicted in the calculations as a function of ionization parameter. The arrows indicate the limits on U from the observed values. The vertical dashed lines mark the possible range in U that will be consistent with the observations. Right panel shows the predicted column density as a function of U for a few ions. The horizontal lines mark the measured values or upper limits to the column densities (see Table. 3.2). Apart from N(Ne VIII) all the observed column densities and the limits are consistent with $-1.82 \leq \log U \leq -1.18$ and Z = 0.5 Z$_\odot$ for log N(H I) = 16 cm^{-2}.

2000). Thus it is possible that the low-ionization species originate from the high-density (low-ionization) phase and high-ionization species Ne VIII originate from the low-density (high-ionization) phase of the absorption-line system. Our data does show some evidence that the absorption-line system consists of a number of components. However, due to low spectral resolution and poor signal-to-noise ratio it is difficult to say if Ne VIII arises from the same component as the other low-ionization species. The density of the absorbing gas or its distance from the quasar nucleus can, in principle, be constrained using equation (3.4) if either of these two quantities and $Q(H^o)$ are known. We estimate the luminosity at the Lyman limit, $L_{LL} = 5.4 \times 10^{29}$ erg s^{-1} Hz^{-1} in the quasar rest frame using the observed flux density, F(1246.7Å)=3.13×10^{-15} erg s^{-1} cm^{-2} Å^{-1} from the IUE data, a luminosity distance of 1950.7 Mpc and a spectral index of α=0.5. This translates into Q(H^o)=1.3×10^{56}

photons s^{-1}. Substituting numerical values in equation (3.4) then gives

$$U = \frac{3.4 \times 10^{44}}{nr^2}. \quad (3.5)$$

Taking a nominal value of log U=−1.5 from the photoionization models, $nr_{pc}^2 = 1.2\times10^9$ cm^{-3} pc^2, where r_{pc} is the distance from the central source in parsecs. However, with the available information, it is not possible to get useful estimates of these parameters. Assuming that the absorbing cloud was pushed outwards by the radio jet $\gtrsim 10^5$ yr ago (cf. Section 3.5.2), it would have travelled $\gtrsim$100 pc with a velocity of $\sim$ 1000 km s^{-1}. This implies that the number density $n \lesssim 10^5$ cm^{-3}.

3.5.2 Jet-cloud interaction?

The complex radio structure of 3C48 has led to suggestions that the jet in 3C48 may be disrupted by strong interaction with the external medium (e.g. Wilkinson et al. 1991; Feng et al. 2005). This is not surprising as CSSs tend to be more asymmetric in both the separation ratio (r_D), defined to be the ratio of the separation from the core/nucleus of the farther component to the nearer one, and the flux density ratio (r_L), defined to be the ratio of integrated flux densities of the farther to the nearer component, compared with the larger sources, suggesting interaction with an asymmetric distribution of gas in the central regions (Saikia et al. 1995, 2001). The component nearer to the nucleus often tends to be the brighter one, which is possibly a signature of the expansion of nearer component through the denser environment leading to higher dissipation of energy. Orientation effects can also lead to substantial enhancements in these observed asymmetry parameters (cf. Jeyakumar et al. 2005 and references therein). Using the images and core position as given by Feng et al. (2005), who have recently reported the detection of a counter-jet in 3C48, the separation ratio for the prominent northern peak N2 and the counter-jet S is ≈2.8. This could increase to ≈5 if the region of enhanced intensity in the outer region is taken instead of N2. The flux density ratio (r_L) of the northern or approaching components to the southern one, S, lies between ∼200 and 400 for observations at different frequencies and with different resolutions (Feng et al. 2005). The source also appears significantly misaligned, possibly due to collision with clouds of gas and also exhibits jitters in the direction of the ejection axis as seen in the VLBA 8-GHz image of Worrall et al. (2004). The misalignment angle, defined to be the supplement of the angle formed at the core by N2 and S is about 30°. For an inclination angle of 30−35° for the jet, estimated from the relative strength of the core, and an intrinsic misalignment of ∼10−15°, r_D is in the range of ∼3.8 to 5 for a velocity

of advancement of ∼0.5c. The corresponding flux density ratio, $r_L = r_D^{2+\alpha}$ (e.g. Scheuer & Readhead 1979; Blandford & Königl 1979) is in the range of ∼50−100 for a spectral index of 0.9, which is lower than the observed flux density ratio by at least a factor of ∼3. This difference could be attributed to intrinsic asymmetries in the gas distribution (cf. McCarthy, van Breugel & Kapahi 1991). Using the formalism of Eilek & Shore (1989) and Gopal-Krishna & Wiita (1991), we estimate the density ratio on opposite sides to be ∼7. However, these numbers should be treated with caution because of the complex structure of the source and uncertainties in some of the basic parameters such as the velocity of advancement.

The detection of blue-shifted absorption lines caused by clouds of gas in the path of the radio jet would be an indication of jet-cloud interaction. Chatzichristou et al. (1999) report the detection of blue-shifted emission line ([OIII] λλ4959,5007 and [OII] λ3727) gas in 3C48 over 1.9 arcsec^2 of the central region. On the basis of the velocity structure of the blue-shifted component of the emission line gas and its increasing strength in the same direction as the radio jet, they suggest that this gas contains the imprint of interaction with the jet. The kinematical properties of this blue-shifted emission line gas, which shows clumpy morphology and has an outflow velocity of ∼580 km s^{-1}, are similar to the one detected in absorption. Using the mass estimate of $\sim 10^9 M_\odot$ (Fabian et al. 1987) for the emission line gas, determined from the strength of [OIII] λ5007 in 3C48, Wilkinson et al. (1991) show that energetics of the radio jet are capable of driving this gas with velocities as high as ≈1000 km s^{-1}. This is similar to the outflowing velocity of ∼1000 km s^{-1}for the blue-shifted material seen in absorption. Although blue-shifted absorption can be caused by other physical processes like radiative acceleration, the kinematical similarities with the emission-line gas and the situation in 3C48 make jet-cloud interaction a likely possibility.

The interaction with the jet can impart momentum to the gas and can also heat as well as ionize it. The gas ploughed and compressed by the jet can heat up to postshock temperatures of $\sim 10^8$K (de Vries et al. 1999). Taking adiabatic and radiative cooling into account de Vries et al. find that such a gas with a density of 1−5 cm^{-3} will cool to 10^4K in about 30,000 yr. Using the recombination coefficients from Péquignot, Petitjean & Boisson (1991), we find that the recombination timescales for gas with a temperature few times 10^4K and density 5 cm^{-3} are only a few thousand years for most of the species considered here. The maximum recombination timescale occurs for H I and O I, which we estimate to be $\sim 10^4$ yr. Therefore, any thermal or ionization signature of jet−cloud interaction will be lost in timescales $\gtrsim 10^5$ yr. Since we can explain the observed column densities of the

absorbing cloud using the photoionization models alone, any injection of energy resulting from a jet-cloud interaction must have taken place before 10^5 yr.

3.6 Summary

Detection of a $z_{\rm abs}$=0.3654 absorption-line system in the UV spectrum of the CSS quasar 3C48, which has a highly distorted radio structure, have been presented in this chapter. The absorbing material is blueshifted by ∼1000 km s^{-1}with respect to $z_{\rm em}$=0.3700 estimated from the optical emission lines. The outflowing material shows absorption lines from Lyβ, Lyγ, C IV, S VI, O VI, N IV and possibly O IV and Ne VIII. Detection of high-ionization lines such as O VI and Ne VIII suggests that the outflowing material is located close to the nucleus of the quasar. The kinematical properties of the $z_{\rm abs}$=0.3654 system are very similar to the blue-shifted emission line gas detected by Chatzichristou et al. (1999). The complex radio structure has been interpreted to be due to strong interaction with the ambient medium. On the basis of spatial correlation between the radio source and emission line gas, Chatzichristou et al. argue that this component bears the imprint of the interaction between the jet and the ambient gas. Considering the similarity of the kinematics of the emitting and absorbing material and the physical situation in 3C48, it is possible that the outflowing material detected in absorption may have also interacted with the radio jet.

Interaction of a cloud with a radio jet can impart momentum and as well as heat and ionize it. The recombination and cooling timescales suggest that signatures of such a jet-cloud interaction will be lost on time scales $\gtrsim 10^5$ yr. We find that photoionization models with Solar abundance ratios (with overall metallicity in the range $0.1 \leq {\rm Z/Z_\odot} \leq 1.3$) are enough to explain the observed column densities of all the species except for Ne VIII . The consistency with the photoionization-models suggests that the any possible interaction of absorbing material with the jet must have taken place $\gtrsim 10^5$ yr ago. Reconciliation of the possible Ne VIII detection requires regions with different levels of ionization. We also find that the abundance ratio of nitrogen to carbon is close to Solar values, unlike in the case of most quasars, especially at high-redshifts, which have super-Solar values.

Our GMRT spectra of 3C48, from which we estimate the 3σ upper limit to the optical depth to lie in the range 0.001 to 0.003, is consistent with the low N(H I) detected towards the optical point source. Assuming a spin temperature of 100 K and line width of 100 km s^{-1}, these correspond to column densities of N(H I)$\leq$(1.8−5.4) $\times$ 10^{19} cm^{-2}. Due to the diffuse nature of the radio structure of 3C48, H I column densities as high as 10^{21} cm^{-2} towards individual knots or compact features cannot be ruled out.

Bibliography

[1] Arshakian T.G., Longair M.S., 2000, MNRAS, 311, 846

[2] Axon D.J., Capetti A., Fanti R., Morganti R., Robinson A., Spencer R., 2000, AJ, 120, 2284

[3] Baker J.C., Hunstead R.W., Athreya R.M., Barthel P.D., de Silva E., Lehnert M.D., Saunders R.D.E., 2002, ApJ, 568, 592

[4] Blandford R.D., Königl A., 1979, ApJ, 232, 34

[5] Boroson T.A., Oke J.B., 1982, Nature, 296, 397

[6] Briggs D.S., 1995, AAS, 18711202B

[7] Carvalho J.C., 1998, A&A, 329, 845

[8] Chatzichristou E.T., Vanderriest C., Jaffe W., 1999, A&A, 343, 407

[9] Conway J.E., Myers S.T., Pearson T.J., Readhead A.C.S., Unwin S.C., Xu W., 1994, ApJ, 425, 568

[10] Corbett E.A. et al., 2003, MNRAS, 343, 705

[11] Cotton W.D., Spencer R.E., Saikia D.J., Garrington S., 2003, A&A, 403, 537

[12] Dallacasa D., Fanti C., Fanti R., Schilizzi R.T., Spencer R.E., 1995, A&A, 295, 27

[13] de Vries W.H., O'Dea C.P., Baum S.A., Barthel P.D., 1999, ApJ, 526, 27

[14] Eilek J.A., Shore S.N., 1989, ApJ, 342, 187

[15] Fabian A.C., Crawford C.S., Johnstone R.M., Thomas P.A., 1987, MNRAS, 228, 963

[16] Fanti R., Fanti C., Schilizzi R.T., Spencer R.E., Nan Rendong, Parma P., van Breugel W.J.M., Venturi T., 1990, A&A, 231, 333

[17] Fanti C., Fanti R., Dallacasa D., Schilizzi R.T., Spencer R.E., Stanghellini C. 1995, A&A, 302, 317

[18] Fanti C. et al., 2004, A&A, 427, 465

[19] Feng W.X., An T., Hong X.Y., Zhao Jun-Hui, Venturi T., Shen Z.Q., Wang W.H., 2005, A&A, 434, 101

[20] Ferland G.J., 1996, HAZY- a brief introduction to CLOUDY 90, University of Kentucky Physics Department Internal Report

[21] Ferland G.J., Korista K.T., Verner D.A., Ferguson J.W., Kingdon J.B., Verner E.M., 1998, PASP, 110, 761

[22] Gelderman R., Whittle M., 1994, ApJS, 91, 491

[23] Gopal-Krishna, Wiita P.J., 1991, ApJ, 373, 325

[24] Greenstein J.L., Mathews T.A., 1963, Nature, 197, 1041

[25] Gupta N., Srianand R., Petitjean P., Ledoux C., 2003, A&A, 406, 65

[26] Hamann F., Ferland G.J., 1992, ApJ, 391, 53

[27] Hamann F., Ferland G.J., 1993, ApJ, 418, 11

[28] Hamann F., Ferland G.J., 1999, ARA&A, 37,487

[29] Hamann F., Barlow T.A., Junkkarinen V., Burbidge E.M., 1997, ApJ, 478, 80

[30] Hamann F.W., Netzer H., Shields J. C., 2000, ApJ, 536, 101

[31] Higgins S.W., O'Brien T.J., Dunlop J.S., 1999, MNRAS, 309, 273

[32] Jeyakumar S., Wiita P.J., Saikia D. J., Hooda J.S., 2005, A&A, 432, 823

[33] Junor W., Salter C.J., Saikia D. J., Mantovani F., Peck A. B, 1999, MNRAS, 308, 955

[34] Mantovani F., Junor W., Fanti R., Padrielli L., Saikia D.J., 1994, A&A, 292, 59

[35] Mathews W.G., Ferland G.J., ApJ, 1987, 323, 456

[36] Mathews T.A., Sandage A.R., ApJ, 1963, 138, 30

[37] McCarthy P.J., van Breugel W., Kapahi V.K., 1991, ApJ, 371, 478

[38] Neugebauer G., Soifer B.T., Miley G. K., 1985, ApJ, 295, L27

[39] O'Dea C.P. 1998, PASP, 110, 493

[40] O'Dea C.P. et al., 2002, AJ, 123, 2333

[41] Orienti M., Dallacasa D., Fanti C., Fanti R., Tinti S., Stanghellini C., 2004, A&A, 426, 463

[42] Péquignot D., Petitjean P., Boisson C., 1991, A&A, 251, 680

[43] Petitjean P., Riediger R., Rauch, M., 1996, A&A ,307, 417

[44] Petitjean P., Srianand R., 1999, A&A, 345, 73

[45] Phillips R.B., Mutel R.L., 1982, A&A, 106, 21

[46] Pihlström, Y.M., 2001, PhD Thesis, Chalmers University of Technology

[47] Readhead A.C.S., Taylor G.B., Xu W., Pearson T.J., Wilkinson P.N., Polatidis A.G., 1996a, ApJ, 460, 612

[48] Readhead A.C.S., Taylor G.B., Pearson T.J., Wilkinson P.N., 1996b, ApJ, 460, 634

[49] Saikia D.J., Jeyakumar S., Wiita P.J., Sanghera H.S., Spencer R.E., 1995, MNRAS, 276, 1215

[50] Saikia D.J., Jeyakumar S., Salter C.J., Thomasson P., Spencer R.E., Mantovani F., 2001, MNRAS, 321,37

[51] Saikia D.J., Gupta N., 2003, A&A, 405, 499

[52] Sanghera H.S., Saikia D.J., Lüdke E., Spencer R.E., Foulsham P.A., Akujor C.E., Tzioumis A.K., 1995, A&A, 295, 629

[53] Scheuer P.A.G., Readhead A.C.S., 1979, Nature, 277, 182

[54] Scoville N.Z., Padin S., Sanders D.B., Soifer B.T., Yun M.S., 1993, ApJ, 415, L75

[55] Snellen I.A.G., Schilizzi R.T., van Langevelde H.J., 2000a, MNRAS, 319, 429

[56] Snellen I.A.G., Schilizzi R.T., Miley G.K., de Bruyn A.G., Bremer M.N., Röttgering H.J.A., 2000b, MNRAS, 319, 445

[57] Spencer R.E., McDowell J.C., Charlesworth M., Fanti C., Parma P., Peacock J.A., 1989, MNRAS, 240, 657

[58] Srianand R., Shankaranarayanan S., 1999, ApJ, 518, 672

[59] Stanghellini C., Dallacasa D., O'Dea C.P., Baum S.A., Fanti R., Fanti C., 2001, A&A, 379, 870

[60] Stockton A., Ridgway S.E., 1991, AJ, 102, 488

[61] Taylor G.B., Readhead A.C.S., Pearson T.J., 1996, ApJ, 463, 95

[62] Telfer R.C., Kriss G.A., Zheng W., Davidsen A.F., Green R.F., 1998, ApJ, 509, 132

[63] Thuan T.X., Oke J.B., Bergeron J., 1979, 230, 340

[64] Tytler D., Boksenberg A., Sargent W.L.W., Young P., Kunth D., 1987, ApJS, 64, 667

[65] van Ojik R., Roettgering H.J.A., Miley G.K., Hunstead R.W., 1997, A&A, 317, 358

[66] Verner D.A., Barthel P.D., Tytler D., 1994, A&AS, 108, 287

[67] Wampler E.J., Robinson L.B., Burbidge E.M., Baldwin J.A., 1975, ApJL, 198, L49

[68] Wang Z., Wiita P.J., Hooda J.S., 2000, ApJ, 534, 201

[69] Wilkinson P.N., Tzioumis A.K., Benson J.M., Walker R.C., Simon R.S., Kahn F.D., 1991, Nature, 352, 313

[70] Wilkinson P.N., Polatidis A.G., Readhead A.C.S., Xu W., Pearson T.J., 1994, ApJ, 432, L87

[71] Wink J.E., Guilloteau S., Wilson T.L., 1997, A&A, 322, 427

[72] Worrall D.M., Hardcastle M.J., Peasrson T.J., Readhead A.C.S., 2004, MNRAS, 347, 632

Chapter 4

Unification scheme and the distribution of neutral gas in compact radio sources

4.1 Introduction

An understanding of the distribution and kinematics of the different components of the circumnuclear gas in an active galactic nucleus (AGN) is important both for studying the anisotropy in the radiation field and thereby testing the unification scheme (cf. Barthel 1989; Urry & Padovani 1995), and for understanding the fuelling of the radio activity. An important way of probing the atomic gas on sub-galactic scales is by studying 21-cm HI absorption towards the compact components of CSS and GPS objects, or the compact radio nuclei of the larger objects (e.g. van Gorkom et al. 1989; Conway & Blanco 1995; Peck et al. 2000; Pihlström 2001; Vermeulen et al. 2003; Pihlström et al. 2003; Gupta et al. 2006). The HI absorption lines associated with CSS and GPS objects exhibit a variety of line profiles, suggesting significant, sometimes complex, gas motions, while the HI column densities have been found to be anti-correlated with source sizes (Chapter 2; Gupta et al. 2006). Pihlström et al. (2003) have explored different distributions of the HI gas density to explain this observed anti-correlation, and find that a disk as well as a spherical distribution are consistent with it. To study some of these aspects and to test for consistency with the unification scheme, we examine the dependence of HI column density on relative prominence of the core, f_c, which is being used as a statistical measure of the orientation of the source axis to the line of sight (Orr & Browne 1982; Kapahi & Saikia 1982). In this chapter, we

Table 4.1: Sample of CSS and GPS sources.

Source name	Alt. name	Opt. ID	Redshift	P_{5GHz} $\times 10^{25}$ (W/Hz)	LLS (kpc)	f_c	Str. class	R_θ	Δ (°)	Ref.	Radio class	N(HI) $\times 10^{20}$ (cm^{-2})	V_{shift} (km/s)	Ref.
(1)	(2)	(3)	(4)	(5)	(6)	(7)	(8)	(9)	(10)	(11)	(12)	(13)	(14)	(15)
J0025−2602	OB-238	G	0.322	112	3.02	<0.002	D			1	CSS	2.42	−30	V
J0111+3906	OC314	G	0.669	99.6	0.04	<0.004	T	1.28	9.7	2,3 4,5	GPS	84.2	0	C
J0119+3210	4C31.04	G	0.060	1.30	0.09	0.012	T	1.14	7.0	6	CSS	12.2	−10	Gu
J0137+3309	3C48	Q	0.3700	245	6.12	0.012	T	5.0	35	7,8	CSS	<0.06		Gu
J0141+1353	3C49	G	0.621	134.0	6.71	0.007	T	2.31	21	9,10	CSS	1.17	−185	V
J0224+2750	3C67	G	0.310	25.8	11.3	0.012	T	2.56	0.5	10,11	CSS	<1.45		V
J0251+4315	S4	Q	1.311	449	0.11	0.008	T	1.38	13	12	CSS	<2.61		Gu
J0410+7656	4C76.03	G	0.599	337	0.93	0.018	T	1.35	12	10,13	CSS	2.66	315	V
J0431+2037	OF247	G	0.219	32.8	1.02	0.096	T	4.69	4.5	13,14	GPS	3.66	318	V
J0503+0203	OG003	Q	0.585	196	0.07	0.028	T	1.39	24	15	GPS	6.69	43	C
J0521+1638	3C138	Q	0.759	78.6	4.98	0.132	T	1.70	0.0	9,10 16	CSS	<0.48		V
J0741+3112	OI363	Q	0.635	238	0.04	0.279	T	1.26	2.9	15,17	GPS	<0.99		V
J0954+7435		G	0.695	462	0.15	<0.002	D			18,19	GPS	<2.51		V
J1035+5628	OL553	G	0.459	72.0	0.02	<0.002	D			20	GPS	<1.38		V
J1120+1420	4C14.41	G	0.362	37.7	0.42	0.017	T	1.28	15	21	GPS	<0.61		V
J1124+1919	3C258	G	0.165	3.0	0.28	<0.012	D			11,22	CSS	5.05	163	Gu
J1206+6413	3C268.3	G	0.371	55.0	6.56	0.001	T	2.96	16	23,10	CSS	2.07	258	V
J1252+5634	3C277.1	Q	0.321	26.8	7.74	0.068	T	2.53	0.0	23,10	CSS	<0.72		V
J1308−0950	OP-010	G	0.464	166	3.47	<0.010	D			1	CSS	<1.35		V
J1313+5458		Q	0.613	72.0	0.25	<0.004	D			18	GPS	<1.80		V
J1326+3154	4C32.44	G	0.370	88.7	0.29	<0.005	D			24,25	GPS	0.75	−471	V
J1443+7707	3C303.1	G	0.267	10.1	7.32	<0.001	D			23	CSS	<1.50		V
J1521+0430	4C04.51	Q	1.296	1208	1.15	<0.002	D			27	GPS	<0.64		Gu
J1816+3457		G	0.245	5.60	0.15	<0.004	D			19	CSS	5.31	−184	P1
J1819−6345	MRC	G	0.0645	4.2	0.41	0.131	T	2.10	21	1,28	CSS	21.2	−160	M
J1821+3942	4C39.56	G	0.798	319	3.88	0.098	T	2.75	5.5	13,14	CSS	1.75	−806	V
J1944+5448	OV573	G	0.263	17.3	0.16	0.033	T	1.81	5.0	14,29	GPS	5.21	−1420	V
J1945+7055		G	0.101	1.54	0.06	0.050	T	1.04	0.0	30	GPS	35.5	−172	P2
J2137−2042	OX-258	G	0.635	223	1.37	<0.004	D			1,31	CSS	<1.18		V
J2325+4346	OZ438	G	0.145	4.70	4.00	<0.010	D			11	CSS	<0.84		Gu
J2344+8226		Q	0.735	292	1.94	0.134	T	1.39	11	13,14	GPS	<0.75		V
J2355+4950	OZ488	G	0.238	22.3	0.26	0.011	T	1.03	7.0	32,33	GPS	3.01	−12	V

The columns are as follows: Cols. 1 and 2: source name and an alternative name; cols. 3 and 4: optical identification and redshift; col. 5: radio luminosity at 5 GHz; col. 6: the largest linear size (LLS) defined to be the separation between the outermost peaks of radio emission; col. 7: the fraction of emission from the core, f_c, at an emitted frequency of 8 GHz; col. 8: structural classification where D denotes a double source while T implies a triple source which has a detected core; col. 9: the separation ratio, R_θ, defined to be the ratio of the separation of the further component from the core to the nearer one; col. 10: the misalignment angle, Δ, defined to be the supplement of the angle formed at the core by the outer hotspots; col. 11: references for the radio structure; col. 12: radio identification of the sources as CSS and GPS objects; col. 13: HI column density or a 3σ upper limit to it estimated assuming a spin temperature of 100 K and full coverage of the background source by the absorber; col. 14: the shift of the primary HI component relative to the systemic velocity as measured from the optical emission lines, with a negative sign indicating a blue-shift, and col. 15: references for the HI observations.

References for structural information: 1: Tzioumis et al. (2002); 2: Pearson & Readhead (1988); 3: Owsianik et al. (1998); 4: Zensus et al. (2002); 5: Baum et al. (1990); 6: Giovannini et al. (2001); 7: Feng et al. (2005); 8: Gupta et al. (2005); 9: Fanti et al. (1989); 10: Saikia et al. (1995); 11: Sanghera et al. (1995); 12: Fey & Charlot (2000); 13: Dallacasa et al. (1995); 14: Saikia et al. (2001); 15: Stanghellini et al. (2001); 16: Akujor et al. (1991); 17: Saikia et al. (1998); 18: Taylor et al. (1994); 19: Peck & Taylor (2000); 20: Fomalont et al. (2000); 21: Bondi et al. (1998); 22: Strom et al. (1990); 23: Lüdke et al. (1998); 24: Mutel et al. (1981); 25: Fey et al. (1996); 26: Perlman et al. (1996); 27: Xiang et al. (2002); 28: Ojha et al. (2004); 29: Xu et al. (1995); 30: Taylor & Vermeulen (1997); 31: Fomalont et al. (2003); 32: Polatidis et al. (1995); 33: Taylor et al. (2000).

References for HI observations: V: Vermeulen et al. (2003); C: Carilli et al. (1998); Gu: Gupta et al. (2006); P1: Peck et al. (2000); M: Morganti et al. (2001); P2: Peck et al. (1999).

have investigated this using a sample of 32 CSS and GPS sources, and have also examined the dependence of HI column density and velocity shift of the primary absorption component relative to the systemic velocity, on source symmetry parameters.

4.2 The sample of sources

Our sample consists of all CSS and GPS sources identified with radio galaxies and quasars for which we could compile information on the HI column density and core flux density or an upper limit to it either from the literature or our observations. CSS and GPS sources such as J1347+1217 (4C+12.50) and J1407+2827 (Mrk668, OQ208), which have prominent HI absorption lines and well-defined radio structures have not been included because they are classifed as Seyferts in the literature (e.g. Hurt et al. 1999; Gallimore et al. 1999). The radio source J1415+1320 (OQ122) which has an HI absorption line (Carilli et al. 1992) but has been identified as a BL Lac object possibly residing in a spiral host galaxy (Wurtz, Stocke & Yee 1996) has also not been considered. For this study, a core is defined to be a compact feature between the two outer lobes of emission. For those without a detected core, the upper limits to the core flux density are 3 times the rms noise in the image, and have been estimated only for those sources whose largest angular size is at least 5 times the resolution element. The fraction of emission from the core, f_c, or an upper limit to it at an emitted frequency of 8 GHz has been estimated for each source. To estimate this fraction, we have used a spectral index of 0 and 1 for the core and extended emission respectively, unless information was available in the literature.

The sample consisting of 32 objects of which 14 are GPS and 18 are CSS objects is listed in Table 4.1. 23 of these are associated with galaxies and 9 with quasars. The projected linear size of the sample ranges from 0.02 to 11.3 kpc with a median value of 0.68 kpc, while the 5-GHz luminosity ranges from 1.3×10^{25} to 1.2×10^{28} W Hz^{-1} with a median value of 7.6×10^{26} W Hz^{-1}. The values of f_c range from <0.001 to 0.279 with a median value of 0.011, while those of N(HI) range from $<0.06\times10^{20}$ to 84.2×10^{20} cm^{-2} with a median value which is less than 1.8×10^{20} cm^{-2}. In this chapter, we will refer to sources with core prominence lesser and greater than the median value as having lower and intermediate values. The sources with the highest values of f_c are not represented in our sample since they would not be classified as CSS and GPS objects.

4.3 Dependence of HI column density on core prominence

To examine the dependence of HI column density on core prominence and also check for consistency with the unification scheme for radio galaxies and quasars, we plot the HI column density against the core fraction (Fig. 4.1). In our sample, there is only one HI detection for the 9 quasars and 15 detections for the 23 galaxies, consistent with orientation effects playing a significant role in the detection of HI absorption. The quasars have a higher median value of f_c of $\sim$0.028 compared with 0.011 for the galaxies. These trends are broadly consistent with the expectations for the unification scheme.

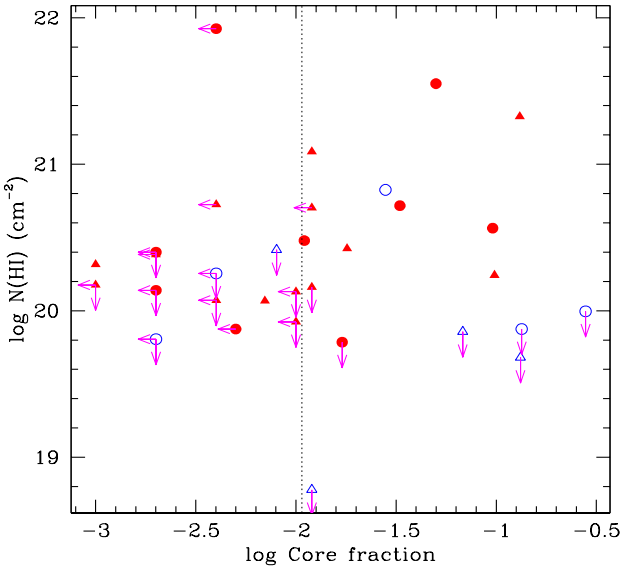

Figure 4.1: Neutral hydrogen column density as a function of core fraction. The solid symbols (in red) correspond to galaxies while open symbols (in blue) denote quasars. Circles denote GPS objects while triangles denote CSS sources. Upper limits are marked by arrows. The vertical dashed line marks the median value of f_c for galaxies.

One of the striking features seen in Fig. 4.1 is that 10 of the 15 galaxies that have a detected HI absorption feature, also have a detected radio core, compared with only 2 out of 8 sources without an HI detection. This suggests that detection of a radio core in galaxies enhances the probability of detecting a 21-cm absorption feature. Dividing the galaxies into two roughly equal groups at the median value of $f_c\sim0.011$, 9 of the 11 with $f_c\geq0.011$ (i.e. intermediate values of core fraction) have a detected absorption feature compared with 6 out of 12 detections in the other group with lower values of f_c. The median value of N(HI), using upper limits as their values, for the intermediate f_c group is $\sim3.7\times10^{20}$ cm^{-2}

compared with 1.5×10^{20} cm^{-2} for the lower f_c group. A Kolmogorov-Smirnov test shows the distributions to be different at a significance level of ∼95 per cent. Thus for galaxies, there is a tendency for the detection rate as well as the column density to increase with the degree of core prominence. For the 9 quasars in our sample, there is only one detection and hence it is not meaningful to do a similar exercise. But clearly, sources with the lowest values of f_c do not tend to have the higher values of N(HI).

It is important to enquire whether such a trend is consistent with the unification scheme for radio galaxies and quasars. The deficit of high column density values for sources with low values of f_c can be understood in a scenario where the radio source sizes are larger than the scale of the circumnuclear disk which contributes most of the absorbing gas, so that the line of sight to the lobes at very large inclinations (corresponding to small values of f_c) does not intersect the HI disk. For intermediate values of f_c, one would then expect higher detection rate as well as higher values of N(HI) as seen in Fig. 4.1. For angles close to the line of sight, which would have the highest values of f_c, one would expect small values of N(HI) and much lower detection rates due to the line of sight passing largely through the ionization cone and also through regions of the disk with a high spin temperature due to the presence of an AGN (Bahcall & Ekers 1969). Such sources will usually get classified as compact flat spectrum (CFS) sources and not many of them with similar properties as the sources in our sample have been searched for 21-cm absorption (cf. Gupta et al. 2006 or see Chapter 2).

4.3.1 Dependence on linear size

The neutral hydrogen column density as a function of linear size for our sample of 32 radio sources is shown in Fig. 4.2. This shows the anti-correlation between the HI column density and source size reported by Pihlström et al. (2003) and extended to a larger sample of 96 sources by Gupta et al. (2006). Thus detection probability of 21-cm absorption feature is higher for both small sources and those with intermediate values of core prominence. It may be noted that projected linear size and f_c for this sample show no significant relation.

4.4 HI and symmetry parameters

In addition to the circumnuclear disk, absorption could also occur in neutral clouds that are part of the gas that has been accelerated by interaction with a radio jet. Gas outflows as fast and broad as ∼1000 km s^{-1} have been detected in a number of radio sources in neutral as

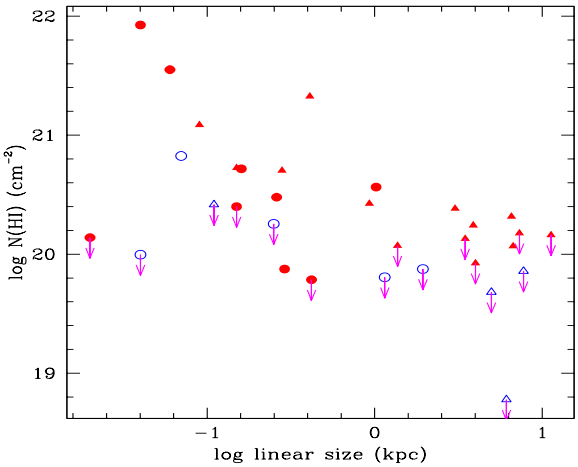

Figure 4.2: Neutral hydrogen column density as a function of projected linear size of the radio sources. See caption of Fig. 4.1 for the meaning of the various colours and symbols.

well as ionised gas (see Morganti, Tadhunter & Oosterloo 2005). The kinematical and spatial properties of these suggest that they are being driven by the same mechanism i.e. interaction with the expanding radio jets. The dynamical interaction of the radio source with these clouds could distort the morphology of the radio source thereby affecting the symmetry parameters such as the separation ratio and the misalignment angle. The separation ratio, R_θ, is defined to be the ratio of the separation of the further component from the core to the nearer one, while the misalignment angle, Δ, is defined to be the supplement of the angle formed at the core by the outer hotspots. Such jet-cloud interactions may also affect the velocity of the absorbing cloud relative to the systemic velocity of the galaxy. However, we find no evidence of any significant dependence of the HI column density as well as the relative velocity of the primary absorption component on either the separation ratio or the misalignment angle (Figs. 4.3 and 4.4). But this does not rule out the importance of the role played by jet-cloud interactions in the observed structures of these sources as there exists significant evidence for this in terms of structural, brightness and polarization symmetry parameters (Saikia et al. 1995; 2001; Saikia & Gupta 2003).

4.5 Summary

For a sample of CSS and GPS objects, we have examined the dependence of HI column density on the degree of core prominence and projected linear size. In our sample, 15 out of 23 galaxies exhibit 21-cm absorption as against 1 out of 9 quasars, which is broadly

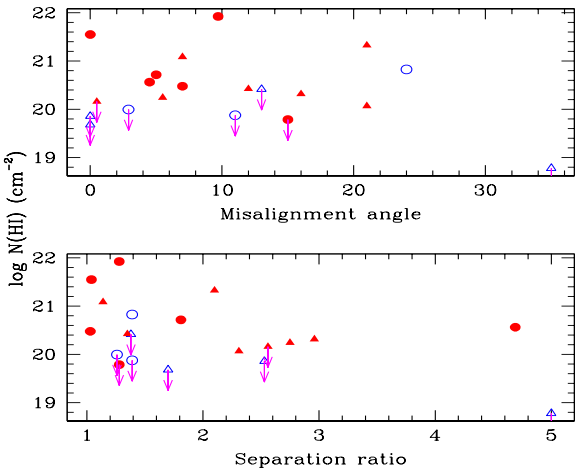

Figure 4.3: Neutral hydrogen column density as a function of radio source symmetry paramters i.e. the separation ratio and misalignment angle. See caption of Fig. 4.1 for the meaning of the various colours and symbols.

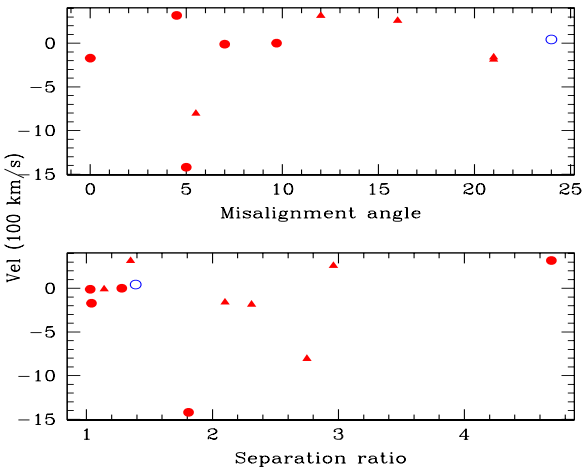

Figure 4.4: The plot of velocities for the principal HI absorption components with respect to the systemic velocity estimated from optical lines as a function of symmetry parameters. See caption of Fig. 4.1 for the meaning of the various colours and symbols.

consistent with the unification scheme. The detection rate as well as the HI column density appears to be larger for galaxies with more prominent cores, with the higher column densities occurring in intermediate values of f_c and not in the lowest values of f_c. This broad trend can be understood in the unification scheme if the lines of sight towards the lobes of sources with the lowest values of f_c, which are inclined at the largest angles to the line of sight, do not pass through the circumnuclear HI disk. This could happen if the source sizes are larger than the scale of the disk. It is interesting to note that 10 of the 15 galaxies with a detected HI absorption feature also has a detected radio core, compared with 2 out of 8 galaxies without any HI detection. Our sample also shows an inverse relationship between the HI column density and the projected linear size, suggesting that both small sizes and more prominent cores enhance the probability of detecting HI absorption in CSS and GPS objects.

In addition to the disk, HI absorption may also be due to clouds of cold gas, some of which may have interacted with the radio jet. We, however, find that the HI column density and the velocity shift of the primary absorption component relative to the systemic velocity show no dependence on the degree of misalignment and the separation ratio.

Bibliography

[1] Akujor C.E., Spencer R.E., Zhang F.J., Davis R.J., Browne I.W.A., Fanti C., 1991, MNRAS, 250, 215

[2] Bahcall J.N., Ekers R.D., 1969, ApJ, 157, 1055

[3] Barthel P.D., 1989, ApJ, 336, 606

[4] Baum S.A., O'Dea C.P., de Bruyn A.G., Murphy D.W., 1990, A&A, 232, 19

[5] Bondi M., Garrett M.A., Gurvits L.I., 1998, MNRAS, 297, 559

[6] Carilli C.L., Perlman E.S., Stocke J.T., 1992, ApJ, 400, L13

[7] Carilli C.L., Menten K.M., Reid M.J., Rupen M.P., Yun M.S., 1998, ApJ, 494, 175

[8] Conway J.E., Blanco P.R., 1995, ApJ, 449, L131

[9] Dallacasa D., Fanti C., Fanti R., Schilizzi R.T., Spencer R.E., 1995, A&A, 295, 27

[10] Fanti C. et al., 1989, A&A, 217, 44

[11] Feng W.X., An T., Hong X.Y., Zhao Jun-Hui, Venturi T., Shen Z.Q., Wang W.H., 2005, A&A, 434, 101

[12] Fey A.L., Charlot P., 2000, ApJs, 128, 17

[13] Fey A.L., Clegg A.W., Fomalont E.B., 1996, ApJS, 105, 299

[14] Fomalont E.B., Frey S., Paragi Z., Gurvits L.I., Scott W.K., Taylor A.R., Edwards P.G., Hirabayashi H., 2000, ApJS, 131, 95

[15] Fomalont E.B., Petrov L., MacMillan D.S., Gordon D., Ma C., 2003, AJ, 126, 2562

[16] Gallimore J.F., Baum S.A., O'Dea C.P., Pedlar A., Brinks E., 1999, ApJ, 524, 684

[17] Giovannini G., Cotton W.D., Feretti L., Lara L., Venturi T., 2001, ApJ, 552, 508

[18] Gupta Neeraj, Srianand R., Saikia D.J., 2005, MNRAS, 361, 451

[19] Gupta Neeraj, Salter C.J., Saikia D.J., Ghosh T., Jeyakumar S., 2006, MNRAS, 373, 972

[20] Hurt T., Antonucci R., Cohen R., Kinney A., Krolik J., 1999, ApJ, 514, 579

[21] Kapahi V.K., Saikia D.J., 1982, JApA, 3, 465

[22] Lüdke E., Garrington S.T., Spencer R.E., Akujor C.E., Muxlow T.W.B., Sanghera H.S., Fanti, C., 1998, MNRAS, 299, 467

[23] Morganti R., Oosterloo T.A., Tadhunter C.N., van Moorsel G., Killeen N., Wills K.A., 2001, MNRAS, 323, 331

[24] Morganti R., Tadhunter C.N., Oosterloo T.A., 2005, A&A, 444, L9

[25] Mutel R.L., Phillips R.B., Skuppin R., 1981, AJ, 86, 1600

[26] O'Dea C.P., 1998, PASP, 110, 493

[27] Ojha R. et al., 2004, AJ, 127, 3609

[28] Orr M.J.L., Browne I.W.A., 1982, MNRAS, 200, 1067

[29] Owsianik I., Conway J.E., Polatidis A.G., 1998, A&A, 336, L37

[30] Pearson T.J., Readhead A.C.S., 1988, ApJ, 328, 114

[31] Peck A.B., Taylor G.B., 2000, ApJ, 534, 90

[32] Peck A.B., Taylor G.B., Conway J.E., 1999, ApJ, 521, 103

[33] Peck A.B., Taylor G.B., Fassnacht C.D., Readhead A.C.S., Vermeulen R.C., 2000, ApJ, 534, 104

[34] Perlman E.S., Carilli C.L., Stocke J.T., Conway J., 1996, AJ, 111, 1839

[35] Pihlström, Y.M., 2001, PhD Thesis, Chalmers University of Technology

[36] Pihlström Y.M., Conway J.E., Vermeulen R.C., 2003, A&A, 404, 871

[37] Polatidis A.G., Wilkinson P.N., Xu W., Readhead A.C.S., Pearson T.J., Taylor G.B., Vermeulen R.C., 1995, ApJS, 98, 1

[38] Saikia D.J., Gupta N., 2003, A&A, 405, 499

[39] Saikia D.J., Jeyakumar S., Wiita P.J., Sanghera H.S., Spencer R.E., 1995, MNRAS, 276, 1215

[40] Saikia D.J., Holmes G.F., Kulkarni A.R., Salter C.J., Garrington S.T., 1998, MNRAS, 298, 877

[41] Saikia D.J., Jeyakumar S., Salter C.J., Thomasson P., Spencer R.E., Mantovani F., 2001, MNRAS, 321,37

[42] Sanghera H.S., Saikia D.J., Lüdke E., Spencer R.E., Foulsham P.A., Akujor C.E., Tzioumis A.K., 1995, A&A, 295, 629

[43] Stanghellini C., Dallacasa D., O'Dea C.P., Baum S.A., Fanti R., Fanti, C., 2001, A&A, 377, 377

[44] Strom R.G., Riley J.M., Spinrad H., van Breugel W.J.M., Djorgovski S., Liebert J., McCarthy P.J., 1990, A&A, 227, 19

[45] Taylor G.B., Vermeulen R.C., 1997, ApJ, 485, L9

[46] Taylor G.B., Vermeulen R.C., Pearson T.J., Readhead A.C.S., Henstock D.R., Browne I.W.A., Wilkinson P.N., 1994, ApJS, 95, 345

[47] Taylor G.B., Marr J.M., Pearson T.J., Readhead A.C.S., 2000, ApJ, 541, 112

[48] Tzioumis A. et al., 2002, A&A, 392, 841

[49] Urry C.M., Padovani P., 1995, PASP, 107, 83

[50] van Gorkom J.H., Knapp G.R., Ekers R.D., Ekers D.D., Laing R.A., Polk K.S., 1989, AJ, 97, 708

[51] Vermeulen R.C. et al., 2003, A&A, 404, 861

[52] Wurtz R., Stocke J.T., Yee H.K.C., 1996, ApJS, 103, 109

[53] Xiang L., Stanghellini C., Dallacasa D., Haiyan Z., 2002, A&A, 385, 768

[54] Xu W., Readhead A.C.S., Pearson T.J., Polatidis A.G., Wilkinson P.N., 1995, ApJS, 99, 297

[55] Zensus J.A., Ros E., Kellermann K.I., Cohen M.H., Vermeulen R.C., Kadler M., 2002, AJ, 124, 662

Chapter 5

Associated 21-cm absorption towards the cores of radio galaxies

5.1 Introduction

An understanding of the properties of the gaseous environments of radio galaxies and quasars could provide valuable insights towards understanding the phenomenon of radio activity associated with these objects and their evolution. As we saw in Chapter 4, such studies also enable us to test consistency of these properties with the unified schemes for these objects. An important way of probing the neutral component of this gas over a wide range of length scales is via 21-cm HI absorption towards radio sources of different sizes. These range from the sub-galactic sized compact steep-spectrum (CSS) and gigahertz peaked-spectrum (GPS) sources, which are believed to be young ($<10^5$ yr), as compared with the larger sources which could extend to over a Mpc and are typically $\sim 10^8$ yr old.

HI absorption lines are seen more often towards CSS and GPS objects, with the HI column densities being anticorrelated with the source sizes (cf. Chapters 2 and 4). Compared with 21-cm absorption searches towards CSS and GPS sources the extended radio galaxies have received relatively less attention. Notable exceptions to this are the studies by van Gorkom et al. (1989) and Morganti et al. (2001) whose samples also contained larger radio sources in addition to the subgalactic-sized compact ones. To investigate whether the circumnuclear gas evolves as the source grows from CSS and GPS scales to the large radio sources, one needs to probe the distribution and properties of this gas on similar scales with comparable sensitivities. This can be achieved via 21-cm absorption measurements towards the compact cores of the large objects using high-resolution observations where the core is

clearly resolved from the more extended bridge emission. Such observations will also help clarify any differences between FR I and FR II sources. In this chapter I present the results of our GMRT survey to search for 21-cm absorption associated with the cores of FR I and FR II radio galaxies and examine the properties of 21-cm absorption by combining our results with those available in the literature. The observations are described in Section 5.2, while in Section 5.3 we present our discovery of 21-cm absorption towards the core of the FR II radio galaxy J2245+3941 (3C 452) and examine the properties of this 21-cm absorber in the light of observations at other wavelengths. In Section 5.4 we combine our results with those of similar searches and discuss the statistical trends in gas properties with respect to radio-source characteristics. The results are summarized in Section 5.5.

5.2 Observations

We observed 10 FR I and FR II radio galaxies with GMRT over the period of 2004-2006. The list of sources and some of their properties are presented in Table 5.1. These sources, which have been selected largely from the 3CR and B2 samples, are part of our larger sample of 22 radio galaxies which have been selected on the basis that core flux density at 1.4 GHz is greater than 100 mJy and radio structure is such that core emission can be distinguished from more extended bridge emission at spatial resolutions of few arcseconds. The subset of sources observed with GMRT so far consists of 6 FR I radio sources and 4 FR II radio sources. Their projected linear sizes range from ∼60 kpc to as large as ∼1 Mpc. Amongst the FR II radio sources all are broad-line radio galaxies (BLRG) except for J2245+3941 (3C 452) which is a narrow-line radio galaxy (NLRG). The subset of 10 sources presented here are randomly drawn from the larger sample. A baseband bandwidth (BB BW) of 4 MHz split into 128 channels was usually used for these observations, except for J0313+4120 for which a BB BW of 8 MHz was used (see Table 5.2). For the observations of J2245+3941 (3C 452) on 2005 Dec 11 we made use of the new high-resolution mode of the GMRT correlator software. This allows one to split the baseband bandwidth into 256 channels, instead of the usual 128 channels. This provided us a spectral resolution of ∼3.6 km s^{-1} in this case. The local oscillator chain and FX correlator system were tuned to centre the baseband bandwidth at the expected redshifted 21-cm frequency. In all our observations we observed standard flux density calibrators (3C 48, 3C 147 and 3C 286) every 3 hours to correct for the variations in amplitudes and bandpass. A compact radio source was also observed approximately every 35 minutes for phase calibration of the array. The data were reduced in the standard way using Astronomical Image Processing System

Table 5.1: Radio sources observed with the GMRT.

Source name	Alt. name	Opt. type	Redshift	S_{5GHz}	P_{5GHz}	Type	LAS	LLS	Ref.
					10^{25}				
				mJy	W/Hz		$''$	kpc	
(1)	(2)	(3)	(4)	(5)	(6)	(7)	(8)	(9)	(10)
J0209+3547	4C+35.03		0.03773	989	0.31	FR I	83	61	0
J0223+4259	3C 66B	WLRG	0.021258	2820	0.28	FR I	645	274	1
J0313+4120	S4	BLRG	0.13400	457	1.88	FR II	570	1340	2
J0334+3921	4C+39.12		0.020591	538	0.05	FR I	357	147	1
J0418+3801	3C 111	BLRG	0.04850	5807	3.04	FR II	205	192	0
J0758+3747	3C 189		0.042836	1049	0.43	FR I	136	113	0
J1835+3241	3C 382	BLRG	0.057870	2270	1.71	FR II	171	189	3
J1836+1942	PKS		0.016144	330	0.02	FR I	962	312	1
J2245+3941	3C 452	NLRG	0.08110	3000	4.00	FR II	256	386	0
J2338+2701	3C465	WLRG	0.030221	2780	0.57	FR I	655	391	1

Col. 1: source name; col. 2: alternative name; col. 3: optical type as and when available in the literature, where BLRG = broad-line radio galaxy, NLRG = narrow-line radio galaxy and WLRG = weak-line radio galaxy (cf. Morganti et al. 2001); col. 4 and col. 5: redshift and total 5-GHz flux density respectively from NED; col. 6: 5-GHz luminosity in the rest frame of the source; col. 7: radio morphology i.e. FR I or FR II; cols. 8 & 9: largest projected angular (LAS) and linear (LLS) size in arcsec and kpc respectively; col. 10: references for the radio structure.

References for the largest angular sizes – 0: This Chapter; 1: NRAO VLA Sky Survey (NVSS) at 1.4 GHz; 2: de Bruyn 1989; 3: Leahy & Perley 1991

(AIPS) package. After the initial flagging or editing of bad data and calibration, source and calibrator data were examined for baselines and timestamps affected by Radio Frequency Interference (RFI). These data were excluded from further analysis. A continuum image of the source was made using calibrated data averaged over ∼60 line-free channels. Due to our interest in absorption towards compact components like the core, the imaging was done without any *uv* cut-off or tapering in the visibility plane. This provided us with the highest possible resolution. This image was then self-calibrated until a satisfactory map was obtained. The self-calibration complex gains determined from this were applied to all the frequency channels and continuum emission was subtracted from this visibility data cube using the same map. Spectra at various positions on the radio galaxy were extracted from this cube. The whole process was done separately for Stokes RR and LL to check for consistency. The two polarization channels were then combined to get the final Stokes I spectrum, which was then shifted to the heliocentric frame. From our search for HI absorption towards the 10 radio sources we report 1 new 21-cm absorption detection which is towards the core of radio galaxy J2245+3941 (3C 452) and present the upper limits on N(HI) for the remaining 9 sources (Table 5.2). In the Figs. 5.1−5.9, we present the final radio continuum images (i.e. same as the one used for continuum subtraction) and 21-cm absorption spectra for the galaxies with only non-detections. Large scale radio morphology i.e. FR I or FR II is well represented in these images except for J0313+4120 and J1836+1942 where most of the diffuse emission is resolved out in our GMRT images. The continuum image and spectra for J2245+3941 (3C 452) are presented in the next section where we also examine the properties of this 21-cm absorber.

5.3 21-cm absorption towards the core of 3C 452 (J2245+3941)

3C 452 is a high-excitation narrow-line FR II radio galaxy at the redshift, z_{em}=0.08110 determined using the [O III] λλ4959, 5007 Å emission lines (Lawrence et al. 1996; Jackson & Rawlings 1997). This is consistent with the estimate from the Hβ line within ∼30 km s^{-1}. However from the data of Lawrence et al. we find that the low-ionization forbidden emission lines namely, [O I], [O II], [N II] and [S II] are all systematically red-shifted with respect to it by ∼200 km s^{-1}. Further, the low-ionization lines appear broader (FWHM∼900 km s^{-1}) than the high-ionization ones which have a FWHM of ∼600 km s^{-1}, suggesting that the low-ionization lines may be arising from shock-ionised gas (see Villar-Martin et al. 1999). The total radio luminosity of 3C 452 at 5 GHz is 3.6×10^{25} W Hz^{-1} sr^{-1}, which is well above the dividing line for the two FR types. At radio wavelengths the source exhibits a

Table 5.2: Observational details and results of the search for associated HI absorption.

Source name (1)	Date (2)	Obs. freq MHz (3)	BW MHz (4)	t_{int} hr (5)	Beam $''\times''$ $^\circ$ (6)	Comp. (7)	Peak flux mJy/b (8)	σ mJy/b (9)	$\tau_{1\sigma}$ 10^{-3} (10)	N(HI) 10^{20}cm^{-2} (11)
J0209+3547	2006 Jan	1368.76	4	3.5	2.41×1.91 +20	Core	102	0.91	<8.9	<5.15
J0223+4259	2006 Jan	1390.84	4	4.6	2.64×2.25 −83	Core	170	1.10	<6.5	<3.77
J0313+4120	2004 Jan	1252.56	8	3.0	2.62×2.15 −53	Core	383	1.12	<2.9	<1.68
J0334+3921	2006 Jan	1391.75	4	4.9	2.70×1.99 +53	Core	304	0.85	<2.8	<1.62
J0418+3801	2006 Jan	1354.70	4	5.2	3.15×2.38 +34	EHS	1393	0.90	<0.7	<0.41
						Core	1103	1.05	<1.0	<0.58
						WHS	250	1.03	<4.1	<2.37
J0758+3747	2006 Jan	1362.06	4	5.2	3.12×2.07 +43	Core	184	1.01	<5.5	<3.19
J1835+3241	2006 Mar	1342.70	4	4.5	2.68×2.10 +35	EHS	203	1.05	<5.2	<3.01
						Core	240	1.17	<4.9	<2.84
						WHS	37	1.12	<30.0	<17.4
J1836+1942	2004 Jan	1397.84	4	2.0	3.04×2.10 −70	Core	224	2.10	<9.4	<5.44
J2245+3941	2005 Dec	1313.85	4	5.6	3.14×2.25 +52	EHS	94	1.10	<11.7	<6.77
						Core	194	1.00	58.0	6.39
						WHS	128	1.10	<8.6	<4.98
J2338+2701	2004 Jan	1378.74	4	4.0	2.89×2.24 −50	Core	302	1.63	<5.4	<3.13

Col. 1: source name; col. 2: year and month of observations; col. 3: redshifted 21-cm frequency; col. 4: baseband bandwidth (BW); col. 5: observing time in hr (excluding calibration overheads); cols. 6, 7 & 8: restoring beam, radio component (EHS = eastern hotspot, WHS = western hotspot and Core= radio core) and peak brightness in mJy/beam for the continuum image made using line-free channels respectively; col. 9: rms noise in the spectrum; col. 10: optical depth estimate, and col. 11: HI column density in 10^{20} cm^{-2}, assuming T_s=100 K; upper limits are 3σ values, assuming Δv=100 km s^{-1}and f_c=1.0.

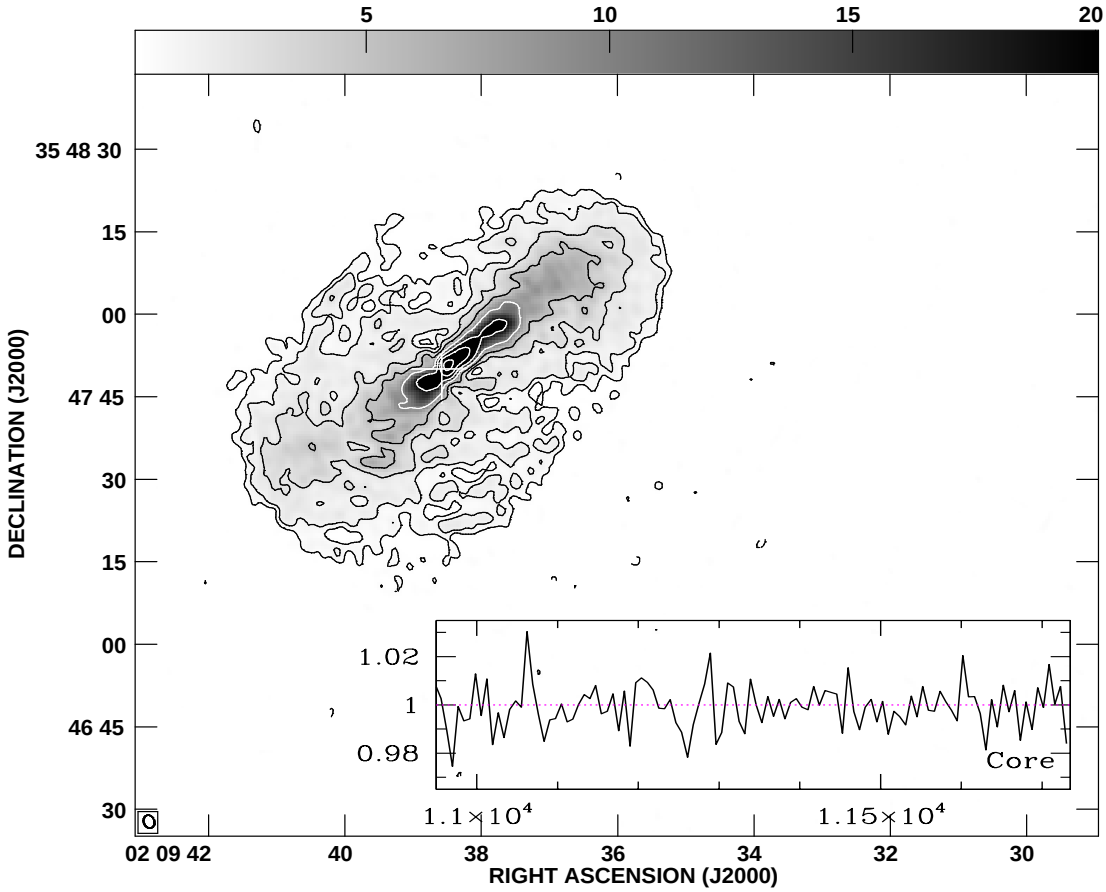

Figure 5.1: Image of J0209+3547 (4C+35.03) with an rms noise of 0.2 mJy/beam. The contour levels are $0.6\times(-1,\ 1,\ 2,\ 4,\ 8,\ 16,\ 32,\ 64,\ 128)$ mJy/beam. The restoring beam of $2.41''\times1.91''$ along position angle 20° is shown as an ellipse and position of the optical host galaxy is marked with a cross. The spectra at the peak intensity pixel in the core is also shown. For this x-axis and y-axis are heliocentric velocity in km s^{-1} and normalised intensity respectively.

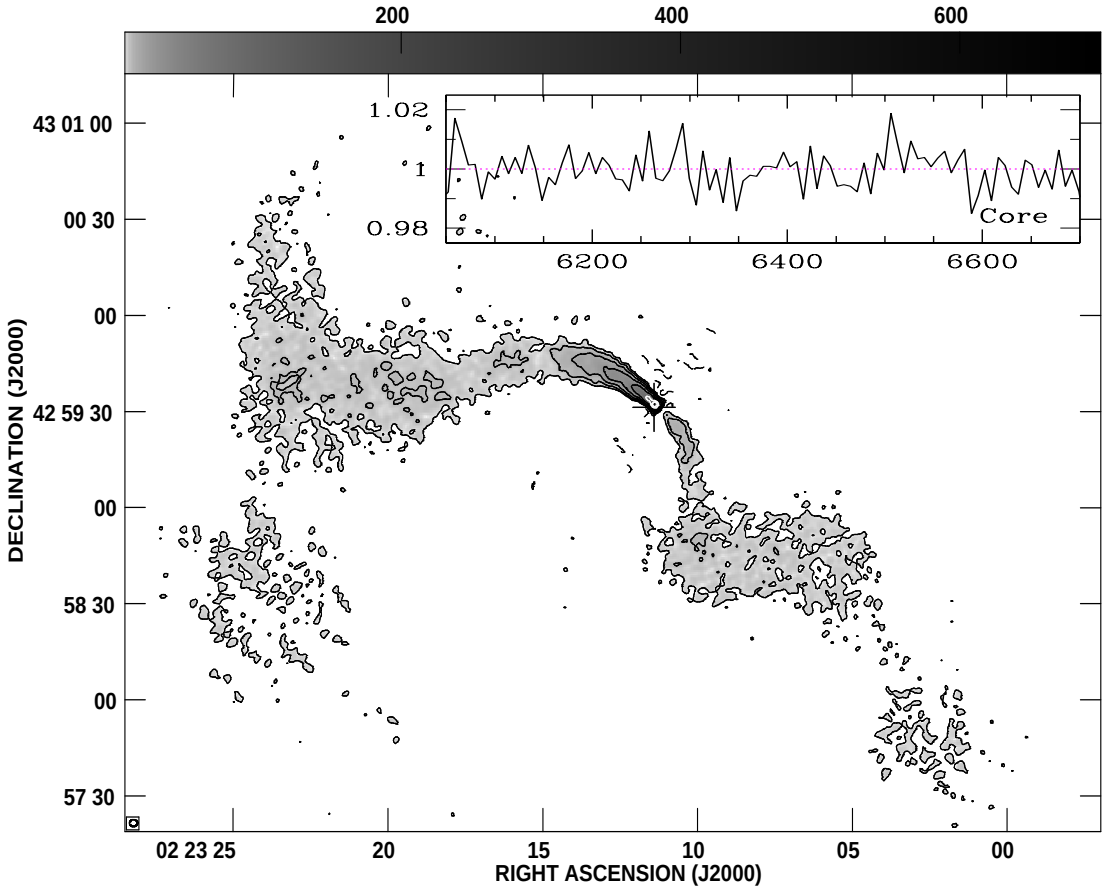

Figure 5.2: Image of J0223+4259 (3C 66B) with an rms noise of 0.6 mJy/beam. The contour levels are $3\times(-1, 1, 2, 4, 8, 16, 32, 45)$ mJy/beam. The restoring beam of $2.64'' \times 2.25''$ along position angle $-83°$ is shown as an ellipse and position of the optical host galaxy is marked with a cross. The spectra at the peak intensity pixel in the core is also shown. For this x-axis and y-axis are heliocentric velocity in km s^{-1} and normalised intensity respectively.

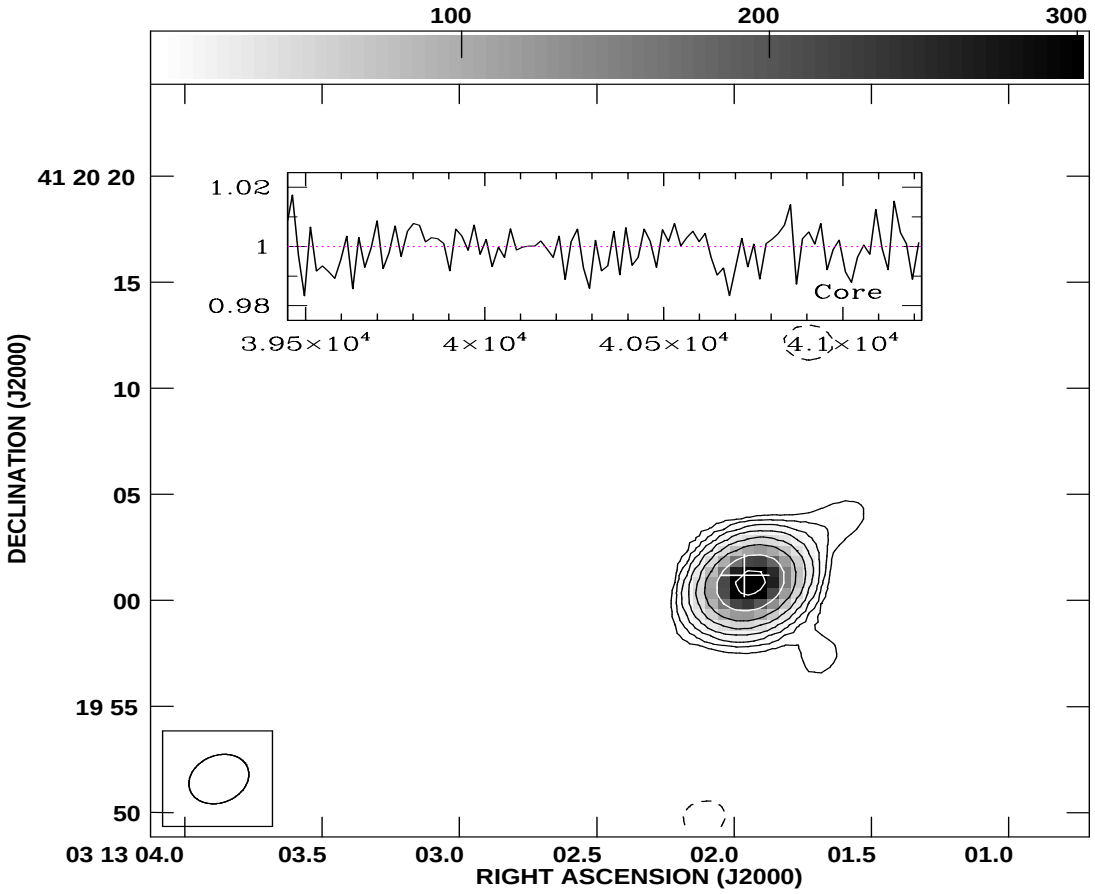

Figure 5.3: Image of J0313+4120 with an rms noise of 0.5 mJy/beam. The contour levels are $2.5\times(-1, 1, 2, 4, 8, 16, 32, 64, 128)$ mJy/beam. The restoring beam of $2.62''\times2.15''$ along position angle -53° is shown as an ellipse and position of the optical host galaxy is marked with a cross. The spectra at the peak intensity pixel in the core is also shown. For this x-axis and y-axis are heliocentric velocity in km s^{-1} and normalised intensity respectively.

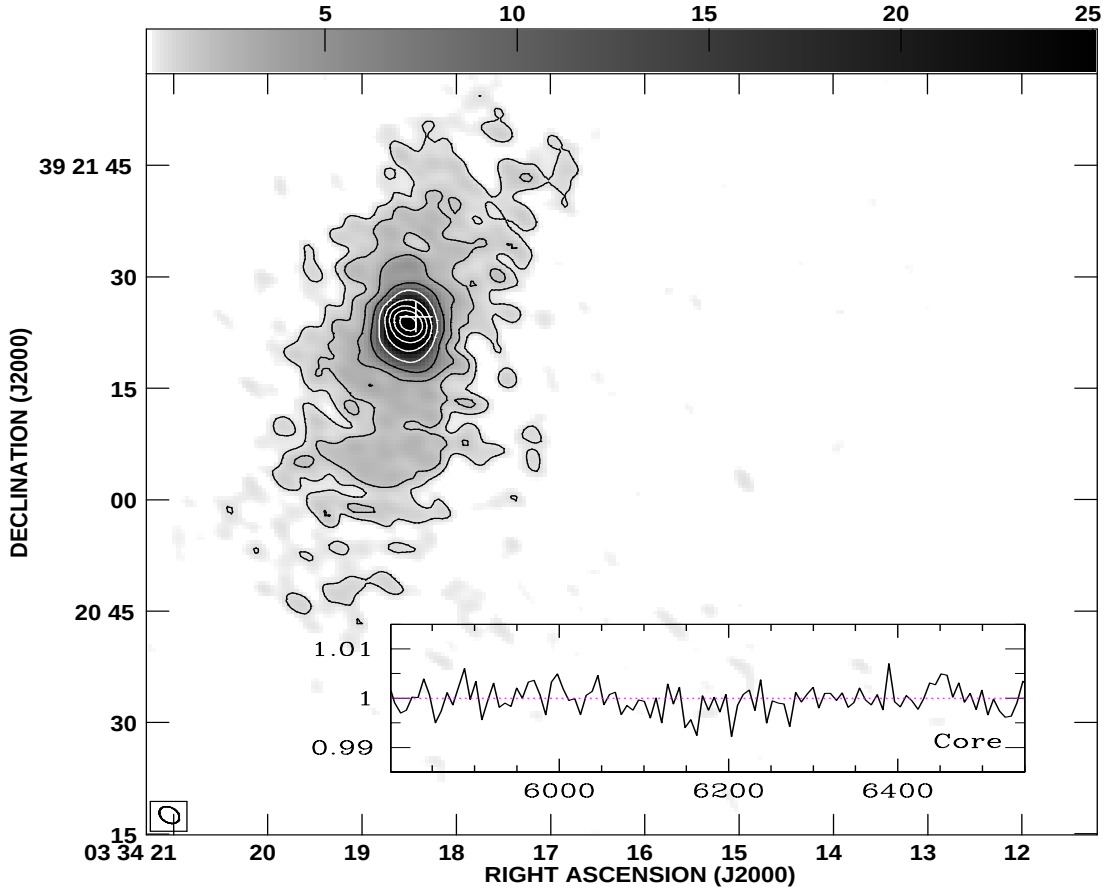

Figure 5.4: Image of J0334+3921 (4C+39.12) with an rms noise of 0.1 mJy/beam. The contour levels are $0.8\times(-1, 1, 2, 4, 8, 16, 32, 64, 128, 256)$ mJy/beam. The restoring beam of $2.70''\times1.99''$ along position angle 53° is shown as an ellipse and position of the optical host galaxy is marked with a cross. The spectra at the peak intensity pixel in the core is also shown. For this x-axis and y-axis are heliocentric velocity in km s^{-1} and normalised intensity respectively.

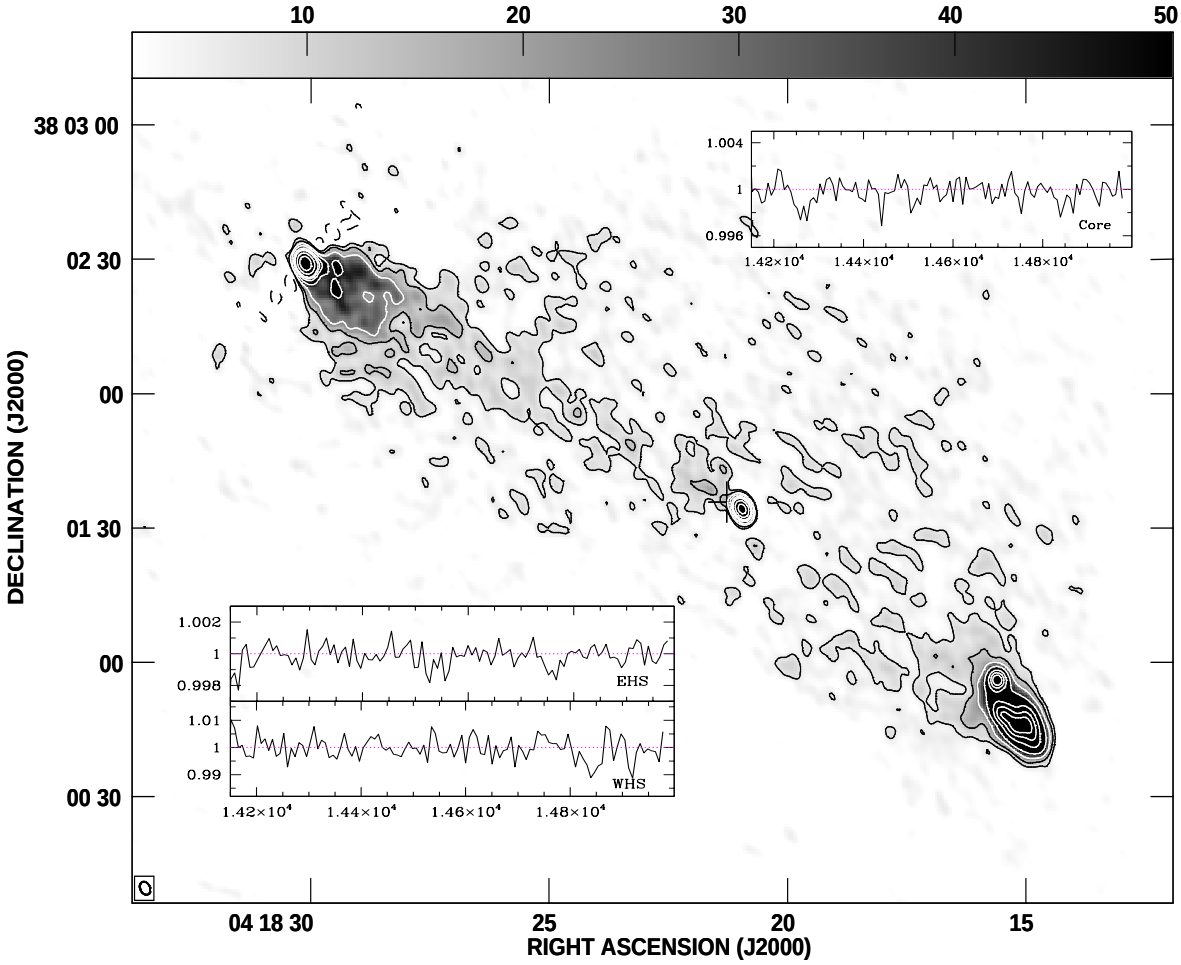

Figure 5.5: Image of J0418+3801 (3C 111) with an rms noise of 0.6 mJy/beam. The contour levels are $6\times(-1, 1, 2, 4, 8, 16, 24, 32, 64, 128)$ mJy/beam. The restoring beam of $3.15''\times2.38''$ along position angle 34° is shown as an ellipse and position of the optical host galaxy is marked with a cross. The spectra at the peak intensity pixel in the core and, eastern and western hotspots are also shown. For these x-axis and y-axis are heliocentric velocity in km s^{-1} and normalised intensity respectively.

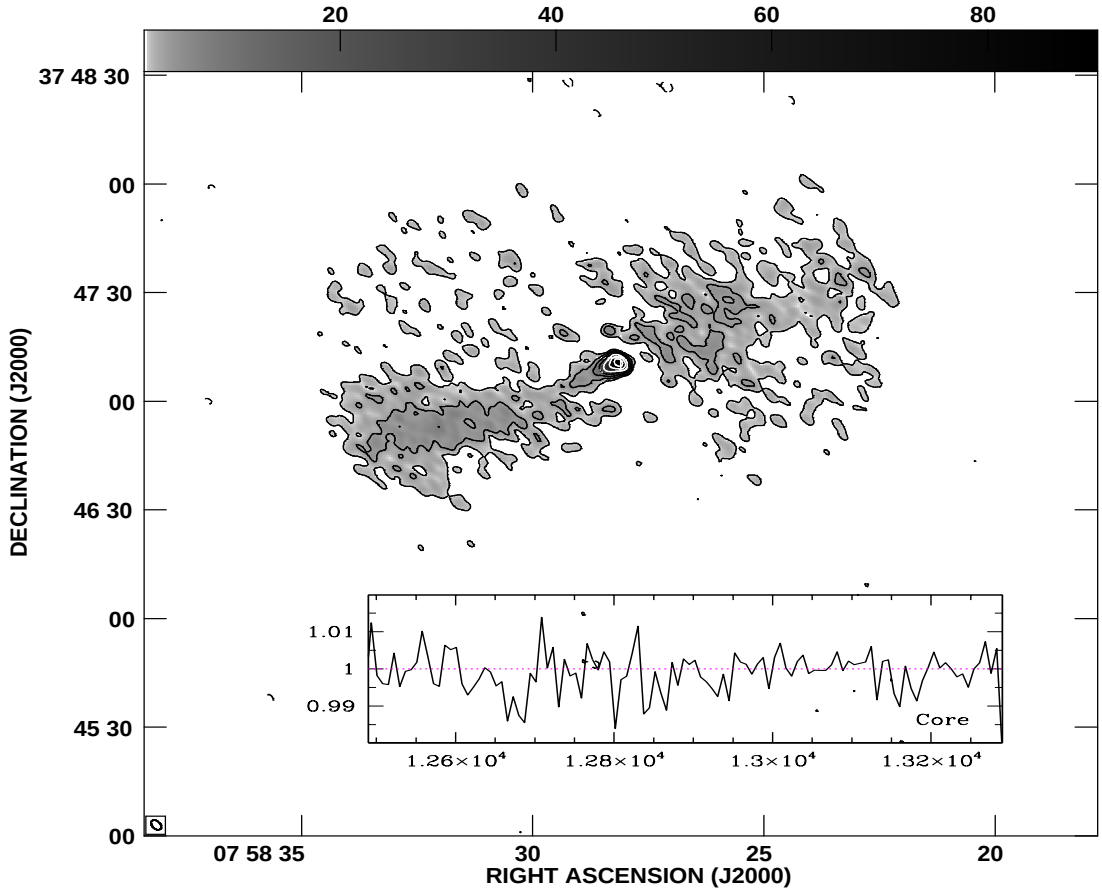

Figure 5.6: Image of J0758+3747 (3C 189) with an rms noise of 0.5 mJy/beam. The contour levels are 2.0×(−1, 1, 2, 4, 8, 16, 32, 64) mJy/beam. The restoring beam of 3.12″×2.07″ along position angle 43° is shown as an ellipse and position of the optical host galaxy is marked with a cross. The spectra at the peak intensity pixel in the core is also shown. For this x-axis and y-axis are heliocentric velocity in km s^{-1} and normalised intensity respectively.

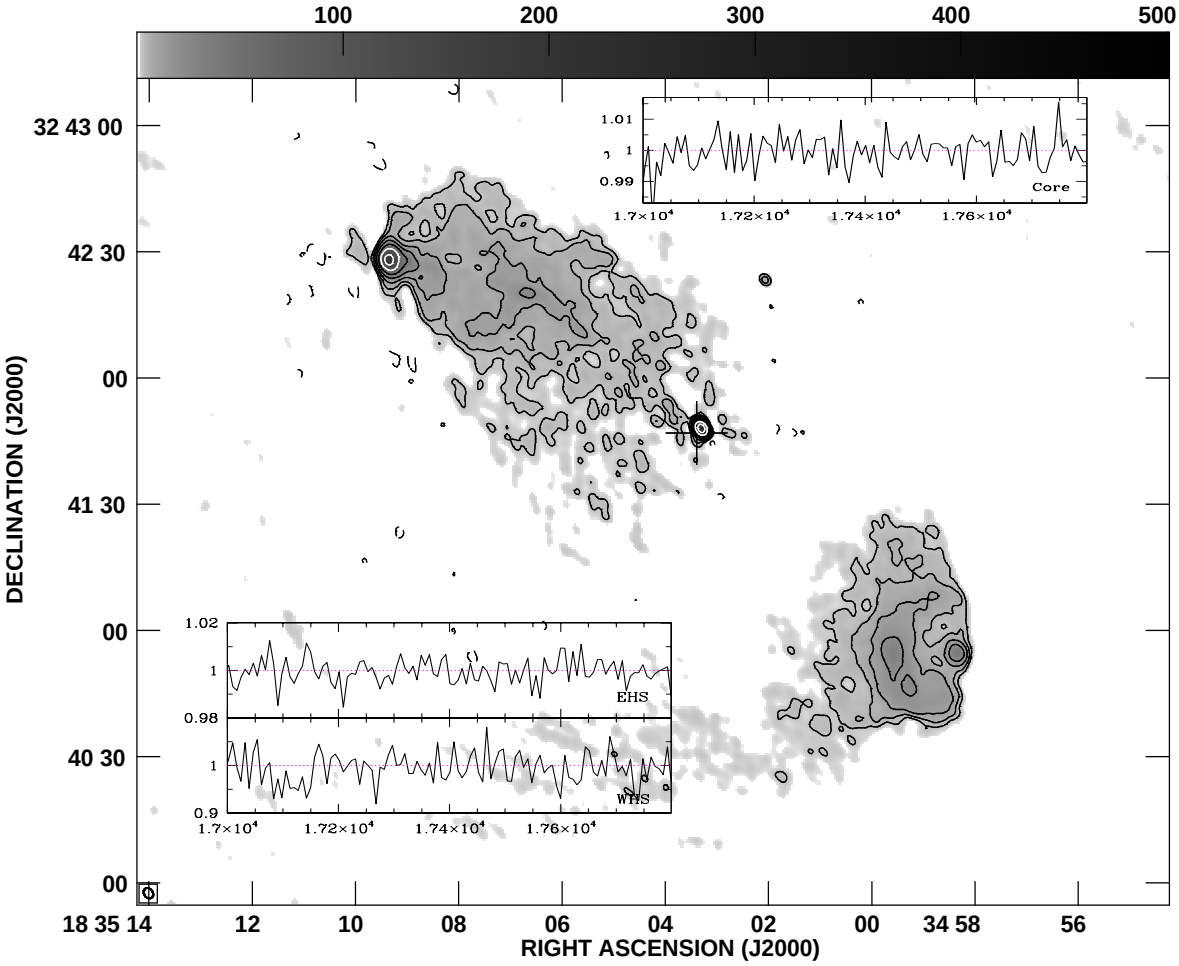

Figure 5.7: Image of J1835+3241 (3C 382) with an rms noise of 0.5 mJy/beam. The contour levels are $2.5\times(-1,\ 1,\ 2,\ 4,\ 8,\ 16,\ 32,\ 64)$ mJy/beam. The restoring beam of $2.68''\times2.10''$ along position angle 35° is shown as an ellipse and position of the optical host galaxy is marked with a cross. The spectra at the peak intensity pixel in the core and, eastern and western hotspots are also shown. For these x-axis and y-axis are heliocentric velocity in km s^{-1} and normalised intensity respectively.

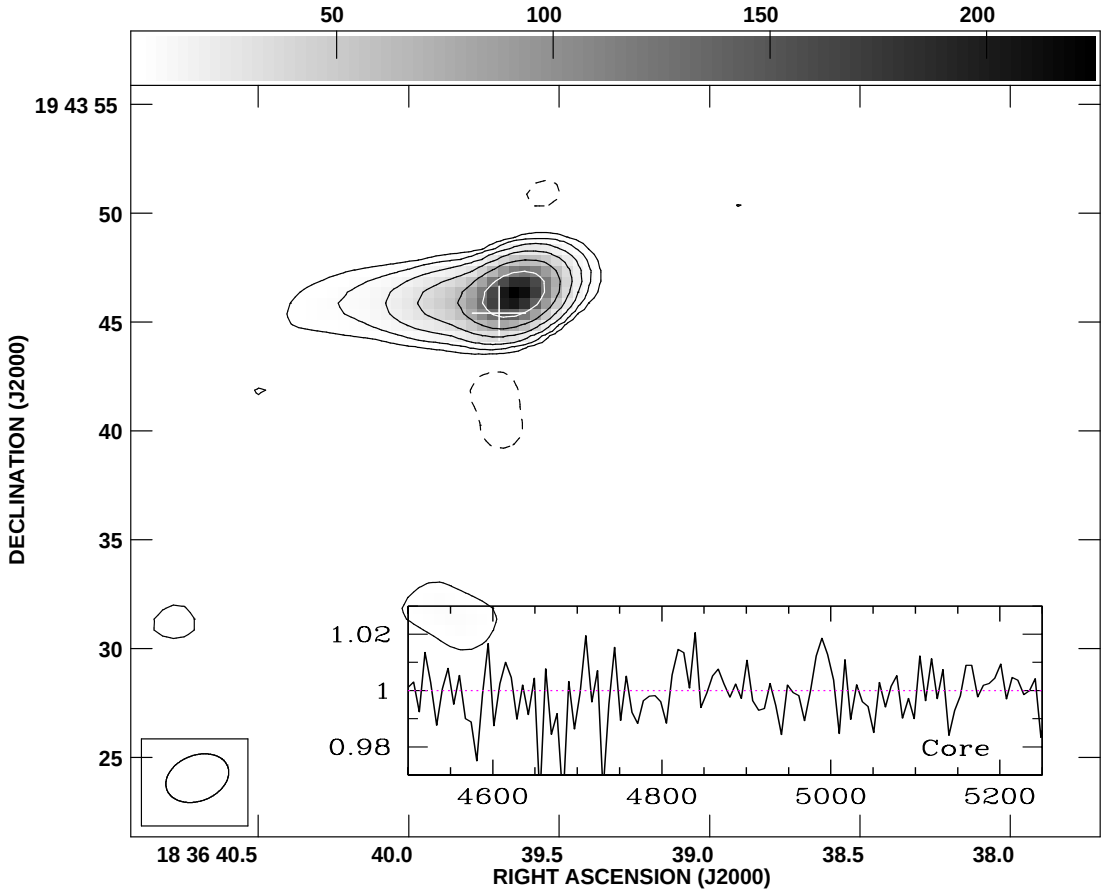

Figure 5.8: Image of J1836+1942 (PKS 1834+196) with an rms noise of 0.8 mJy/beam. The contour levels are $4.0\times(-1, 1, 2, 4, 8, 16, 32, 64)$ mJy/beam. The restoring beam of $3.04''\times2.10''$ along position angle -70° is shown as an ellipse and position of the optical host galaxy is marked with a cross. The spectra at the peak intensity pixel in the core is also shown. For this x-axis and y-axis are heliocentric velocity in km s^{-1} and normalised intensity respectively.

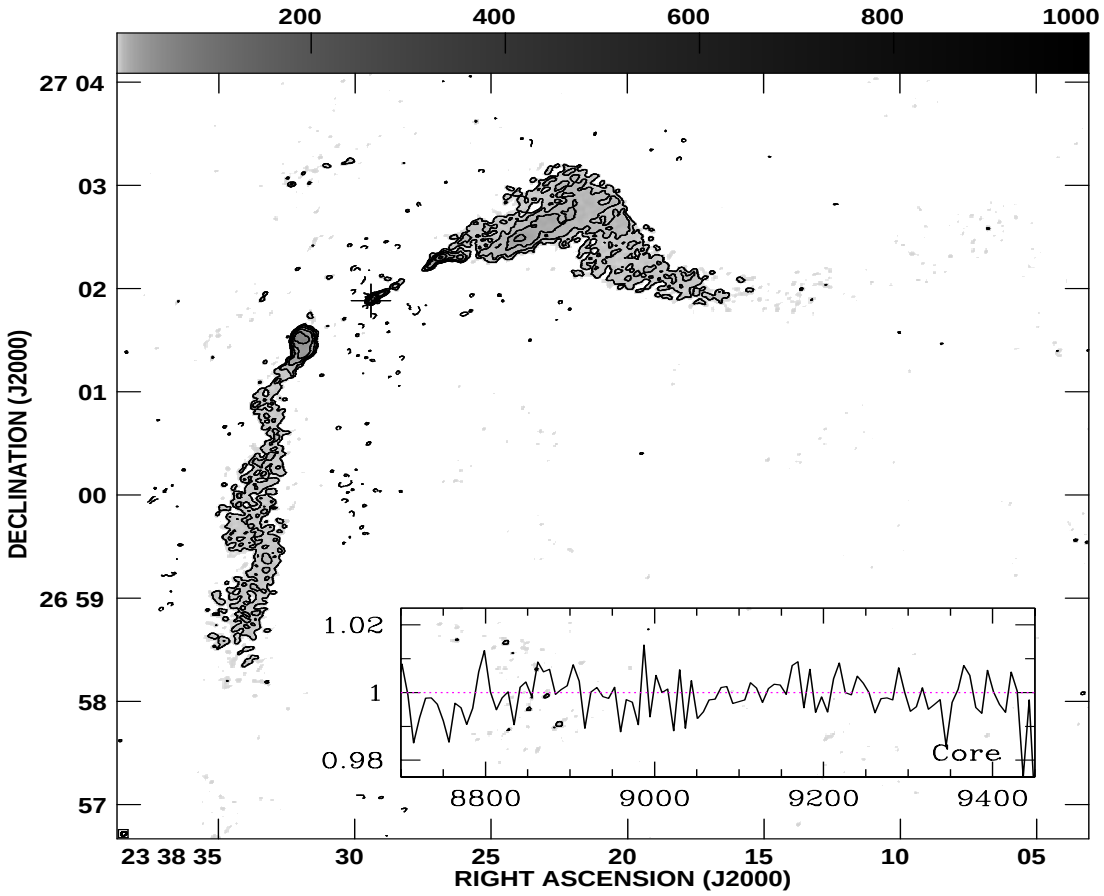

Figure 5.9: Image of J2338+2701 (3C 465) with an rms noise of 0.5 mJy/beam. The contour levels are 2.5×(−1, 1, 2, 4, 8, 16, 32, 64) mJy/beam. The restoring beam of 2.89″×2.24″ along position angle −50° is shown as an ellipse and position of the optical host galaxy is marked with a cross. The spectra at the peak intensity pixel in the core is also shown. For this x-axis and y-axis are heliocentric velocity in km s^{-1} and normalised intensity respectively.

symmetric triple morphology with a largest angular size of 256 arcsec, which corresponds to a linear size of 386 kpc (e.g. Black et al. 1992; Dennett-Thorpe et al. 1999). The compact arcsec-scale radio core is resolved with an angular resolution of ∼1.2 mas into a central peak of emission, which we call the 'nucleus', and symmetric jet-like structures on opposite sides of it (Giovannini et al. 2001). Most of the emission is within ∼5 mas (7.6 pc) of the radio nucleus, although faint emission is seen extending upto ∼20 mas (30 pc) from the radio nucleus on both sides. Using the jet symmetry and core prominence at 5 GHz, Giovannini et al. suggest that this source must be oriented at an angle greater than ∼60° to the line of sight. The core as well as diffuse emission associated with the lobes have been detected in x-rays using the Chandra telescope (Isobe et al. 2002). The HST WFPC-2 image of the host galaxy suggests the presence of a faint dust lane roughly perpendicular to the radio axis of the source (de Koff et al. 2000).

In Fig. 5.10 we present our GMRT image of 3C 452 at 1313 MHz, which shows the radio core, the symmetrically located hotspots on opposite sides of the parent optical galaxy and the extended bridge of emission. The peak flux density of the radio core in our image is 194 mJy/beam. The peak intensities for the brightest components in the eastern and western lobes, referred to as the eastern hotspot (EHS) and the western hotspot (WHS) are given in Table. 5.2. The total flux density in the image is 9.98 Jy at 1313 MHz, which is within a few per cent of the value of 10.2 Jy. The latter has been estimated using the measurements with least errors at 750 and 4850 MHz from the NASA Extragalactic Database. The HI absorption spectra towards the core and hotspots of 3C 452 are presented in Fig. 5.10. HI absorption has been detected clearly towards the core of the radio galaxy while no absorption has been detected towards the hotspots or any other part of the source. The rms noise in the spectra and 1-σ upper limits to the optical depth towards EHS and WHS are presented in Table. 5.2. The HI column density, N(HI), integrated over the entire spectrum using the relation

$$\mathrm{N(HI)} = 1.835 \times 10^{18} \frac{\mathrm{T}_s \int \tau(v) dv}{f_c} \ \mathrm{cm}^{-2}, \tag{5.1}$$

where T_s, τ and f_c are the spin temperature, optical depth at a velocity v and the fraction of background emission covered by the absorber respectively, is $6.39{\times}10^{20}(\mathrm{T}_s/100)(1.0/f_c)$ cm^{-2}. The absorption profile is well fitted with three Gaussian components (Fig. 5.11). The best fit parameters are summarised in Table 5.3. It may be noted that the widths of the components and corresponding column densities are typical of those observed in our Galaxy (e.g. Ferrière 2001; Dickey & Lockman 1990). The absorption profile consists of a strong narrow component near the velocity of the galaxy estimated from the [O III] emission

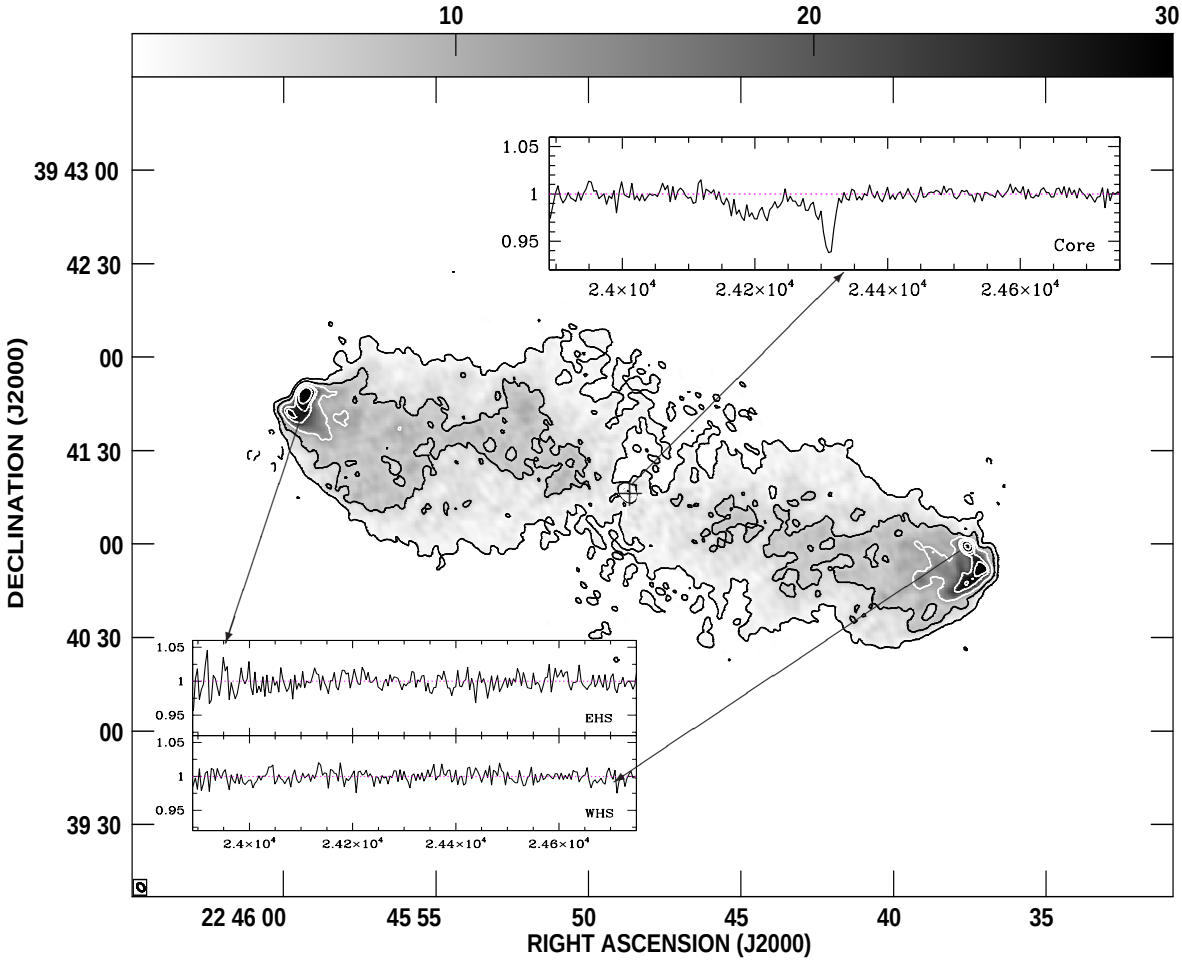

Figure 5.10: GMRT image of J2245+3941 (3C 452) with an rms noise of 0.3 mJy/beam. The contour levels are $1.5\times(-2,-1,\ 1,\ 4,\ 8\ ,\ 16,\ 20,\ 32,\ 64,\ 128)$ mJy/beam. The restoring beam of $3.14''\times2.25''$ along position angle 52° is shown as an ellipse and the position of the optical host galaxy is marked with a cross. The spectra at the peak intensity pixel in the eastern hotspot (EHS), core and western hotspot (WHS) are also shown. For these x-axis and y-axis are heliocentric velocity in km s^{-1} and normalised intensity respectively.

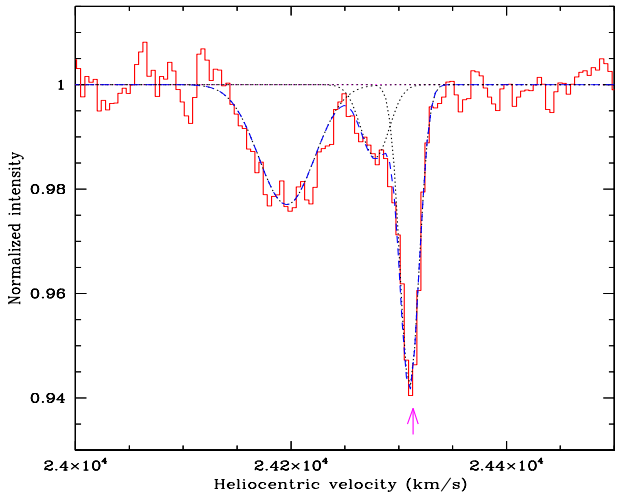

Figure 5.11: The HI absorption spectrum (histogram) towards the core of the radio galaxy 3C 452. The spectrum has been smoothed using a 3-pixel wide boxcar filter. The three Gaussian components fitted to the absorption profile and the sum of these components i.e. the fit are plotted as dotted and dashed lines respectively. The systemic velocity (24313 km s^{-1}) determined using [O III] emission lines has been marked by an arrow.

lines and two broader components blue-shifted with respect to it by about ∼30 and ∼115 km s^{-1}. However different velocities for the host galaxy estimated from different emission lines can sometimes make it difficult to ascertain the kinematics of the absorbing gas (see e.g. Tadhunter et al. 2001; Vermeulen et al. 2006). In 3C 452 the velocity corresponding to the low-ionization lines would imply that the narrow and two broad 21-cm absorption lines are blue-shifted by ∼200, 230 and 315 km s^{-1}. This would then imply that both the [O III] emission and 21-cm absorption lines are associated with outflowing gas. Fast and broad outflows in HI with velocities extending up to several thousand km s^{-1} have been reported for a number of radio galaxies (Morganti, Tadhunter & Oosterloo 2005).

In the following we compare our results with observations at infrared and x-ray wavelengths to constrain some of the properties of the absorbing material. The nuclear extinction of 3C 452 as measured by near-infrared observations is A_v >2.30 (Marchesini, Capetti & Celotti 2005). For the diffuse ISM of our Galaxy, the mean of total neutral hydrogen i.e. N(HI+H_2) is related to visual extinction as

$$N(HI + H_2) = 1.89 \times 10^{21} A_v \, mag^{-1} cm^{-2} \quad (5.2)$$

(Bohlin, Savage & Drake 1978; Cardelli, Clayton & Mathis 1989). Using this relation and assuming that all the gas producing extinction is atomic we get for 3C 452, N(HI)>2.2×10^{21}

Table 5.3: Multiple Gaussian fit to the HI absorption spectrum

Id. no.	v_{hel} km s^{-1}	FWHM km s^{-1}	Frac. abs.	N(HI) $10^{20}(\frac{T_s}{100})(\frac{f_c}{1.0})^{-1}$ cm^{-2}
1	24196	61(3)	0.023(0.001)	2.71
2	24278	31(4)	0.014(0.002)	0.84
3	24310	21(1)	0.058(0.002)	2.35

cm^{-2}. Its comparison with the total neutral hydrogen column density determined from 21-cm absorption implies T_s >350 K for f_c=1.0. In fact, the spin temperature of 21-cm absorbing gas can be much higher than ∼350 K. For the warm neutral medium seen in the Galaxy T_s ranges from 5000−8000 K (Kulkarni & Heiles 1988). Such high spin temperatures are also expected to arise in the proximity of the active nucleus (Bahcall & Ekers 1969).

Using the Chandra telescope, Isobe et al. (2002) detected x-ray emission associated with the core and lobes of the radio galaxy. They infer that a total hydrogen column density N(H)≈6×10^{23} cm^{-2} is required to fit the x-ray spectrum towards the core. Even for a spin temperature of ∼8000 K, the 21-cm absorbing gas has atleast an order of magnitude lesser column density than that required for x-ray absorption. This either implies that the x-ray absorbing gas is different from that responsible for 21-cm absorption or that the 21-cm absorber does not cover the core completely. The nucleus in the 5-GHz VLBI map of Giovannini et al. (2001) has a flux density of only ∼20 mJy. Assuming a spectral index of 0, this would then correspond to f_c ∼0.1. Thus a spin temperature of ∼8000 K and f_c of ∼0.1 are required if the gas producing 21-cm absorption and nuclear extinction also causes the x-ray absorption. It is worth mentioning here that reconciliation of x-ray absorbing column density with the absorbers detected at other wavelengths in AGN is a recurring problem (see e.g. Hamann 1997; Gallimore et al. 1999). In the simplest explanation the x-ray absorber and the UV or 21-cm absorption line systems are not cospatial. For example, in a 21-cm absorption study of a sample of 13 Seyfert galaxies, Gallimore et al. (1999) did not find any correlation between the 21-cm and x-ray absorbing column density. The nuclear extinction measured for a complete sub-sample of 3CR radio sources, which includes 3C 452, ranges from 0 to 9 mag (Marchesini et al. 2004). Adopting 9 mag as an upper limit on A_v for 3C 452 and f_c=1.0 for the 21-cm absorber would then imply that the gas producing 21-cm absorption and nuclear extinction, and x-ray absorption are not cospatial.

HI observations via VLBI techniques are required to constrain the properties and location of the absorbing clouds and further investigate this scenario. The x-ray spectrum of diffuse emission associated with the lobes is consistent with the Galactic value of N(H)=1.2×10^{21} cm^{-2}. This is consistent with the limits on the neutral hydrogen column density derived from the GMRT spectra towards the radio hotspots (Table 5.2).

5.4 Discussion

Of the 10 radio galaxies observed with the GMRT we detect 21-cm absorption associated with the core of 1 radio galaxy i.e. J2245+3941 (3C 452) and report N(HI) upper limits towards the remaining 9 radio galaxies. In order to have a larger sample to examine the trends in gas properties with respect to radio source characteristics we also consider the observational results from other similar searches available in the literature. For this we have considered only those radio interferometric observations having a spatial resolution of few arcseconds or better so as to be able to distinguish the core emission from the more extended bridge emission. In Table 5.4 we present the results of such 21-cm absorption searches. Thus combining the Tables 5.1 and 5.4 we obtain a sample of 44 radio sources, called the 'core sample'. It may be noted that five radio galaxies in the Table 5.4, namely 3C 29, 3C 40, 3C 278, 3C 403 and 3C 445, have 1.4 GHz core flux density less than ∼100 mJy as against the selection criterion of our GMRT sample.

21-cm absorption observations towards the cores of radio galaxies in 'core sample' provides an opportunity to probe the HI content at the subgalactic scales. Results from these can be compared directly with the ones obtained from the absorption studies towards subgalactic-sized compact radio sources (Section 2.4.2). Recall that there exists an anticorrelation between the source N(HI) and source size for the compact sources. For the 'core sample', Fig. 5.12 shows the 21-cm HI column density against projected linear size. T_s =100 K and full coverage of the radio core have been assumed to estimate the column density using Eqn. 5.1. The upper limits on N(HI) for non-detections are calculated from the 3σ limit on the peak optical depth and a velocity width of 100 km s^{-1}. As can be noticed from Fig. 5.12 that N(HI) upper limits for the searches for 21-cm absorption towards the cores of larger radio galaxies have not been as deep as the limits obtained for the searches of compact radio sources (also see Fig. 2.16). This is mainly due to the fact that 1.4 GHz flux densities of these cores is about an order of magnitude weaker than the total radio emission available from the compact radio sources at similar scales. Nevertheless it is interesting to note that for FR I radio sources in the 'core sample' HI absorption

Table 5.4: Sample of radio sources from literature forming the 'core sample'.

Source name	Alt. name	Opt. ID	Redshift	P_{5GHz} $\times 10^{25}$ W/Hz	LAS $''$	LLS kpc	Ref.	Type	N(HI) $\times 10^{20}$ cm^{-2}	V_{shift} km s^{-1}	Ref.
(1)	(2)	(3)	(4)	(5)	(6)	(7)	(8)	(9)	(10)	(11)	(12)
J0037−0109	3C15	WLRG	0.0730	2.0	37.5	52.5	1	FR II	<0.50		M
J0038−0207	3C17	BLRG	0.2197	32.0	28.7	100.5	1	FR II	<1.57		M
J0057+3021	NGC315	NLRG?	0.0165	0.14	3143	1041	14	FR I	4.6	400	G
J0057−0123	3C29	WLRG	0.0450	1.0	120.0	108.0	1	FR I	<9.39		M
J0126−0120	3C40	WLRG	0.0180	0.2	316.7	126.7	1	FR I	<4.50		M
J0241−0815*	NGC1052	WLRG	0.0050	0.1	26.5	2.7	15	FR I?	3.0	173	G
J0308+0406	3C78	WLRG	0.0287	0.7	60.0	36.0	3	FR I	<0.73		M
J0319+4130	Perseus A	NLRG	0.0175	3.2	198.3	71.6	16	FR I	2.34	2725	G
J0331+0233	3C88	WLRG	0.0302	0.4	191.3	114.8	1	FR II	<5.06		M
J0429−5349		WLRG	0.0399	?	360.0	280.4	4	FR I	<11.46		M
J0519−4546	PicA	BLRG	0.0351	4.2	450.0	315.0	5	FR II	<2.43		M
J0621−5241	MRC	WLRG	0.0511	0.9	47.7	47.7	1	FR I	<3.60		M
J0918−1205	Hydra A	WLRG	0.0549	9.3	93.7	98.6	17	FR I	42	<100	D
J1006+3453	3C236	WLRG	0.1005	5.4	2363	4324	14	FR II	8.2	162	G
J1145+1936	3C264	WLRG	0.0217	0.2	40.9	17.7	6	FR I	<1.54		G
J1219+0549	NGC4261	WLRG	0.0075	0.06	492.0	74.8	18	FR I	7.2	9	J
J1230+1223	M87	NLRG	0.0044	0.3	744.8	66.3	7	FR I	<1.35		G
J1247+6723		WLRG	0.1073	0.5	618.0	1195	2	FR II	6.73	63	S
J1248−4118*	NGC4696	WLRG	0.0099	0.03	32.0	6.4	8	FR I	<1.57		M
J1254−1233	3C278	WLRG	0.0150	0.13	123.8	37.1	6	FR I	<12.32		M
J1321−4342	NGC5090	WLRG	0.0114	0.06	770.0	154.0	4	FR I	2.70	4	M
J1325−4301	Centaurus A	WLRG	0.0018	0.04	668.6	24.7	19	FR I	2.28	3	G
J1336−3356	IC4296	WLRG	0.0125	0.06	100.9	30.3	1	FR I	<7.43		M
J1352+3126	3C293	NLRG	0.0450	0.9	90.0	78.6	21	FR II	18.0	9	B
J1449+6316*	3C305	NLRG	0.0416	0.4	5.0	4.1	22	FR II	7.40	130	MM
J1516+0701	3C317	WLRG	0.0345	0.3	41.4	28.0	1	FR I	<1.74		G
J1632+8232	NGC6251	WLRG	0.0247	0.2	3150	1547	9	FR I/II	<2.51		G
J1644−7715	MRC	WLRG	0.0427	1.0	124.2	99.4	1	FR II	<8.63		M
J1720−0058	3C353	WLRG	0.0304	3.8	252.9	151.7	1	FR II	42	−100	M
J1806+6949	3C371	WLRG	0.0510	1.3	62.5 (280)	61.4 (275)	10	FR I	<2.90		G
J1952+0230	3C403	NLRG	0.0590	1.9	200.0	220.0	11	FR II	<17.82		M
J1959+4044	Cygnus A	NLRG	0.0561	257.0	127.0	136.5	20	FR II	25.4	151	C
J2157−6941	PKS	BLRG	0.0283	2.0	78.8	47.3	12	FR II	<1.90		M
J2223−0206	3C445	BLRG	0.0562	0.9	570.0	627.0	13	FR II	<8.06		M

Col. 1: source name; col. 2: alternative name; col. 3: optical type; col. 4: redshift; col. 5: 5-GHz luminosity in the rest frame of the source; cols. 6 & 7: largest projected angular (LAS) and linear (LLS) size in arcsec and kpc respectively, as measured from the outermost radio peaks; col. 8: references for the radio structure; col. 9: radio morphology; col. 10: HI column density or a 3σ upper limit to it; col. 11: the shift of the primary HI component relative to the systemic velocity as measured from the optical emission lines, with a negative sign indicating a blue-shift, and column 12: references for the HI observations.

References for the structural information and LLS: 1: Morganti et al. (1993); 2: NVSS; 3: Saikia et al. (1986); 4: Jones & McAdam (1992); 5: Perley et al. (1997); 6: Baum et al. (1988); 7: Owen, Eilek & Kassim (2000); 8: Burgess & Hunstead (2006); 9: Perley et al. (1984); 10: Wrobel & Lind (1990); 11: Dennett-Thorpe et al. (1999); 12: Fosbury et al. (1998); 13: Leahy et al. (1997); 14: Mack et al. (1997); 15: Wrobel & Heeschen (1984); 16: Pedlar et al. (1990); 17: Dwarakanath, Owen & van Gorkom (1995); 18: Condon & Broderick (1988); 19: Condon et al. (1996); 20: Perley, Dreher & Cowan (1984); 21: Beswick et al. (2004); 22: Morganti et al. (2005).

References for HI observations: B:Beswick et al. (2004); M: Morganti et al. (2001); MM:Morganti et al. (2005); G: van Gorkom et al. (1989); D: Dwarakanath, Owen & van Gorkom (1995); J: Jaffe & McNamara (1994); S: Saikia, Gupta & Konar (2007); C: Conway & Blanco (1995).

* J0241−0815 would fall in the category of CFS whereas J1248−4118 and J1449+6316 can be classified as CSS sources.

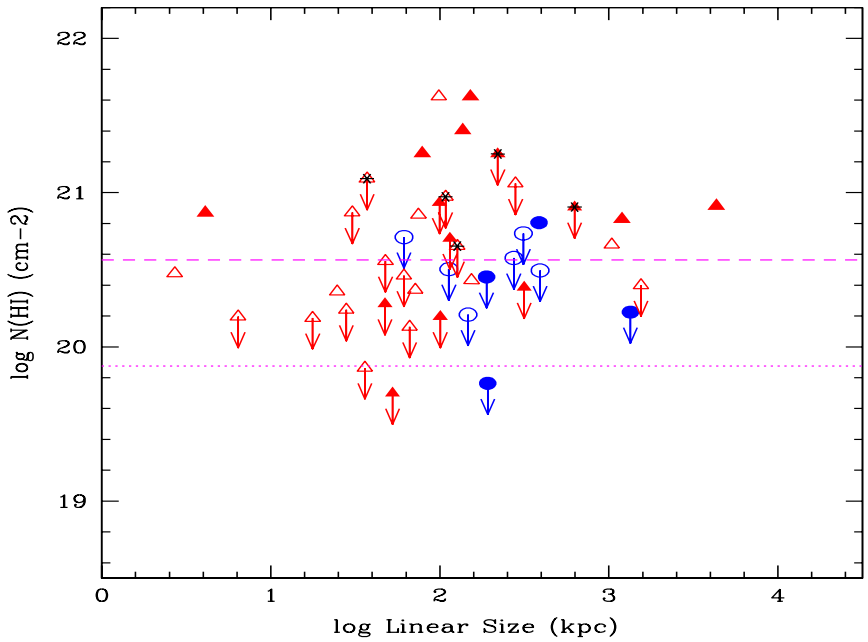

Figure 5.12: HI column density as a function of projected linear source size. Arrows mark the 3σ upper limit to the column density. The blue symbols are sources from our GMRT observations, while red symbols are data from the literature. The open symbols denote FR I radio galaxies while solid symbols represent FR II sources. Dashed and dotted lines correspond to median and minimum value of 21-cm column density detected for the galaxies in our sample of compact radio sources (Table 4.1) to study the dependence of N(HI) on core prominence. Radio galaxies with core flux density lesser than 100 mJy have been further marked as black star.

is detected towards 7 out of 25 (∼30%) objects whereas 7 out of 19 (∼35%) FR II exhibit 21-cm absorption. These compare well with the 21-cm absorption detection rate of ∼35% towards compact radio sources (cf. Section 2.4.2). To a first order this means that galactic environments of the powerful radio sources as probed by 21-cm absorption are similar for compact and larger radio sources. This is interesting as in a recent HI-emission study of a sample of radio sources, Emonts, Morganti & Oosterloo et al. (2007) found that all the sources with $M(HI) \gtrsim 10^9 M_\odot$ have a compact radio source. None of the FR I sources in their sample are found to be associated with these large amounts of gas in HI. It should be noted that detection rate for FR I sources in the 'core sample' could also be as low as 10% if one excludes the detections which were reported individually rather than as part of the searches of sample of radio sources.

The presence of circumnuclear disc is an important component of the unification scheme of FR II radio galaxies. It must be noted for the 'core sample' that 21-cm absorption is not detected towards any of the FR II broad-lined radio galaxies (BLRGs) which are supposed to have jet-axis aligned closer to the line-of-sight than compared to say narrow-lined radio galaxies. This possibility of 21-cm absorption arising from the circumnuclear disks for the FR II radio galaxies is consistent with a number of observational trends. Gupta & Saikia (2006; Chapter 4) for a sample of CSS and GPS sources find the dependence of N(HI) on the degree of core prominence to be consistent with the HI having a disk-like distribution, with the source sizes being larger than the scale size of the disk. Very Long Baseline Interferometry (VLBI)-scale spectroscopic observations towards several sources such as the CSS object J0119+3210 (4C+31.04) and the cores of larger sources such as the well known FR II source Cyg A and the FRI objects NGC 4621 and Hydra A show evidence of absorption arising from a circumnuclear disk-like structure (Conway & Blanco 1995; Taylor 1996; Conway 1999; van Langevelde et al. 2000). In fact, Morganti et al. (2001) have suggested that there may be differences in the torus/disk between FR I and FR II sources, with those in FR Is being geometrically thin.

It is interesting to note that the low-ionization forbidden emission lines in 3C 452 are found to be broader and more red-shifted than the high-ionization ones. The low-ionization lines could then correspond to gas interacting with the jet, thereby being broadened. In that case, a plausible scenario to explain the different 21-cm absorption components is one in which [O III] emission lines represent the systemic velocity and the narrowest 21-cm absorption line component coincident with it, arises from gas in a circumnuclear disk aligned with the dust lane perpendicular to the radio source axis of 3C 452 (de Koff et al. 2000). Thus, if we attribute the narrow component to be due to absorption by a disk, the broader blue-shifted components could still be due to outflowing gas. Amongst the two notable detections of 21-cm absorption towards the cores of extended FR II radio galaxies, namely Cyg A and 3C 353, the system associated with the narrow-line radio galaxy Cyg A has a FWHM of $\sim$270 km s^{-1} and column density of $2.54\times10^{21}(\mathrm{T}_s/100)(1.0/f_c)$ cm^{-2} (Conway & Blanco 1995). The redshift of Cyg A determined from the [O III] emission lines is z_{em}=0.05606 (see Section 4.3 of Tadhunter et al. 2003). The 21-cm absorption line associated with it consists of two components; the narrower (FWHM$\sim$102 km s^{-1}) and weaker one being consistent with the z_{em} while the other one (FWHM$\sim$151 km s^{-1}) is red-shifted with respect to it by $\sim$170 km s^{-1}. In the weak-line radio galaxy 3C 353, the absorption-line (FWHM$\sim$300 km s^{-1}) corresponds to a total HI column density of $4.2\times10^{21}(\mathrm{T}_s/100)(1.0/f_c)$ cm^{-2} (Morganti et

al. 2001). The peak of absorption is blue-shifted with respect to the systemic velocity of the host galaxy estimated from the [O III] and Hα emission lines by $\sim$100 km s^{-1}. Thus 21-cm absorption-line systems detected towards the cores of Cyg A, 3C 353 and 3C 452 have peaks of absorption red-shifted, blue-shifted and consistent with respect to the velocity corresponding to the [O III] emission line. Thus the absorption profiles are often complex suggesting radial motions (i.e infall or outflow) in addition to disks, as has been inferred for the CSS and GPS objects. However, for the 'core sample' majority of 21-cm absorption

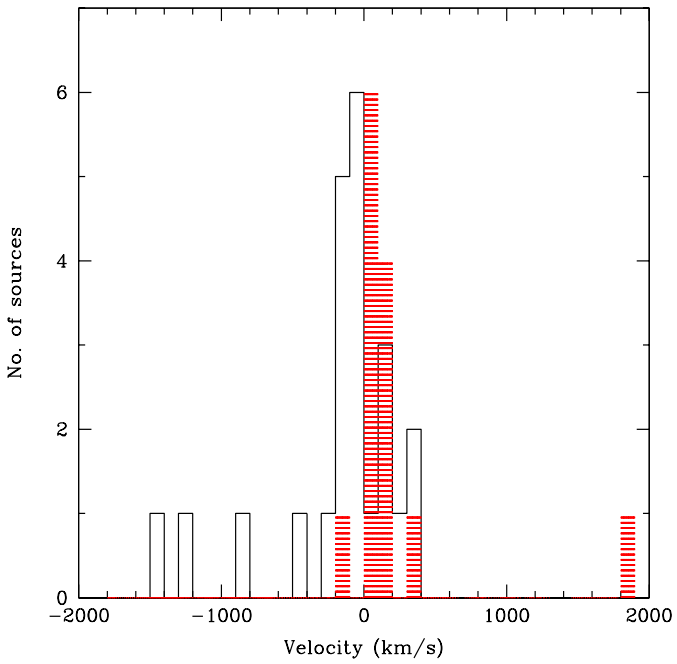

Figure 5.13: The distribution of velocities for the principal HI absorption components with respect to the systemic velocity estimated from optical lines. The solid line is the distribution for CSS sources, while the distribution for absorption lines towards the cores of FR I and FR II radio sources is shown shaded. Absorption line system detected towards Perseus A is placed in the bin at 2000 km s^{-1} instead of the actual value of 2725 km s^{-1}.

systems are either consistent with systemic velocity or redshifted with respect to systemic velocity (Fig. 5.13). The redshifted absorbing material, as noted by van Gorkom et al. (1989) could very well represent the HI clouds falling to the centers of ellipticals. This excess of infalling absorbing material in case of these evolved radio galaxies is in contrast with the case of most compact (i.e. youngest) GPS sources which have an excess of blueshifted absorption lines (cf. Section 2.4.6). This further accentuates the role played by jet-cloud interaction in accelerating the gas clouds in sub-galactic sized radio sources.

5.5 Summary

I have presented the results from a search for 21-cm absorption towards the cores of 10 FR I and FR II radio galaxies. From our search we made 1 new detection i.e. towards the core of radio galaxy J2245+3941 (3C 452) and presented the upper limits on N(HI) for remaining 9 sources. The 21-cm absorption profile detected towards the core of 3C 452 is resolved into three components. The deepest and narrowest of these is consistent with the velocity corresponding to [O III] emission lines. The other two broader components are blue-shifted with respect to it by ∼30 and ∼115 km s^{-1}. If the systemic velocity of the host galaxy is determined from low-ionization forbidden emission lines then both the [O III] emission and 21-cm absorption lines are associated with outflowing material. The 21-cm components are blue-shifted relative to the low-ionization lines by ∼200, 230 and 315 km s^{-1}respectively. The neutral hydrogen column density of the gas is estimated to be N(HI)=$6.39\times10^{20}(T_s/100)(f_c/1.0)^{-1}$ cm^{-2}. If the 21-cm absorber is also responsible for the nuclear absorption seen at x-ray wavelengths, then for a spin temperature of ∼8000 K, the absorber occults only ∼10 per cent of the radio core. This would also be consistent with the nuclear extinction seen at infrared wavelengths.

We combine our results with those of similar 21-cm absorption searches to obtain a larger sample called 'core sample' of 44 radio galaxies. For FR I radio sources in the 'core sample' HI absorption is detected towards 7 out of 25 (∼30%) objects whereas 7 out of 19 (∼30%) FR II exhibit 21-cm absorption. Latter compares well with the 21-cm absorption detection rate of ∼35% towards the compact radio sources (cf. Section 2.4.2). To first order this means that galactic environments of the powerful radio sources as probed by 21-cm absorption are similar for compact (younger) and larger (evolved) radio sources. However, majority of absorption lines in the 'core sample' are either redshifted or consistent with systemic velocity, which could very well represent the infalling material. This is to be contrasted with the case of most compact GPS radio sources where there is an excess of blueshifted absorption lines. This accentuates the role played by jet-cloud interaction in accelerating the gas clouds in these compact radio sources.

Bibliography

[1] Bahcall J.N., Ekers R.D., 1969, ApJ, 157, 1055

[2] Baum S.A., Heckman T., Bridle A., van Breugel W., Miley G., 1988, ApJS, 68, 643

[3] Beswick R.J., Peck A.B., Taylor G.B., Giovannini G., 2004, MNRAS, 352, 49

[4] Black A.R.S., Baum S.A., Leahy J.P., Perley R.A., Riley J.M., Scheuer P.A.G., 1992, MNRAS, 256, 186

[5] Bohlin R.C., Savage B.D., Drake J.F., 1978, ApJ, 224, 132

[6] Burgess A.M., Hunstead R.W., 2006, AJ, 131, 114

[7] Cardelli J.A., Clayton G.C., Mathis J.S., 1989, ApJ, 345, 245

[8] Condon J.J., Broderick J.J., 1988, AJ, 96, 30

[9] Condon J.J., Helou G., Sanders D.B., Soifer B.T., 1996, ApJS, 103, 81

[10] Conway J.E., Blanco P.R., 1995, ApJ, 449, L131

[11] de Bruyn A.G., 1989, A&A, 226, L13

[12] de Koff S. et al., 2000, ApJS, 129, 33

[13] Dennett-Thorpe J., Bridle A.H., Laing R.A., Scheuer P.A.G., 1999, MNRAS, 304, 271

[14] Dickey J.M., Lockman F.J., 1990, ARA&A, 28, 215

[15] Dwarakanath K.S., Owen F.N., van Gorkom J.H., 1995, ApJ, 442, L1

[16] Emonts B., Morganti R., Oosterloo T., 2007, NewAR, 51

[17] Ferrière K.M., 2001, RvMP, 73, 1031

[18] Fosbury R.A.E., Morganti R., Wilson W., Ekers R.D., di Serego A.S., Tadhunter C.N., 1998, MNRAS, 296, 701

[19] Giovannini G., Cotton W.D., Feretti L., Lara L., Venturi T. 2001, ApJ, 552, 508

[20] Gallimore J.F., Baum S.A., O'Dea C.P., Pedlar A., Brinks E., 1999, ApJ, 524, 684

[21] Gupta Neeraj, Salter C.J., Saikia D.J., Ghosh T., Jeyakumar S., 2006, MNRAS, 373, 972

[22] Gupta Neeraj, Saikia D.J., 2006, MNRAS, 370, L80

[23] Hamann F., 1997, ApJS, 109, 279

[24] Isobe N., Tashiro M., Makishima K., Iyomoto N., Suzuki M., Murakami M.M., Mori M., Abe K., 2002, ApJ, 580, L111

[25] Jackson N., Rawlings S., 1997, MNRAS, 286, 241

[26] Jaffe W., McNamara B.R., 1994, ApJ, 434, 110

[27] Jones P.A., McAdam W.B., 1992, ApJS, 80, 137

[28] Kulkarni S.R., Heiles C., 1988, in Galactic and Extragalactic Radio Astronomy, ed. G. Verschuur & K. Kellerman (Heidelberg: Springer), 95

[29] Lawrence C.R., Zucker J.R., Readhead A.C.S., Unwin S.C., Pearson T.J., Xu W., 1996, ApJS, 107, 541

[30] Leahy J.P., Perley R.A., 1991, AJ, 102, 537

[31] Leahy J.P., Black A.R.S., Dennett-Thorpe J., Hardcastle M.J., Komissarov S., Perley R.A., Riley J.M., Scheuer P.A.G., 1997, MNRAS, 291, 20

[32] Mack K.-H., Klein U., O'Dea C.P., Willis A.G., 1997, A&AS, 123, 423

[33] Marchesini D., Capetti A., Celotti A., 2005, A&A, 433, 841

[34] Morganti R., Killeen N.E.B., Tadhunter C.N., 1993, MNRAS, 263, 1023

[35] Morganti R., Oosterloo T.A., Tadhunter C.N., van Moorsel G., Killeen N., Wills K.A., 2001, MNRAS, 323, 331

[36] Morganti R., Tadhunter C.N., Oosterloo T.A., 2005, A&A, 444, L9

[37] Morganti R., Oosterloo T.A., Tadhunter C.N., van Moorsel G., Emonts B., 2005, A&A, 439, 521

[38] Owen F.N., Eilek J.A., Kassim N.E., 2000, ApJ, 543, 611

[39] Pedlar A., Ghataure H.S., Davies R.D., Harrison B.A., Perley R., Crane P.C., Unger S.W., 1990, MNRAS, 246, 477

[40] Perley R.A., Bridle A.H., Willis A.G., 1984, ApJS, 54, 291

[41] Perley R.A., Dreher J.W., Cowan J.J., 1984, ApJ, 285, L35

[42] Perley, R.A., Roser H., Meisenheimer K., 1997, A&A, 328, 12

[43] Saikia, D.J., Subrahmanya C.R., Patnaik A.R., Unger S.W., Cornwell T.J., Graham D.A., Prabhu T.P., 1986, MNRAS, 219, 545

[44] Saikia D.J., Gupta Neeraj, Konar C., 2007, MNRAS, 375, L31

[45] Tadhunter C., Wills K., Morganti R., Oosterloo T., Dickson R., 2001, MNRAS, 327, 227

[46] Tadhunter C., Marconi A., Axon D., Wills K., Robinson T.G., Jackson N., 2003, MNRAS, 342, 861

[47] Taylor G.B., 1996, ApJ, 470, 394

[48] van Gorkom J.H., Knapp G.R., Ekers R.D., Ekers D.D., Laing R.A., Polk K.S., 1989, AJ, 97, 708

[49] van Langevelde H.J., Pihlström Y.M., Conway J.E., Jaffe W., Schilizzi R.T., 2000, A&A, 354, 45

[50] Vermeulen R.C. et al., 2003, A&A, 404, 861

[51] Vermeulen R.C., Labiano A., Barthel P.D., Baum S.A., de Vries W.H., O'Dea C.P., 2006, A&A, 447, 489

[52] Villar-Martín M., Tadhunter C., Morganti R., Axon D., Koekemoer A., 1999, MNRAS, 307, 24

[53] Wrobel J.M., Heeschen D.S., 1984, ApJ, 287, 41

[54] Wrobel J.M., Lind K.R., 1990, ApJ, 348, 135

Chapter 6

Outflowing material in the $z_{\rm em}$= 4.92 BAL QSO SDSS J160501.21−011220.0

6.1 Introduction

Broad absorption line systems (BALs) seen in the spectra of QSOs are characterized by absorption features with large velocity widths ($\Delta v \sim$ a few 1000 km s^{-1}) and, usually, high ionization states (Turnshek et al. 1988; Weymann et al. 1991). The gas giving rise to BALs is believed to be material ejected by the quasar but still located very close to the central regions. Thus studying metallicities in the absorbing gas is a direct probe of the chemical enrichment in the very central regions of AGNs (see Hamann & Ferland 1999 for the review). The associated absorption line systems by and large show large metallicities with a tendency of nitrogen being over-abundant with respect to oxygen and other $\alpha-$ process elements (e.g. Petitjean et al. 1994; Korista et al. 1996; Hamann 1997; Petitjean & Srianand 1999). Detailed studies of emission line properties of $z \geq 4$ QSOs have revealed Super-Solar metallicities in the line emitting gas in broad line regions (BLR), suggesting very rapid star formation process (e.g. Hamann & Ferland 1992; Dietrich et al. 2003). However, no such metallicity estimates at such high redshifts based on absorption lines using echelle spectra are available.

Unlike in the case of most normal galaxies, it is believed that the high metal enrichment usually observed in QSOs has taken place in less than a few 10^8 years through rapid star formation similar to what is expected to happen in the center of ellipticals (Hamann & Fer-

land 1993; Matteucci & Padovani 1993). Thus, studying BAL QSOs at $z_{\rm em} \geq 5$, where the age of the Universe is t$\leq 1.07 \times 10^9$ yr, is important for understanding the star-formation history at a time close to the epoch of reionization and possibly also for constraining cosmological parameters. In the initial list of SDSS QSOs (Fan et al. 2000) there are few QSOs at $z \geq 4$ with associated absorption lines. We obtained a UVES spectrum of the QSO SDSS J160501.21-011220.0, the highest redshift BAL QSO known at that time, with the aim to study the outflowing gas in detail.

In order to derive a realistic estimate of the absorbing gas metallicity one needs to have a good handle on the ionization corrections. Associated systems being close to the QSO are most probably ionized by the QSO light rather than the diffuse intergalactic background. However the ionizing spectrum from the BAL QSOs is poorly known. It is known that BAL QSOs are under-luminous in X-rays (Bregman 1984; Singh et al. 1987; Green & Mathur 1996). Recent, deep Chandra observations have shown that the optical to X-ray spectral index, α_{OX}, measured for BAL QSOs is systematically lower than that of non-BAL QSOs (Green et al. 2001). It is not clear whether this X-ray weakness is due to the QSO being intrinsically X-ray quiet (i.e., this is a property of the central engine) or due to line-of-sight absorption (i.e., radiative transfer effects). Using a complete sample of optically selected QSOs, Brandt et al. (2000) have shown a significant anti-correlation between α_{OX} and the total equivalent width of the C IV absorption lines. In addition it is noticed that the emission line properties of the BAL and non-BAL QSOs are very similar even though the observed X-ray properties differ significantly (Weymann et al. 1991; Korista et al. 1993). Thus, it is most likely that the relative X-ray weakness of BAL QSOs is due to intrinsic absorption.

It must be noted that all existing models of BAL systems assume standard QSO spectrum. However estimated metallicities will be different if the intrinsic α_{OX} is different from that of a typical QSO spectrum. Indeed, Srianand & Petitjean (2000) have shown that the inferred metallicities decrease with decreasing value of α_{OX}. Also, if the absorption is responsible for the suppression of X-rays then it is important to investigate whether it is caused by the gas responsible for the BAL troughs (common absorbers) or by a distinct gas component. It is likely that the common absorber picture is correct for the BAL towards PHL 5200 (Mathur et al. 1995) and that a distinct Compton thick screen is required for the BAL towards PG 0946+301 (Gallagher et al. 1999; Mathur et al. 2000; see also Kraemer et al. 2002).

In this chapter I present a detailed analysis of two well detached BAL outflow com-

ponents that are seen in the spectrum of QSO J160501.21-011220.0 ($z_{em} = 4.92$). Details of the observations are discussed in Sect. 6.2 which is followed by the description of the BALs and column density estimates in Sect. 6.3. In Sect. 6.4 we investigate the physical conditions of the gas. The results are summarised in Sect. 6.5.

6.2 Observations and data reduction

The Ultraviolet and Visible Echelle Spectrograph (UVES; Dekker et al. 2000), installed at the ESO VLT 8.2 m telescope, unit Kueyen, on Mount Paranal in Chile, was used on June 15-17, 2001, to obtain high resolution spectra of QSO J 160501.21−011220.0. A non-standard setting with cross-disperser #4 and central wavelength 8420 Å was used in the Red arm of UVES. Full wavelength coverage was obtained this way from 6514 to 8300 Å and from 8494 to 9300 Å accounting for the gap between the two Red-arm CCDs. The CCD pixels were binned 2×3 (namely, twice in the spatial direction and three times in the dispersion direction) and the slit width was either fixed to $1''.2$ or $1''.5$, yielding an overall spectral resolution $R \sim 30000$. The total integration time 3h30min was split into 3 exposures. The data were reduced in the dedicated context of MIDAS [1], the ESO data reduction system, using the UVES pipeline (Ballester et al. 2000) in an interactive mode. The main characteristics of the pipeline is to perform a precise inter-order background subtraction for science frames and master flat-fields, and an optimal extraction of the object signal rejecting a number of cosmic ray impacts and subtracting the sky spectrum simultaneously. The pipeline products are checked step by step. The wavelength scale of the spectra reduced by the pipeline was then converted to vacuum-heliocentric values and individual 1-D exposures scaled, weighted and combined altogether using the NOAO *onedspec* package of the IRAF[2] software. During this process, the spectra were rebinned to 0.08 Å pix^{-1}. In order to increase the signal-to-noise ratio in this near-IR part of the optical range (and as the lines of interest are broad), we applied a Gaussian filter smoothing with two pixel FWHM and get an effective spectral resolution of ~ 12 km s^{-1}. The resulting signal-to-noise ratio per pixel is of the order of 20 or more over most of the wavelength range considered here. The final spectrum is shown in Fig. 6.1.

The continuum fitting in the red side of the Lyα emission has been performed using a

[1] MIDAS: Munich Image Data Analysis System, trademark of the European Southern Observatory (ESO)

[2] IRAF: The Image Reduction and Analysis Facility is distributed by the National Optical Astronomy Observatories, which is operated by the Association of Universities for Research in astronomy, Inc. (AURA), under cooperative agreement with the National Science Foundation.

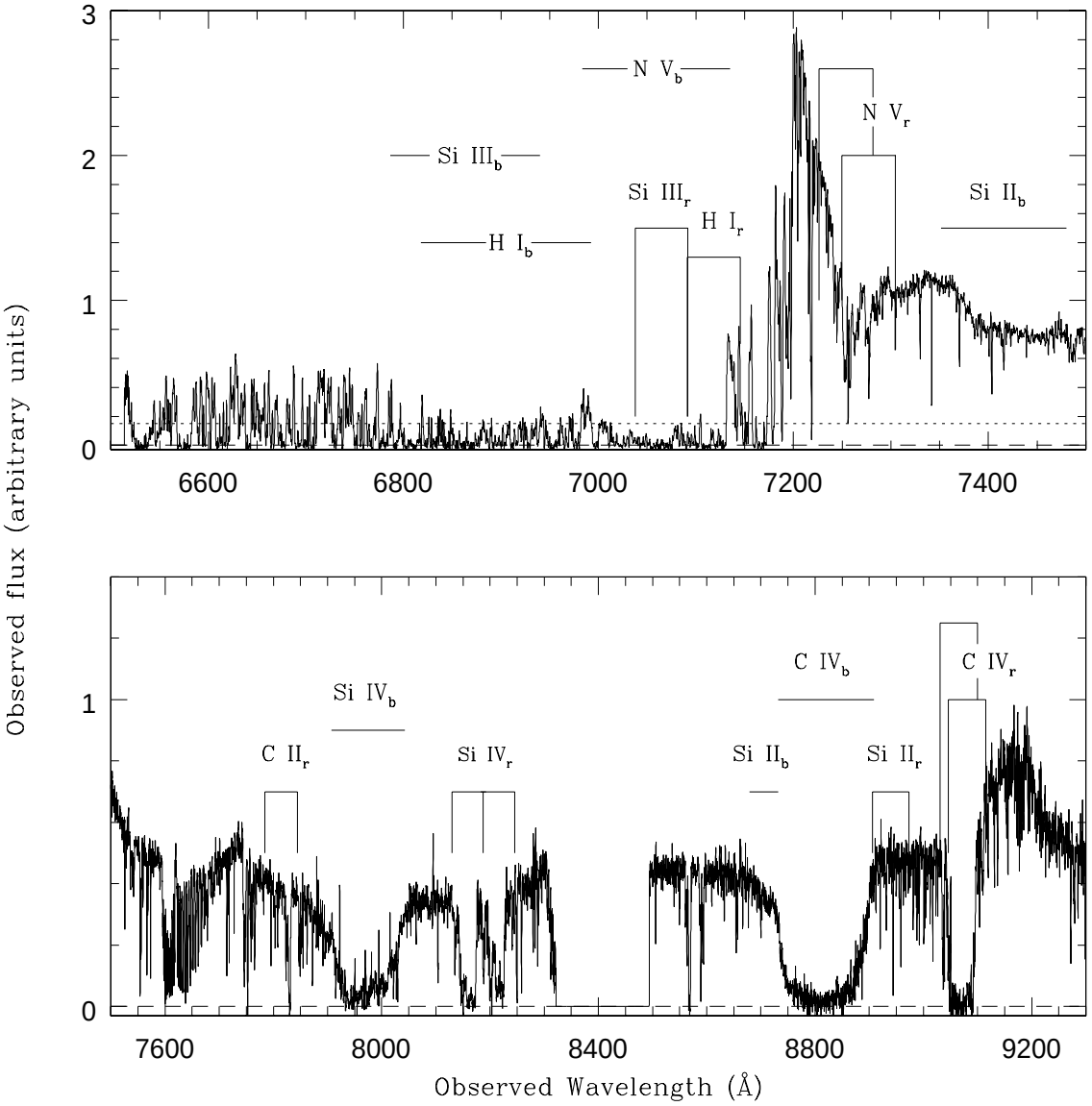

Figure 6.1: UVES spectrum of the $z_{\rm em}$= 4.92 QSO SDSS J160501.21-011220. Two well detached BAL features are seen covering the redshift ranges 4.62−4.75 and 4.83−4.88. We denote them as blue and red systems respectively. The expected positions of different lines (with sub-scripts r and b denoting red and blue respectively) are marked with solid lines. The horizontal dotted line in the top panel gives the mean transmitted flux computed over the Lyα forest in the wavelength range 6550−6800 Å that is not affected by the BAL absorption lines.

smooth low order polynomial considering only the absorption free regions. In the Lyman-α forest, we approximated the QSO spectrum by a powerlaw, $f_\nu \propto \nu^{-0.6}$, that we fitted on the low-dispersion SDSS spectrum made available to us by Dr. Fan. The normalization of the power-law was done using the flux in the region between the C IV and Si IV emission lines. In our normalised spectrum the mean Lyα transmission flux in the redshift range z=4.39 to z=4.60 (that is not contaminated by any BAL absorption lines) is 0.15. This is consistent with the values derived in the same redshift range using non-BAL QSOs (Becker et al. 2001).

6.3 Broad absorption line systems

Based on the unabsorbed C IV emission line we estimate the emission redshift of the QSO to be $z_{\rm em}$=4.92. Two well detached absorption line systems are identified based on the C IV and Si IV absorptions over the redshift ranges, $z_{\rm abs}$=4.83−4.88 and $z_{\rm abs}$ = 4.62−4.75, respectively. For mean redshifts $z_{\rm abs}$ = 4.855 and 4.685, this corresponds to ejection velocities of ≈3,330 km s^{-1}and ≈ 12,160 km s^{-1}. The spectrum in the Lyman-α forest is heavily affected by the high Lyα opacity of the intergalactic medium. Even though excess absorption is seen at the expected positions of BAL absorption lines (see Fig. 6.1) it is difficult to estimate column densities in this region. Therefore, in the following sections we use only lines observed on the red side of the Lyα emission line to investigate the physical conditions in the outflowing gas.

6.3.1 The red component at $z_{\rm abs}$ = 4.855

The absorption trough in this component is ∼ 2000 km s^{-1} wide. The absorption profiles of different transitions centered at z_{abs} = 4.855 are shown in Fig. 6.2. The absorption profile of the Si IV doublet that is comparatively less saturated than that of the C IV doublet suggests the presence of 2 relatively narrow components denoted by l1 and l2 and 3 broad subcomponents denoted by a, b and c. While Lyα and C IV are detected in all these components, N V absorption is detected only in the broad subcomponents (see Fig. 6.2).

All the obviously saturated absorption lines have zero residual (C IV and Lyman-α, see Fig. 6.2). The covering factor of the gas is therefore unity. In case of complete coverage the observed residual intensities R_1 and R_2 in the first and second member of the doublet are related as R_1=R_2^2 (see Srianand and Shankarnaraynan 1999). Indeed, even though part of the N V absorption line is contaminated by atmospheric absorption (see Fig. 6.3), the

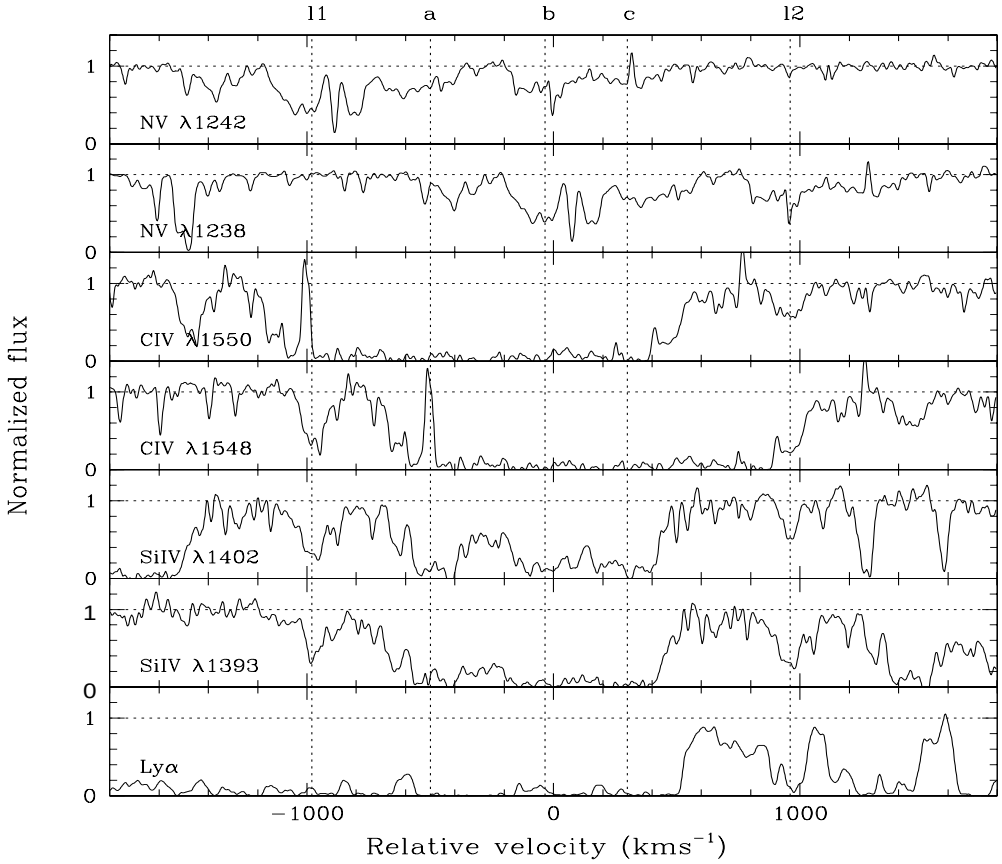

Figure 6.2: Velocity plots of the red absorption line system centered at $z_{\rm abs} = 4.855$. We identify 5 distinct components based on the Si IV and C IV profiles (marked with vertical dotted lines). Detection of Lyα line in this system is unambiguous as the profile just follows the well detached Si IV absorption line at least from 0 to 600 km s^{-1}.

velocity ranges in the profiles that are free of blending are consistent with complete coverage (see top panel in Fig. 6.3). As emission in this wavelength range is contributed by both continuum and broad emission lines the corresponding absorbing gas has to be located outside the broad line region (BLR). As the N V lines are weak we can derive the N V column densities. However, due to saturation effects, we can determine only lower limits for C IV and H I column densities. It can be seen on Fig. 6.2 that Si IVλ1402 is only partly saturated which means that, although very uncertain, we can estimate the corresponding column density. We use also the Si IVλ1402 profile as a template to determine upper limits on the column densities of non detected species (see below). The column density in each

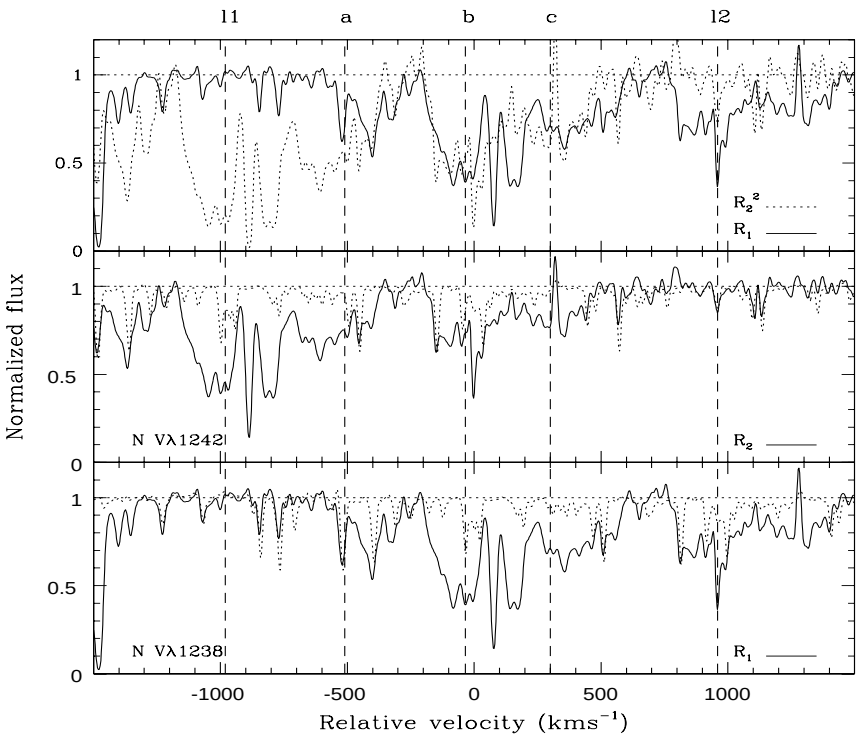

Figure 6.3: Velocity plots of N v doublets centered at $z_{\rm abs} = 4.855$. R_1 and R_2 are the residual intensities in the first and second lines of the doublet.Vertical dotted lines show the subcomponents l1, a, b, c and l2 respectively. In the lower two panels the dotted profiles give the atmospheric lines seen toward QSO 1122−1628. In the top panel we overplot the two N v profiles after appropriately scaling (see text) the N vλ1242 assuming complete coverage. The good matching of profiles suggests that N v absorption line covers the background source completely.

velocity pixel was obtained using the relation

$$N(v) = 3.768 \times 10^{+14}\ \tau/f\lambda\ \mathrm{cm}^{-2}\ \mathrm{km}^{-1}\mathrm{s} \tag{6.1}$$

where, τ, f and λ are the optical depth, oscillator strength and rest wavelength respectively. The total column density is obtained by integrating $N(v)$ over the velocity range -1120 to 1160 km s^{-1}. The results are presented in Table 6.1. Rest wavelengths and oscillator strengths used here are taken from Verner et al. (1994). The two lines of the C iv doublet are blended and we use an effective oscillator strength, $f = f_1 + f_2$, and mean wavelength, $(\lambda_1 + \lambda_2)/2$, to compute the lower limit on the column density. In the case of N v, we use the N vλ1238 line for component a and N vλ1242 line for components b and c that are free of blending. Contamination by atmospheric features (see Fig. 6.3) is corrected by carefully

Table 6.1: Column densities estimated using apparent optical depth method with complete coverage.

$z_{\rm abs}$	species	logN ($\rm cm^{-2}$)
4.855	H I	$\geq$15.67
	C II	$\leq$14.21
	C IV	$\geq$15.64
	Si II	$\leq$14.13
	Si IV	15.33:
	N V	14.63−14.71
4.685	H I	$\leq$ 16.00
	C IV	$\geq$15.94
	Si II	$\leq$14.73
	Si IV	$\geq$15.40

masking the atmospheric contamination using the normalised spectrum of Q 1122−1628. Singly ionized species such as Si II, C II and Al II are absent and the spectrum at the expected position of Al III lines is unfortunately very noisy. As said above, we evaluate upper limits for column densities of the latter species using the Si IVλ1402 profile (which is not completely saturated and least affected by atmospheric contamination) extending from −1120 to 1160 km $\rm s^{-1}$ as a template. The scaling factor $k = [Nf\lambda]_{X^+}/[Nf\lambda]_{template}$ between the two optical depths $\tau_{template}$ and τ_{X^+} for species X^+ is then obtained by minimizing

$$\alpha = \Sigma(\tau_{\rm X^+} - k * \tau_{template})^2 \tag{6.2}$$

For Si II and C II, k comes out to be 0.031 and 0.035 respectively. The corresponding upper limits on the column densities are given in Table 6.1. Note that the error in the column density of N V is mainly due to continuum placement uncertainties. We note that most of the atmospheric absorption seen in the expected wavelength range have consistent equivalent width. This suggests that our continuum fitting does not underpredict the absorption in the N V region. No flux is detected at the expected position of Si IIIλ1206 (see Fig. 6.1). However, we could not use this to derive a lower limit on Si III as the same region is contaminated by a probable N V absorption line from the blue component (see Fig. 6.5).

Finally we notice that the velocity separation between the two narrow components l1 and l2 of the red component is very close to the Si IV doublet splitting. This is shown

in Fig. 6.4. This is consistent with growing evidence for line-locked flows and radiative acceleration in BAL systems (see Srianand et al. 2002 and references therein).

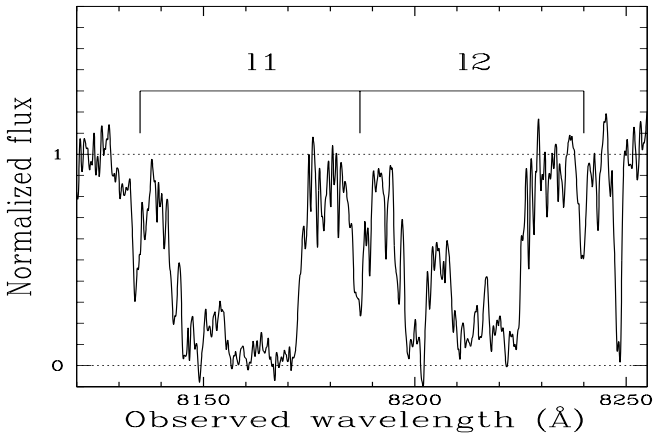

Figure 6.4: Region of the spectrum containing the Si IV trough of the red BAL component at $z_{\rm abs} \sim 4.855$. Note that systems l1 and l2 have a velocity separation equal to that of the Si IV doublet splitting suggesting the presence of line-locking in the system.

6.3.2 The blue component at $z_{\rm abs} = 4.685$

The absorption profiles of different transitions centered at $z_{abs} = 4.685$ are shown in Fig. 6.5. Doublet partners for C IV and Si IV are partially blended together. The non-zero residual flux for the blended C IV$\lambda\lambda$1548,1550 corresponds to a covering factor, $f_{\rm c} \geq$0.90. It is interesting to note that the absorption is well detached from the emission line profile. Thus the partial coverage reflects either $\simeq 10\%$ contribution from the scattered light or partial coverage of the continuum source. Lower limits to column densities for the Si IV$\lambda\lambda$1393,1402 and C IV$\lambda\lambda$1548,1550 were obtained assuming full coverage (see Table 6.1). Doing otherwise would only increase these limits. Note that C IV absorption line extends over a larger velocity range as compared to Si IV absorption profile (see Fig. 6.5). Like in the red component, singly ionized species Si II and C II are not detected which indicates that the neutral hydrogen column density cannot be large (remember that metallicity in this kind of gas is usually large). N V may be present but its redshifted position in the Lyα forest overlaps with that of H I and Si III from the red component (see Fig. 6.1). The mean transmitted flux at the N V position is consistent with saturated absorption line. In the Fig. 6.5 the intervening Lyman-α forest is clearly observed over the whole range corresponding to the BAL H I Lyman-α trough. This means that the H I optical depth cannot be large except if

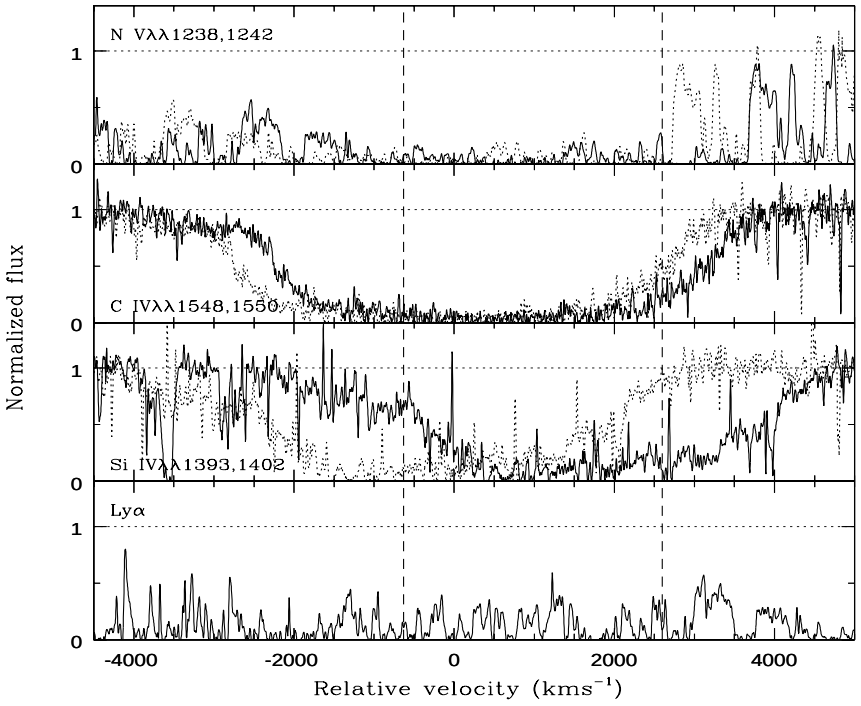

Figure 6.5: Velocity plots for the blue component centered at $z_{\rm abs}$= 4.685. Second member of the doublets is overlaid as a dotted line. Vertical dashed lines mark the velocity range over which Si IV absorption line is seen. Note that C IV absorption is seen over a larger velocity range. The non-zero residual flux at the expected position of Lyα absorption is used for obtaining the upper limit on the H I column density.

the covering factor of H I is much smaller than that of C IV. This is not impossible (see e.g. Srianand et al. 2002) but would be surprising given the non detection of both C II and Si II. By comparing the mean transmission in this region with that devoid of BAL absorption lines we estimate that $\tau(v)$ for H I is less than 2. If we use the velocity range covered by the C IV profile ($\simeq$ 4000 km s^{-1}), we see that the H I column density can not much larger than 10^{16} cm^{-2}.

6.4 Discussion

6.4.1 Physical conditions in the outflowing gas

From the discussion in the previous Section, it is clear that constraints are not strong enough to probe the physical conditions in the blue component ($z_{\rm abs}$ = 4.685). We therefore mainly concentrate on the red component ($z_{\rm abs}$ = 4.855). Recent Chandra observations (Vignali

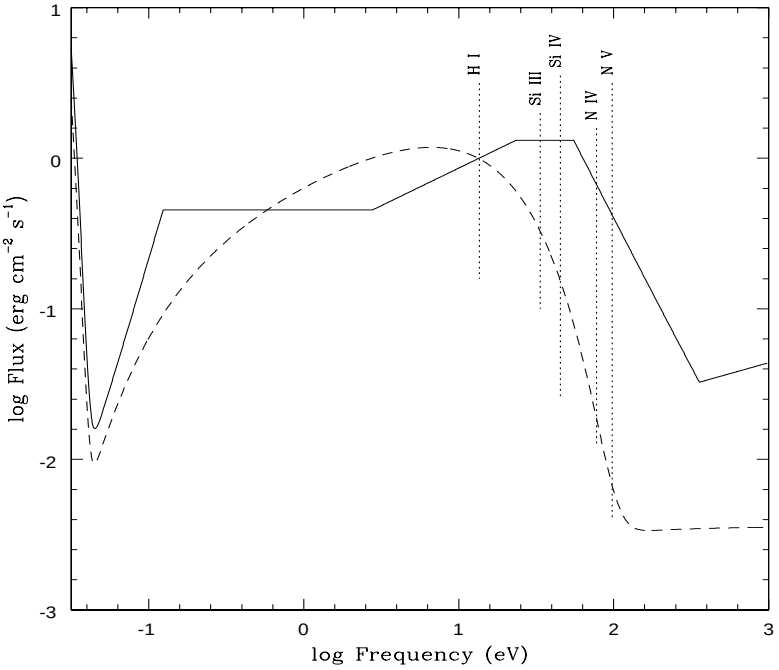

Figure 6.6: The spectral energy distribution (SED) of the ionizing radiation. The continuous and dashed curves correspond to the SED of the MF and BAL spectrum respectively. The vertical dotted lines give the ionization potential of the different species we are interested in this study.

et al. 2001) fail to detect X-rays from the QSO SDSS J160501.21-011220.0. As discussed before, the X-ray non-detection could be either due to large X-ray absorbing column density or a consequence of the QSO being intrinsically X-ray quiet. Indeed, there are already some reports that the X-ray continuum shapes of QSOs may evolve at $z \geq 2.5$ (e.g. Vignali et al. 1999; Blair et al. 2000; Vignali et al. 2003). Assuming that the lack of X-rays in this source is due to absorption, Vignali et al. (2001) infer that the X-ray non-detection for this object implies a total hydrogen column density of N(H(total)) $\geq 5.0 \times 10^{23}$ cm^{-2}, characteristic of low-ionization BAL QSOs at low redshift. Note that the limit on the X-ray flux further implies a small optical to X-ray spectral index, $\alpha_{\rm ox} < -1.82$, for this object.

The absence of singly ionized species C II and Si II suggests that H I is optically thin at the Lyman limit. Thus, to probe the physical conditions in the red component, we run grids of photoionization models using Cloudy (Ferland 1996) in the range log N (H I) (cm^{-2})$\sim 10^{16}$ to 10^{17} cm^{-2}, considering the gas being ionized by either an unattenuated QSO spectrum given by Mathews & Ferland (1987) (hereafter MF spectrum; see Fig. 6.6) or a modified

Table 6.2: Chemical compositions considered in the models:

	Solar	Starburst*		
Metal	1.0 $Z_\odot$	1.0 Z_{SB}	0.5 Z_{SB}	0.20 Z_{SB}
C	-3.44	-3.90	-4.22	-4.63
N	-4.03	-4.60	-5.34	-6.51
O	-3.13	-3.00	-3.30	-3.70
Si	-4.44	-4.43	-4.74	-5.14

* This form of Starburst abundances correspond to chemical evolution model M5a of Hamann & Ferland (1993).

spectrum with little X-rays (hereafter BAL spectrum; see Fig. 6.6) mimicking attenuation of a typical QSO spectrum by a large column density of ionized gas (see below). The models are run for different chemical composition, either the Solar one or the so-called Starburst one (see Table 6.2). In all the models, the calculations are stopped when the total neutral hydrogen column density reaches the limit we set (log N(H I) (cm^{-2}) = 16 or 17).

The input parameters of the models, that reproduce the observed ratios as well as the column densities of individual species, are given in Table 6.3. The corresponding total hydrogen column density in the allowed range of ionization parameters is given in the last Column of the Table 6.3. Results for some selected models with different ionizing spectra and chemical composition for log N(H I) (cm^{-2})) = 17 are given in Fig. 6.7. In this figure we have plotted the column density of different species as a function of ionization parameter. The horizontal dotted lines mark limits on the observed column densities of Si II , Si IV , C II and C IV . The minimum and maximum of the allowed range for log U are marked with verticle dashed lines. The former is obtained using either of the ratios N(Si II)/N(Si IV) or N(C II)/N(C IV) and the latter is obtained from the observed N(N V)/N(Si IV) ratio for metallicities assumed in the model. The range of ionization parameters for which the observed N V column density is reproduced is indicated as a verticle shaded region.

We note that, if the H I column density is close to the observed value (i.e. few 10^{16} cm^{-2}) one needs overall metallicities larger than Solar to explain the observed column densities. We therefore mainly concentrate on models with N(H I)= 10^{17} cm^{-2} that will give a conservative lower limit on the metal enrichment in the system.

If the gas is ionized by a MF type spectrum and has a Solar composition, it can be seen from panel (a) in Fig. 6.7 that the observed constraints on the ion ratios and the N V and

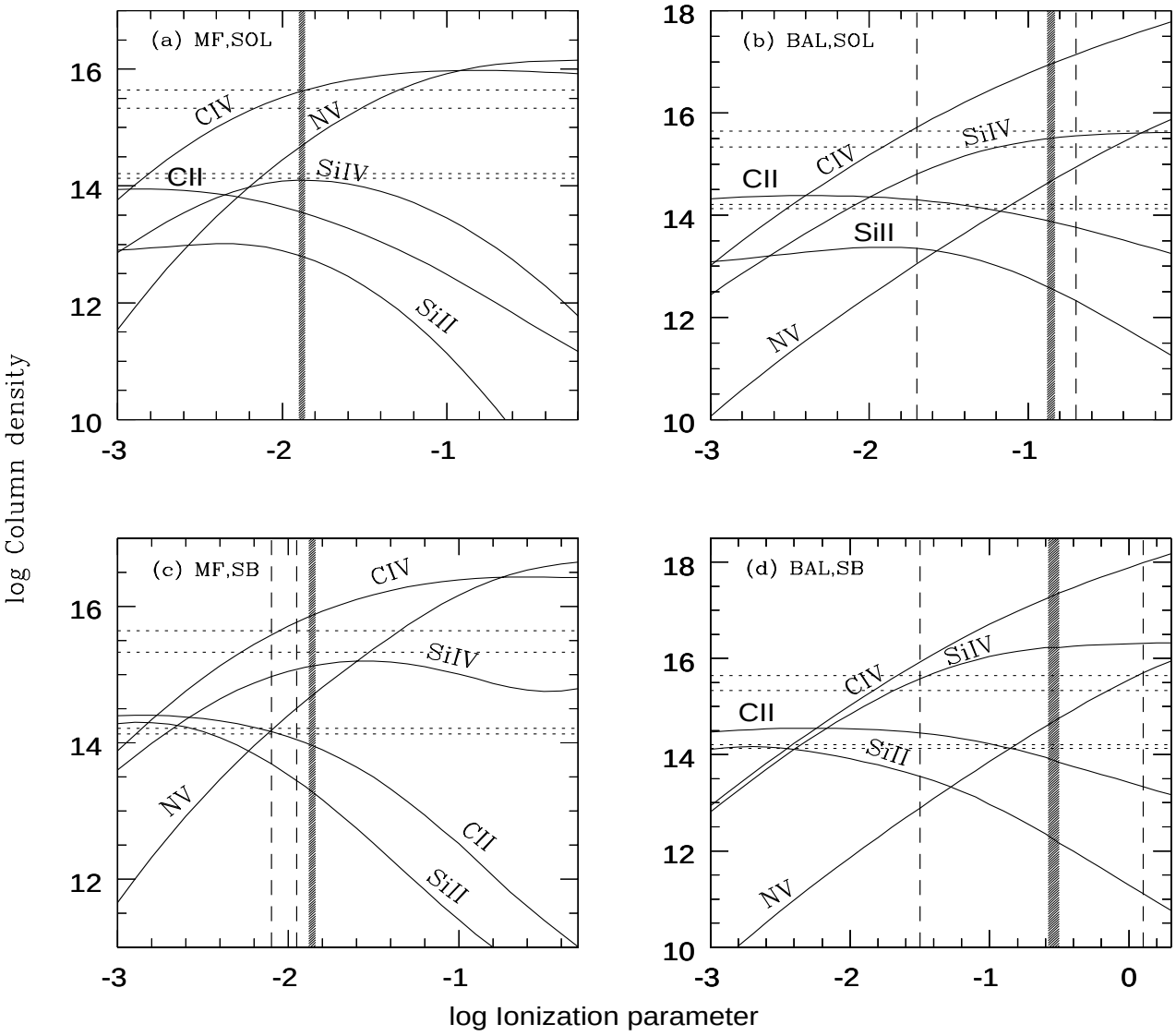

Figure 6.7: Predicted column densities of different species as a function of ionization parameter for log N(H I) (cm^{-2}) = 17. Results given in panels (a) and (b) are obtained for the MF and BAL spectrum with metallicity 0.1 $Z_\odot$ and 0.5 $Z_\odot$ respectively. The results for MF and BAL ionizing spectrum with metallicity 0.1 Z_{SB} of the Starburst enrichment (see Table 6.2) are given in panels (c) and (d) respectively. In each panel the horizontal dotted lines (from bottom to top) mark the limits on the column density of Si II , C II , Si IV and C IV obtained from our observations. While the former two are lower limits the latter two are upper limits. The verticle dashed lines give the limits on the ionization parameters based on the X II/X IV ratios and the observed ratios of N V and Si IV . The verticle shaded region gives the ionization parameter range over which the observed column density of N V is reproduced for the chosen nitrogen metallicity.

Table 6.3: Summary of the photoionization models considered for the red component.

Model parameters				**allowed range in log U from**		**log(N(H(total)))***
Spectrum	enrichment	Metallicity(Z)	log N(H I)*	ratios	observed N	
MF	Solar	$0.5Z_{\odot}$, [Si/N]=3.0[Si/N]$_{\odot}$	17.00	(-2.25,-2.15)	≈-2.2,-2.1	(19.99,20.11)
BAL	”	$1.0Z_{\odot}$	16.00	(-1.5,-1.1)	≈-1.1	20.00
”	”	$1.5Z_{\odot}$	”	(-1.4,-0.95)	≈-1.0	19.90
”	”	$0.05_{\odot}$	17.00	(-1.7,-0.75)	≈-0.7	21.42
”	”	$0.1Z_{\odot}$	”	(-1.7,-0.7)	(-0.9,-0.8)	(21.53,21.62)
”	”	$0.2Z_{\odot}$	”	(-1.65,-0.65)	≈-1.0	21.36
”	”	$1.0Z_{\odot}$	”	(-1.4,-0.4)	–	–
”	Starburst	$1.0Z_{SB}$	16.00	(-1.4,-0.65)	≈-0.7	20.30
”	”	$5.0Z_{SB}$	”	(-1.4,-0.7)	≈(-1.0,-0.9)	(19.32,19.41)
”	”	$9.0Z_{SB}$	”	(-1.15,-0.8)	≈-1.05	19.11
”	”	$0.2Z_{SB}$	17.00	(-1.7,FP)	≈0.1	22.42
”	”	$0.5Z_{SB}$	”	(-1.5,0.1)	≈(-0.6,-0.5)	(21.60,21.70)
”	”	$1.0Z_{SB}$	”	(-1.3,0.1)	≈-0.8	21.12

* in cm^{-2}

C IV column densities can be consistently reproduced for log U $\simeq -1.9$ (see the shaded region). However the predicted column density of Si IV is lower than the observed value by more than an order of magnitude. It is clear that the observed value can be reproduced only if [Si/H]≥[Si/H]$_{\odot}$. Increasing the overall abundance actually reduces the required overabundance of Si with respect to N. For example if one assumes Z = 0.5 $Z_{\odot}$ the observed column densities can be reproduced consistently with lower ionization parameter and a [Si/N] ratio higher than Solar by a factor of 3 only (see Table. 6.3). Larger metallicities are not possible however as C II would then be detectable.

The enhancement of N(Si IV) with respect to N(N V) can be achieved by either enhancing the silicon metallicity with respect to the nitrogen one as discussed above or by suppressing the N IV ionizing photons. The first possibility can be achieved in a chemical enrichment model where the secondary production of N has not yet begun to dominate. The latter possibility naturally arise if the cloud sees an attenuated X-ray spectrum, similar to what we observe directly for SDSS J160501.21−011220.0. We explore this possibility in the following.

We model the absorbed spectrum (called BAL spectrum in the following) as the compos-

ite of a black body spectrum with temperature T = 150,000 K, plus a power-law spectrum with $\alpha_{uv} = 0.5$ and $\alpha_x = 1.0$ and a relative scaling $\alpha_{ox} = 2.0$ (see Ferland 1996). From Fig. 6.6, it is clear that for a given number of hydrogen ionizing photons this spectrum has less photons to ionize Si III and N IV compared to the MF spectrum. Thus a given ionization state will be produced by higher values of log U and hence higher total hydrogen column densities. However the major difference is the presence of a soft X-ray excess in the MF spectrum that implies more N IV ionizing photons for a given number of Si III ionizing photons compared to the BAL spectrum. For a column density of log N (H I) (cm^{-2})≈17.00, observations can be reproduced by models with metallicities $0.05Z_{\odot} \leq Z \leq 0.2Z_{\odot}$ (Table 6.3). This is also demonstrated in panel (b) of Fig. 6.7. As expected, in these models the results are consistent with observations at an ionization parameter an order of magnitude higher than that required for the MF ionizing spectrum. Thus, we can reproduce the observed column densities with Sub-Solar metallicity and Solar abundance ratios.

It is usual in the case of the BLR clouds to explain an enhanced nitrogen abundance by rapid star formation nucleosynthesis. We consider such a chemical enrichment in our models using option "starburst abundances" in Cloudy (see Table 6.2). The details of the models are given in Hamann & Ferland (1993). These models have problems in reproducing the observations when a MF ionizing spectrum is considered (see panel (c) in Fig. 6.7). However, the observed ratios are reproduced if the BAL spectrum is used instead (see Table 6.3 and panel (d) in Fig. 6.7) for overall metallicity ≥ 0.2 and log N(H I) (cm^{-2}) in the range 16 to 17.

It is interesting to note that for all the models considered here the total hydrogen column density is at least an order of magnitude less than the amount required (i.e. N(H(total)) $\geq 5 \times 10^{23}$ cm^{-2}) to explain the lack of X-rays in this QSO by absorption of a standard QSO spectrum (Table 6.3). We also run models by fixing the total hydrogen column density to be N(H(total)) $\geq 5 \times 10^{23}$ cm^{-2}. For MF ionizing spectrum we do not find any model that can reproduce the constraints noted in Table 6.1. Thus, we can conclude that either SDSS J160501.21−011220.0 is intrinsically X-ray weak or, if there is any Compton thick screen between the quasar and us, it has nothing to do with the gas that is associated with the red component.

The similar characteristics of the blue component together with the low N(H I) column density of the system strongly suggests that the blue component as well is not Compton thick.

6.4.2 Formation redshift of the blackhole

We estimate the mass of the black hole from the Eddington accretion. For this we estimate the rest frame luminosity at 2500 Å using the low dispersion spectra obtained by the SDSS group (Fan et al. 2000) to be L_ν=1.37×10^{31} erg s^{-1} Hz^{-1}. Applying bolometric correction as suggested by Elvis et al. (1994), we obtain a bolometric luminosity of L_{bol}=9.21×10^{46} erg s^{-1}. Assuming Eddington accretion we derive the black hole mass, $M_{\rm BH}$ = 7.1×10$^8\eta^{-1}$ M$_\odot$ (see Haiman & Loeb 2001). Here, η is the efficiency parameter (i.e. accretion luminosity given in the units of Eddington luminosity). If ϵ=$L_{bol}/\dot{M}_{BH}c^2$ is the radiative efficiency for a mass accretion rate $\dot{M}_{BH}$ then the natural e-folding time scale for the growth of a single seed can be written as

$$t = M_{BH}/\dot{M}_{BH} = 4.0 \times 10^7 \epsilon_{0.1}\eta^{-1} yr \tag{6.3}$$

It will therefore take about ln(7.1×10$^8\eta^{-1}$M$_\odot$/10 M$_\odot$) = 18.1 e-folding times (or t $\geq$ 0.7$\epsilon_{0.1}\eta^{-1}$ Gyr) for the black hole to grow to the above estimated mass from a stellar-mass seed of 10 M$_\odot$. For the assumed value of ϵ $\approx$ 0.1 and $\eta \approx 1.0$ this corresponds to a formation epoch of the black hole close to $z \approx 11$ for the cosmological model considered here.

6.5 Summary

I have presented the analysis of broad absorption lines (BALs) seen in the spectrum of the $z_{\rm em}\simeq$4.92 QSO SDSS J160501.21-011220.0. Our high spectral resolution UVES spectrum shows two well detached absorption line systems at $z_{\rm abs}$= 4.685 and 4.855. The system at $z_{\rm abs}$= 4.855 covers the background source completely suggesting that the gas is located outside the broad emission line region. On the contrary the system at $z_{\rm abs}$= 4.685, which is redshifted on top of the quasar continuum, has a covering factor of the order of 0.9. Physical conditions are investigated in the BAL system at $z_{\rm abs}$= 4.855 using detailed photoionization models. The observed H I column density and the limits on C II and Si II absorptions suggest that log N(H I) (cm^{-2}) is in the range 16–17. The observed column densities of N V , Si IV and C IV in the $z_{\rm abs}$= 4.855 component require, unlike what is derived when analysing broad emission lines, that nitrogen is underabundant by more than a factor of 3 compared to silicon if the gas is photoionized by a typical QSO spectrum. Thus, if the gas is ionized by a standard MF spectrum, the chemical enrichment of the cloud is different from that required by emission line clouds. We show however that the relative supression in

the N v column densities can be reproduced for Solar abundance ratios or abundance ratios typical of rapid Starburst nucleosynthesis if we use an ionizing spectrum that is devoid of X-rays. Thus if the composition of BAL is like that of the emission line regions it is most likely that the cloud sees an ionizing spectrum similar to what we observe from this QSO that is strongly attenuated in the X-rays. This is consistent with the fact that none of our models have high enough Compton optical depth to be able to remove X-rays from the QSO. Similar arguments lead to the conclusion that the system at $z_{\rm abs}$= 4.685 as well is not Compton thick.

Using simple Eddington arguments we show that the mass of the central black hole is $\sim 8 \times 10^8$ $M_\odot$. This suggests that the accretion onto a seed black hole must have started as early as $z \sim 11$. This gives a typical formation epoch for the host galaxy of the QSO.

Bibliography

[1] Ballester P., Modigliani A., Boitquin O. et al., 2000, The Messenger, 101, 31

[2] Becker R. et al., 2001, AJ, 122, 2850

[3] Blair A.J., Stewart G.C., Georgantopoulous I., Boyle B.J., Griffiths R.E., Shanks T & Almaini O., 2000, MNRAS, 314,138

[4] Brandt W.N., Laor A., Wills B.J., 2000, ApJ, 528, 637

[5] Bregman J.N., 1984, ApJ, 276, 423

[6] Dekker H. et al., 2000, SPIE, 4008, 534

[7] Dietrich M. et al., 2003, A&A, 398, 891

[8] Elvis M. et al., 1994, ApJS, 95, 1

[9] Fan X. et al., 2000, AJ, 119, 1

[10] Ferland G. J., 1996, HAZY- a brief introduction to CLOUDY 90, University of Kentucky Physics Department Internal Report

[11] Gallagher S., Brandt W.N., Sambruna R., Mathur S., Yamamski N., 1999, ApJ, 519, 549.

[12] Green P.J., Aldcroft T.L., Mathur S., Wilkes B.J., Elvis M., 2001, ApJ, 558, 109

[13] Green P.J., Mathur S., 1996, ApJ, 462, 637

[14] Haiman Z., Loeb A., 2001, ApJ, 552, 459

[15] Hamann F., 1997, ApJS, 109, 279

[16] Hamann F., Ferland G.J., 1992, ApJ, 391L, 53

[17] Hamann F., Ferland G.J., 1993, ApJ, 418, 11

[18] Hamann F., Ferland G.J., 1999, ARA&A, 37, 487

[19] Korista K. et al., 1993, ApJ, 413, 445

[20] Korista K. et al., 1996, ApJ, 461, 641

[21] Kraemer S.B., Crenshaw D.M., Yaqoob T. et al., 2002, astro-ph/0208478

[22] Mathews W.G., Ferland G.J., 1987, ApJ, 323, 456

[23] Mathur S., Elvis M., Singh K.P., 1995, ApJ, 455, 9

[24] Mathur S. et al., 2000, ApJ, 533, 79

[25] Matteucci F., Padovani P., 1993, ApJ, 419, 485

[26] Petitjean P., Rauch M., Carswell R.F., 1994, A&A, 291, 29

[27] Petitjean P., Srianand R., 1999, A&A, 345, 73

[28] Singh K.P., Westergaard N.J., Schnopper H.W., 1987, A&A, 172, 11

[29] Srianand R., Petitjean P., 2000, A&A, 357, 414

[30] Srianand R., Petitjean P., Ledoux C., Hazard C., 2002, MNRAS, 336, 753

[31] Srianand R., Shankaranarayanan S., 1999, ApJ, 518, 672

[32] Turnshek D.A., 1988, in STScI Symposium Series 2, QSO Absorption lines: Probing the Universe, ed. J.C. Blades, D. Turnshek, & C. Norman (Cambridge:Cambridge Univ. Press)

[33] Verner D.A., Barthel P.D., Tytler D., 1994, A&AS, 108, 287

[34] Vignali C. et al., 1999, ApJ, 516, 582

[35] Vignali C. et al., 2001, AJ, 122, 2143

[36] Vignali C. et al., 2003, AJ, 125, 418

[37] Weymann R.J., Morris S.L., Foltz C.B., Hewett P.C., 1991, ApJ, 373, 23

Chapter 7

Concluding remarks

In this thesis we have used absorption lines to study environments of the two *almost* exclusive classes of AGN i.e. radio loud AGN and broad absorption line quasar. We have made observations with the Arecibo telescope and GMRT at radio wavelengths, VLT at optical and also used archival data of HST, FUSE and IUE at ultraviolet. This last Chapter gives an overview of the main results obtained in the thesis and recent developments in the field related to issues raised in section 1.2.

- ***New 21-cm absorption detections from our surveys***

  - *21-cm absorption associated with J1124+1919 (3C 258)*
    We detected 21-cm absorption associated with the CSS galaxy 3C 258 ($z_{\rm em}$=0.165), whose HST image shows an odd-shaped galaxy with an arc-like structure of high-surface brightness, and a larger, fainter tail extending to the northeast. The HI absorption spectrum is complex, fitted with seven Gaussian components, possibly due to interaction of the compact radio source with the ISM of the host galaxy. The FWHM of line is at the narrow end when compared to values of 21-cm associated with other CSS sources. The individual Gaussian components are narrow, with FWHM lying between $\sim$4 and 12 km s^{-1}, implying $T_s \lesssim 400-2000$ K.
  - *21-cm absorption associated with the core of J2245+3941 (3C 452)*
    3C 452 is a high excitation narrow-line FR II radio galaxy exhibiting a symmetric triple morphology. 21-cm absorption profile detected towards the core is resolved into three components with deepest and narrowest of these being consistent with

the velocity corresponding to [O III] emission lines. The neutral hydrogen column density of the gas is estimated to be N(HI)=$6.39\times10^{20}(T_s/100)(f_c/1.0)^{-1}$ cm^{-2}. If the 21-cm absorber is also responsible for the nuclear absorption seen at x-ray wavelengths, then for a spin temperature of ∼8000 K, the absorber occults only ∼10 per cent of the radio core. This would also be consistent with the nuclear extinction seen at infrared wavelengths.

- ***21-cm absorption detection rate and its dependence on radio source properties and redshift***

  21-cm absorption surveys in the recent past have concentrated on the samples of compact radio sources (see e.g. Vermeulen et al. 2003; Philström et al. 2003) with larger sources getting hardly any attention. Vermeulen et al. and Pihlström et al. detected HI absorption associated with 33% of the compact (mostly CSS and GPS) radio sources, with HI being anti-correlated with source size. In **Chapters 2 and 5**, we have presented the results of our 21-cm absorption survey that included both compact radio sources and cores of large radio galaxies; 37 sources in total. These results include 2 new 21-cm absorption detections, higher spectral resolution and signal-to-noise spectra for 5 radio sources, HI emission from one and 21-cm absorption upper limits for the remaining 29 sources. These observations in conjunction with the results available in literature have allowed us to investigate the properties of 21-cm absorption in compact as well as classical large radio sources at similar scales. The resultant sample has 75 compact radio sources with HI detection rate being highest (45%) for the most compact GPS sources. The anti-correlation between the HI column density and source size for GPS and CSS sources, first noted by Pihlström et al. (2003), is confirmed by this enlarged sample. This anticorrelation is also consistent with the optical spectroscopic observations of van Ojik et al. (1997), who interpreted deep troughs in the Lyα emission profiles of 18 high-redshift ($z > 2$) radio galaxies (HZRGs) to be absorption due to HI with column densities in the range $10^{18}-10^{19.5}$ cm^{-2}. Interestingly, 9 out of the 10 HZRGs with sizes <50 kpc have associated HI absorption compared with 2 of the 8 larger (>50 kpc) ones. We didn't find any significant correlation between the 21-cm absorption and redshift, and radio source luminosity (sample extends upto $z \sim 1$ and is spread over 4 orders of magnitude in luminosity).

  CSS and GPS sources are believed to be younger counterparts of classical large radio sources. In **Chapter 5**, we have investigated whether the properties of circumnuclear

gas evolves as the radio source grows from CSS and GPS scales to the large radio sources. For this purpose we have used results from our GMRT survey of 21-cm absorption towards the cores of 10 radio galaxies and those available in the literature. The final sample consists of 44 large FR I and FR II radio galaxies. It is interesting to note that for FR I sources 21-cm absorption is detected towards 7 out of 25 (∼25%) objects whereas 7 out of 19 (∼35%) FR II exhibit 21-cm absorption. Although affected by small number statistics these detection rates compare very well with the detection rate (∼35%) towards the compact radio sources. To first order for FR II radio sources this means that their galactic environments are similar for compact (i.e. young) and large (i.e. evolved) radio sources. Detection rates for large radio galaxies, for both FR I and FR II, could very well be higher than the current estimate as several upper limits are not *deep enough* (see Fig. 5.12). Quite significant (∼25%) and statistically comparable 21-cm absorption detection rate for FR I radio galaxies is particularly interesting as they are believed to have much smaller amounts of obscuring material in terms of *thin* circumnuclear disks (see e.g. Morganti et al. 2001; van Langevelde et al. 2000; Taylor et al. 1999). The absence of optically thick obscuring material has also been confirmed by HST observations of a sample of 33 FR I radio galaxies (Chiaberge et al. 1999).

- ***Distribution of neutral hydrogen in radio loud AGN and consistency with the expectations of unification schemes***

  Determining the distribution of different components (ionised, neutral and molecular) of circumnuclear gas in radio loud AGN is important for studying the anisotropy in radiation field and thereby testing the unified scheme. In **Chapter 4**, we have examined the dependence of HI column density on the degree of core prominence, which is being used as a statistical measure of the orientation of the source axis to the line of sight (Orr & Browne 1982; Kapahi & Saikia 1982), for a sample of 32 CSS and GPS sources. In our sample, 15 out of 23 galaxies exhibit 21-cm absorption as against 1 out of 9 quasars, which is broadly consistent with the unification scheme. Also there is a tendency for the detection rate as well as column density for galaxies to increase with core prominence, a statistical indicator of the orientation of the jet axis to the line of sight. This can be understood in a scenario where radio sources are larger than the scale of the circumnuclear HI disc so that the lines of sight to the lobes at very large inclinations do not intersect the disc. The sources in our sample also exhibit the known anticorrelation between HI column density and source size. This suggests that

small linear size, along with intermediate values of core prominence, is a good recipe for detecting 21-cm absorption in CSS and GPS objects. Very Long Baseline Interferometry (VLBI)-scale spectroscopic observations towards several sources such as the CSS object J0119+3210 (4C+31.04) and the cores of larger sources such as the well known Fanaroff-Riley class II (FR II) source Cyg A and the FRI objects NGC 4261 and Hydra A show evidence of absorption arising from a circumnuclear disk-like structure (Conway & Blanco 1995; Conway 1999; van Langevelde et al. 2000). In case of classical large FR II radio galaxies, statistical evidence of the presence of circumnuclear disk comes from the that fact 21-cm absorption is not detected towards any of the broad-line radio galaxies (BLRGs) which are supposed to have jet-axis aligned closer to the line-of-sight than compared to narrow-line radio galaxies (cf. **Chapter 5**).

As noted above, the case of large FR I radio galaxies is particularly curious. HST imaging and X-ray observations both have suggested the presence of unobscured cores in as many as ∼85% of the sources (Chiaberge et al. 1999; Trussoni et al. 1999, 2003). It has been postulated that FR I sources have relatively *thin* circumnuclear disks as compared to FR II class. Detection in about ∼25% is therefore surprising especially when most of the upper limits on 21-cm optical depth are not very deep (see Fig. 5.12). Clearly this issue needs to be investigated with deeper 21-cm observations of a large sample of FR I sources.

Obviously, deeper 21-cm searches with VLBI-class resolution of much larger samples of CSS, GPS and cores of large radio sources will help in determining accurate optical depths and also constraining the location of absorbing gas. In **Chapters 2 and 5**, we have discussed in detail the caveats that limit the interpretation of 21-cm absorption measurements in relation to radio source properties and redshift. For large radio sources the data is presently limited by sensitivity and sample size while for the compact radio sources where the large number of measurements are available the samples are heterogeneous. Samples of CSS and GPS chosen for 21-cm absorption searches span large range in radio source luminosity and redshift. Studies with large, homogeneous samples are needed to effectively examine the dependence of 21-cm absorption properties on radio source properties and test the evolutionary models.

- ***Role of jet-cloud interaction in determining the kinematics and physical conditions of absorbing gas***

  In addition to the circumnuclear disk, absorption could also occur in neutral clouds that are part of the gas that has been accelerated by interaction with the radio jet.

Imprints of this interaction are to be found in kinematical and physical conditions of the gas and structural properties of radio source. Compact radio sources, which are supposed to evolve by boring through the host galaxy ISM, have been found to be more asymmetric in terms of structural, brightness and polarization symmetry parameters (Saikia et al. 1995, 2001; Saikia & Gupta 2003). Signatures of interaction with jet in CSS sources have been detected in broad and complex emission-line profiles and their alignment with radio structure. Gelderman & Whittle (1994) found that properties of [O III] λ5007 for a sample of CSS sources suggested that kinematics of emission line were driven by the radio source. Radio-optical alignment, i.e. similar extent and alignment for the radio source and emission-line gas, has been detected for larger as well as compact radio sources (Chambers et al. 1987; McCarthy et al. 1987; de Vries et al. 1999; Axon et al. 2000; O'Dea et al. 2002). More recently Labiano et al. (2005) using HST long-slit spectroscopy of the emission-line nebulae in the CSS sources 3C 67, 3C 277.1 and 3C 303.1 have shown that emission-line ratios are consistent with a mix of shock excitation and photoionization in the extended gas. In addition, they found line ratios indicative of lower ionization gas to be associated with higher gas velocities.

In this thesis we have explored the theme of jet-cloud interaction by looking for its imprints in the kinematics and physical conditions of the absorbing gas. In **Chapter 2** we showed that distribution of the velocity shifts of the principal (strongest) 21-cm absorption component associated with CSS and GPS sources tends to be blue-shifted. We note that skewness of the distribution comes largely from the principal components detected towards most compact i.e. GPS sources. The higher incidence of blue-shifted features suggests that some of the absorption could be due to gas clouds accelerated by the radio jets. Evidence for jet-cloud interaction has been further reinforced by discovery of gas outflows as fast and broad as $\sim$1000 km s^{-1} in a number of radio sources in neutral as well as ionised gas (Morganti, Tadhunter & Oosterloo 2005). In **Chapter 3**, we have investigated physical conditions in the outflowing material detected in absorption in the CSS quasar 3C 48. 3C 48 has a highly complex and distorted radio structure, speculated to be due to disruption of jet by interaction with a cloud. Outflowing material detected by us in the HST, FUSE and IUE spectra exhibits absorption lines over large range of ionisation states. We explore the physical conditions in the absorbing material using photoionization simulation code CLOUDY. Considering the similarity with kinematics of the emission-

line gas and physical situation in 3C 48 we show that outflowing material detected in absorption may have also interacted with radio jet.

As noted above whether it be structural, brightness and polarization asymmetry or kinematical and ionisation properties of gas seen in emission and absorption, evidences from all the quarters underlines the strong interaction of compact radio source with its environment. This is to be contrasted with the scenario of classical large FR I and FR II radio galaxies presented in **Chapter 5**. Majority of 21-cm absorption lines in the sample of large radio galaxies are either redshifted or consistent with the systemic velocity. This further accentuates the role played by jet-cloud interaction in accelerating the gas clouds in the case of compact radio sources.

- ***OH upper limits and their implications***

  In **Chapter 2** along with the results of 21-cm absorption search I presented the upper limits on OH column densities for 9 sources. These sources, observed at Arecibo telescope, were simultaneously searched for HI and OH. Molecular absorption searches towards AGN have had very little success so far with only a few systems detected till now (see also Darling & Giovanelli 2002; Kanekar & Chengalur 2002). Although circumnuclear gas around AGN is expected to have molecular component as well (Maloney et al. 1994), these non-detections suggest that either molecules have been destroyed or the OH and CO transitions used so far to search for molecules have been radiatively suppressed (Black 1998).

- ***X-ray quietness of BAL QSOs***

  Broad absorption line quasars have been known to be systematically X-ray quiet as compared to non-BAL QSOs (Korista et al. 1993; Green et al. 2001). It is almost likely that this X-ray weakness is intrinsic although existing models of BAL systems largely assume standard QSO spectrum. In **Chapter 6** I have presented detailed analysis of two well detached BAL outflow components that are seen in the spectrum of $z_{\rm em}\simeq$4.92 QSO SDSS J160501.21-011220.0. We find that observed column densities of N V , Si IV and C IV in the $z_{\rm abs}$= 4.855 component require that nitrogen is underabundant by more than a factor of 3 compared to silicon if the gas is photoionized by a typical QSO spectrum. We show that if the composition of BAL is like that of the emission line regions then the observed column densities can be reproduced if the absorbing cloud sees an ionizing spectrum similar to what we observe from this QSO i.e. a spectrum strongly attenuated in the X-rays.

Bibliography

[1] Axon D.J., Capetti A., Fanti R., Morganti R., Robinson A., Spencer R., 2000, AJ, 120, 2284

[2] Black J.H., 1998, The Molecular Astrophysics of Stars and Galaxies, edited by Thomas W. Hartquist and David A. Williams. Clarendon Press, Oxford, 469

[3] Chambers K.C., Miley G.K., van Breugel W., 1987, Nature, 329, 604

[4] Chiaberge M., Capetti A., Celotti A., 1999, A&A, 349, 77

[5] Conway J.E., Blanco P.R., 1995, ApJ, 449, L131

[6] Conway J.E., 1999, NewAR, 43, 509

[7] Darling J., Giovanelli R., 2002, AJ, 124, 100

[8] de Vries W.H., O'Dea C.P., Baum S.A., Barthel P.D., 1999, ApJ, 526, 27

[9] Gelderman R., Whittle M., 1994, ApJS, 91, 491

[10] Green P.J., Aldcroft T.L., Mathur S., Wilkes B.J., Elvis M., 2001, ApJ, 558, 109

[11] Kanekar N., Chengalur J.N., 2002, A&A, 381, L73

[12] Kapahi V.K., Saikia D.J., 1982, JApA, 3, 465

[13] Korista K. et al., 1993, ApJ, 413, 445

[14] Labiano A. et al., 2005, A&A, 436, 493

[15] Maloney P.R., Begelman M.C., Rees M.J., 1994, ApJ, 432, 606i

[16] McCarthy P.J., van Breugel W., Spinrad H., Djorgovski S., 1987, ApJ, 321, L29

[17] Morganti R., Oosterloo T.A., Tadhunter C.N., van Moorsel G., Killeen N., Wills K.A., 2001, MNRAS, 323, 331

[18] Morganti R., Tadhunter C.N., Oosterloo T.A., 2005, A&A, 444, L9

[19] O'Dea C.P. et al., 2002, AJ, 123, 2333

[20] Orr M.J.L., Browne I.W.A., 1982, MNRAS, 200, 1067

[21] Pihlström Y.M., Conway J.E., Vermeulen R.C., 2003, A&A, 404, 871

[22] Saikia D.J., Jeyakumar S., Wiita P.J., Sanghera H.S., Spencer R.E., 1995, MNRAS, 276, 1215

[23] Saikia D.J., Jeyakumar S., Salter C.J., Thomasson P., Spencer R.E., Mantovani F., 2001, MNRAS, 321, 37

[24] Saikia D.J., Gupta N., 2003, A&A, 405, 499

[25] Taylor G.B., O'Dea C.P., Peck A.B., Koekemoer A.M., 1999, ApJ, 512, L27

[26] Trussoni E., Vagnetti F., Massaglia S., Feretti L., Parma P., Morganti R., Fanti R., Padovani P., 1999, A&A, 348, 437

[27] Trussoni E., Capetti A., Celotti A., Chiaberge M., Feretti L., 2003A&A, 403, 889

[28] van Langevelde H.J., Pihlström Y.M., Conway J.E., Jaffe W., Schilizzi R.T., 2000, A&A, 354, 45

[29] van Ojik R., Röttgering H.J.A., Miley G.K., Hunstead R.W., 1997, A&A, 317, 358

[30] Vermeulen R.C. et al., 2003, A&A, 404, 861